Sensitivity of the ANTARES neutrino telescope to Gamma-Ray Bursts

Den Naturwissenschaftlichen Fakultäten

der Friedrich-Alexander-Universität Erlangen-Nürnberg

zur

Erlangung des Doktorgrades

vorgelegt von

Melitta Naumann-Godó
aus Arad

Als Dissertation genehmigt von den Naturwissenschaftlichen Fakultäten der Universität Erlangen-Nürnberg

Tag der mündlichen Prüfung:	26.02.2007
Vorsitzender der Prüfungskommission:	Prof. Dr. E. Bänsch
Erstberichterstatter:	Prof. Dr. G. Anton
Zweitberichterstatter:	Prof. Dr. G. van der Steenhoven

To my physics teacher Erich Kreißl,
for his encouragement

Abstract

The ANTARES neutrino telescope is currently being installed in the Mediterranean Sea with the principal objective of searching for galactic and extragalactic sources of high-energy cosmic neutrinos and neutrinos from dark matter annihilation.

This thesis is dedicated to the detection of neutrinos from gamma-ray bursts (GRBs) with the ANTARES detector. The "hindsight method" is presented as an off-line method for the identification of GRB-neutrinos, which can be applied a posteriori as it uses GRB coordinates recorded beforehand by gamma-ray satellites in orbit, together with ANTARES event data previously collected in normal sampling mode, thus complementing the existing alert-based method.

To predict its sensitivity, the neutrino flux from individual gamma-ray bursts which have been observed with the BATSE detector is estimated. The neutrino emission is calculated in two ways within the framework of the GRB fireball model with internal shock waves: the first model assumes that 10% of the γ-luminosity is emitted in the form of neutrinos, while the second model is more elaborate in the sense that it directly normalises the individual neutrino flux to the measured luminosity of the GRB in question. By summarising the individual neutrino spectra, the average GRB-neutrino flux is calculated for different types of GRBs (long bursts, short bursts and X-ray flashes).

For the calculation of the expected rate of GRB-neutrinos in ANTARES the key parameters of the telescope such as effective area and angular resolution are determined from the modified muon reconstruction algorithm. Given the unexpectedly high rate of optical noise in the deep sea at the ANTARES site, probably due to the increase in bioluminescent activity since the first site evaluation measurements, this thesis has also been devoted to the development of a reconstruction algorithm which is robust with respect to high-level and varying background noise and retains most of the efficiency familiar from low noise levels, while at the same time maintaining the purity of the reconstructed events.

Background studies taking into account both atmospheric neutrinos and muons alike suggest that one neutrino detected in coincidence with the time and angular window of a recorded GRB during an observation period of approximately 5 years would already be significant to a level of 3σ. This measurement of a single GRB-neutrino would already constitute a benchmark observation, since it would confirm the acceleration of hadrons to at least the measured energy and thereby provide a clue to the origin of high-energy cosmic rays. In the regrettable case of the absence of a GRB-neutrino signal a 5-year limit could be derived corresponding to

$$E^2\Phi_{90\%} = 3.8 \cdot 10^{-9} \quad \text{GeV cm}^{-2}\ \text{s}^{-1}\ \text{sr}^{-1}$$

if a flux corresponding to the second GRB flux model is expected.

Contents

Introduction

Le seul véritable voyage n'est pas d'aller vers d'autres paysages, mais d'avoir d'autres yeux.
The real voyage of discovery consists not in seeking new landscapes, but in having new eyes.
Marcel Proust, French novelist (1871 - 1922)

Historically, the field of astronomy is based on optical observations starting with the naked eye and advancing towards more sophisticated instruments to boost resolution. As detector techniques improved, the frontiers of astronomy were extended further at both ends of the photon spectrum with radio astronomy and gamma-ray astronomy already matured.

At the high-energy end of the spectrum, photon astronomy has made considerable progress thanks to the successes of the Compton Gamma-Ray Observatory and the imaging air Cherenkov telescopes. However, an intrinsic limit is set on further exploration by the attenuation of gamma-rays from distant sources due to pair production in interactions with the photons of the cosmic microwave background (CMB) radiation:

$$\gamma + \gamma_{2.7K} \rightarrow e^+ + e^-.$$

As the Universe is not transparent to photons of TeV energy and above, new astronomical messengers such as neutrinos, very high-energy cosmic rays (at EeV[1] energies) and gravitational waves rise into the exploratory focus and are becoming increasingly important for probing the high-energy sky to its outer edge.

At EeV energies, proton astronomy is also conceivable, at least in terms of pointing accuracy, since at such high energies the ambient magnetic field no longer diverts the direction of charged particles. However, the Universe is also opaque to the highest-energy cosmic rays, since they likewise interact with the CMB, predominantly by photoproduction via the Δ resonance:

$$p + \gamma_{2.7K} \rightarrow \Delta^+ \rightarrow \pi + N.$$

[1] 1 EeV = 1 Exa eV = 10^{18} eV = 0.16 J

This so-called GZK-cutoff[2] [1],[2] establishes an upper limit to the range of high-energy nuclei. For instance, the absorption length of a 50 EeV proton is 10 Mpc (see Fig. 0.1).

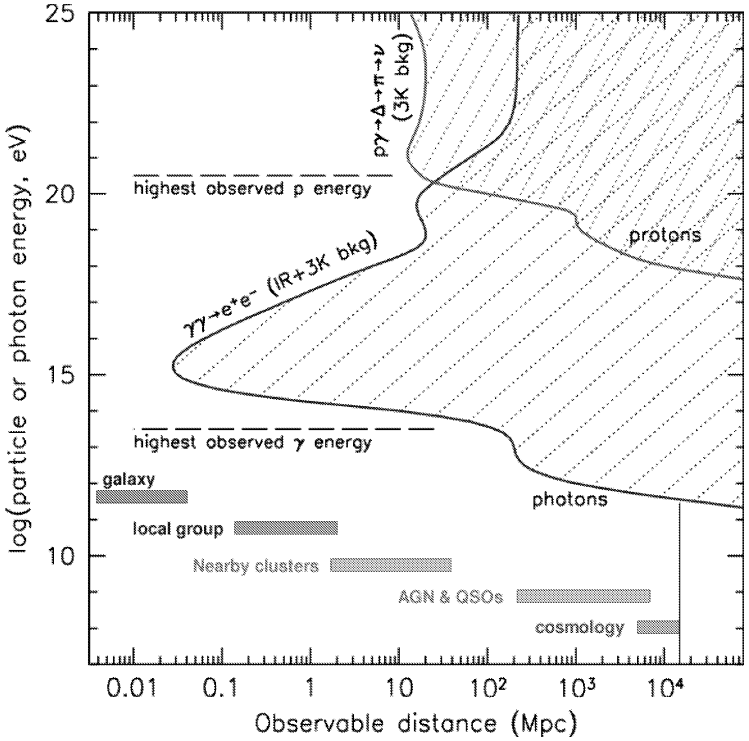

Figure 0.1: *Absorption length in Megaparsec as a function of photon/proton energy.[3]*

Thus, despite considerable instrumental challenges due to the extremely low cross-section of neutrino interactions and the modest angular resolution compared to conventional astronomical instruments, neutrino astronomy is a promising complementary field of astrophysics, especially at high energies. Both cross-section and angular resolution increase with energy, and large natural resources of ice and water can be instrumented and thus exploited as target material. Moreover, the low cross-section of neutrinos enables them to escape from very dense regions (e.g. the centre of galaxies or collapsing stars), which are otherwise opaque to photons, and reach us without being hindered by clouds and other material on the way.

Therefore, neutrino astronomy can address a number of fundamental questions concerning the origin of cosmic rays and the physics behind the most luminous and violent phenomena in the Universe such as gamma-ray bursts and active

[2]first predicted by Greisen, Zatsepin and Kuzmin

galactic nuclei. The discovery potential of neutrino astronomy could also be extended to include dark matter which is likely to annihilate itself in gravitational centres (such as the galactic centre or the Sun), producing among other things neutrinos, which are perhaps the only particles capable of escaping from these dense regions.

Regions from which both neutrinos and photons can also be observed are of great interest because combined observations can provide a lot of information about the internal mechanisms of these energetic objects and maybe help identify the acceleration mechanisms behind the highest-energy cosmic rays.

1 Neutrinos in astrophysics and cosmology

The observation of cosmic rays (CR) ranging over more than 10 orders of magnitude in energy can be viewed in connection with neutrino production on various energy scales and by different mechanisms. Neutrinos are known to emerge from the interaction of cosmic rays with different background media – in analogy to conventional beam dumps – which they encounter during their propagation, such as the terrestrial atmosphere, intragalactic gas and cosmic microwave background radiation.

In addition to these guaranteed neutrino fluxes, there are a number of candidate neutrino sources based on the assumption that the astrophysical sources responsible for the acceleration of cosmic rays due to the gravitational energy release in very luminous objects will also produce neutrinos as a by-product of their cooling. This direct connection between neutrinos and cosmic rays could be proved by the observation of neutrinos from sources known to emit high-energy non-thermal gamma-rays, such as gamma-ray bursts, active galactic nuclei, supernova remnants, x-ray binaries etc. Such an observation would constitute a smoking-gun evidence of the origin of the hadronic component of cosmic rays.

1.1 Neutrino background emission from known sources

Atmospheric neutrinos

Neutrinos are produced in abundance when cosmic rays penetrate the atmosphere. For the high-energy cosmic rays, the atmosphere represents an absorber with exponentially increasing density. As a result, the interaction of cosmic rays with air can be described phenomenologically as a showering process yielding a cascade of secondary particles, which in turn decay or continue to interact. Neutrinos arise from the decay of pions, kaons and other hadrons as well as from the

decay of muons. They provide a significant background for neutrino telescopes, which needs to be discriminated so that extraterrestrial sources can be detected.

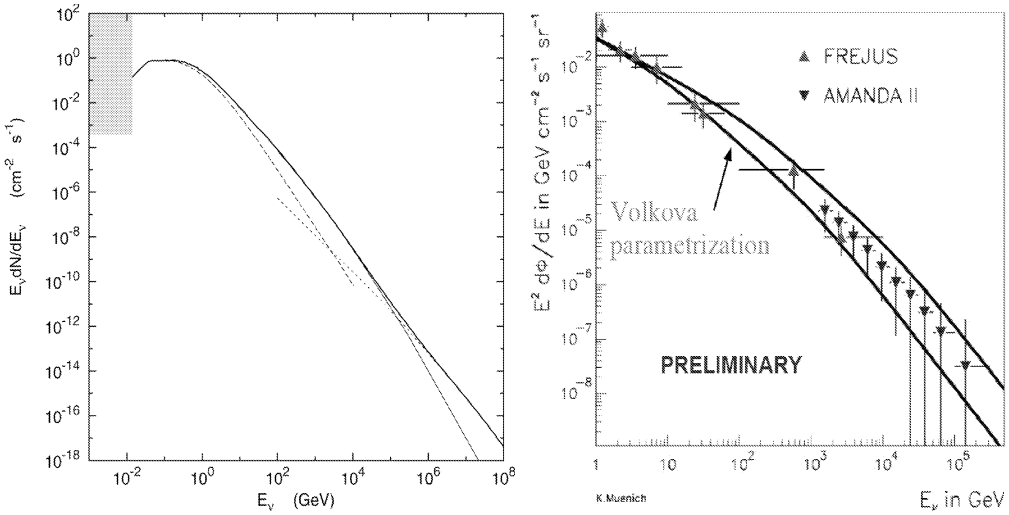

Figure 1.1: *Left: Composition of the atmospheric neutrino spectrum from [4]: vertical flux of $\nu_\mu + \bar{\nu}_\mu$ (heavy solid line); $\nu_e + \bar{\nu}_e$ (dashed line); prompt neutrino (dotted line); $\nu_\mu + \bar{\nu}_\mu$ from pion and kaons (thin solid line at high energies). The shaded region is dominated by solar neutrinos. Right: Measured atmospheric neutrino flux by Amanda and Frejus [5]. The black lines indicate the theoretical values for the horizontal (upper) and vertical (lower) direction respectively.*

The main components of the high-energy atmospheric neutrino flux are presented in Figure 1.1. At low energies, the flux is dominated by conventional atmospheric neutrinos, which arise from the decay of charged pions and kaons. At energies below several GeV, the muons have not yet been attenuated relativistically and hence decay, producing ν_e and ν_μ with a ratio of $1:2$ in accordance with the initial pion distribution. However, as Super-Kamiokande has demonstrated, when the atmospheric neutrinos are used as a test beam, neutrino oscillation effects have to be taken into consideration. With ν_μ oscillating almost exclusively into ν_τ, the neutrino flavour composition changes from initially $1:2:0$ to $1:1:1$ at energies close to 1 GeV. Well above this energy level, oscillation effects can be safely ignored in the treatment of atmospheric neutrinos.

Above a few hundred GeV, the pion flux is larger than the kaon flux but, since the pions are more likely to interact before decaying, the total neutrino flux is dominated by the kaon contribution.

At high energies above 1 TeV, kaons also start to become significantly attenuated before decaying, thus lending importance to the prompt component. In this

energy region neutrinos are produced predominantly by the decay of short-lived charmed mesons such as $D^{\pm}$, D^0, D_s and Λ_c. The calculation of the prompt neutrino flux requires taking into account next to leading order processes in the charm production cross-section, which heavily depend on the behaviour of the parton distribution functions at small x, below the lowest values ($x \approx 10^{-5}$) probed in collider experiments. Hence, estimating the prompt neutrino flux involves systematic uncertainties due to the need for extrapolating the parton distribution functions over several orders of magnitude. Therefore, measuring the atmospheric neutrino flux at energies in the PeV region will have an important impact on parton distribution functions.

Moreover, the prompt atmospheric neutrino flux also depends considerably on the assumed chemical composition of the cosmic rays. For the same spectrum, a heavier composition of cosmic rays would result in a lower CR-nucleon flux, thus leading to lower neutrino fluxes. While the detailed composition of cosmic rays below the knee[1] has been well measured in air shower experiments, at higher energies a rigidity-dependent model has to be assumed, which again introduces theoretical uncertainties.

The differential atmospheric neutrino flux can be parametrised with the use of a broken power law to account for the above-mentioned components of the flux. In addition, the angular variation of the neutrino flux, called the secant theta effect, is also taken into consideration in the analytic approximation. The conventional atmospheric neutrino flux component arising from pion and muon decay peaks at the horizon due to the comparatively longer flight-time in thinner layers of the atmosphere, thus increasing the decay probability. In contrast, the prompt atmospheric neutrinos – as their name indicates – are produced instantly and hence distributed isotropically, following the spectrum of the primary cosmic rays.

The differential spectra of atmospheric muon neutrinos ($\nu_\mu + \bar{\nu}_\mu$) at sea level are analytically approximated by [6] as a function of the zenith angle θ and the neutrino energy E in units of (GeV m^2 s sr)$^{-1}$:

$$\Phi_{\nu_\mu}(E,\theta) \simeq \begin{cases} 285 \left(\frac{E}{GeV}\right)^{-2.69} \left(\frac{1}{1+\frac{6E}{E_\pi(\theta)}} + \frac{0.213}{1+\frac{1.44E}{E_{K^\pm}(\theta)}}\right), & 10^2\ GeV < E < 5.4 \cdot 10^5\ GeV \\ 4800 \left(\frac{E}{GeV}\right)^{-4.04} (E_\pi(\theta) + 0.89 E_{K^\pm}(\theta)), & E > 5.4 \cdot 10^5\ GeV \end{cases} \tag{1.1}$$

The corresponding electron neutrino ($\nu_e + \bar{\nu}_e$) spectra from muon and kaon decay can be parametrised by

[1] The transition region in the cosmic ray spectrum around 4 PeV where the spectral index steepens from 2.7 to 3.0 is called the "knee".

$$\Phi_{\nu_e}(E,\theta) \simeq \begin{cases} 24\left(\frac{E}{GeV}\right)^{-2.69}\left(\frac{0.05}{1+\frac{1.5E}{E_{K^\pm}(\theta)}}+\frac{0.185}{1+\frac{1.5E}{E_{K_2^0}(\theta)}}+\frac{11.4E^{\zeta(\theta)}}{1+\frac{1.21E}{E_\pi(\theta)}}\right), & 10^2 < E < 3.7\cdot 10^5\ GeV \\ 71\left(\frac{E}{GeV}\right)^{-4.045}(E_{K^\pm}(\theta)+3.7E_{K_2^0}(\theta)), & E > 3.7\cdot 10^5\ GeV \end{cases} \tag{1.2}$$

The values for $E_\pi(\theta)$, $E_{K^\pm}(\theta)$, $E_{K_2^0}(\theta)$, and $\zeta(\theta)$ are extracted from tables given in [6]. The accuracy of these formulae is about 5% in shape, but the absolute flux is uncertain to about 20%. It is also evident that electron neutrinos are suppressed by nearly two orders of magnitude in comparison to muon neutrinos because, at the high energies involved, all the decay channels which would produce ν_e via muon decay contribute only to a small extent since the lifetime of the muons is relativistically prolonged, allowing them to reach sea level before decaying.

Galactic neutrinos

Cosmic rays also propagate through the interstellar medium of our galaxy, thereby producing secondary particles such as neutrinos in hadronic interactions similar to those reactions giving rise to the terrestrial atmospheric neutrino flux. Unlike Earth's atmosphere, the interstellar medium has a much lower density of about 1 particle per cm^3 which leads to far greater interaction lengths as compared to the decay lengths of the secondary particles. Therefore, in contrast to the atmospheric scenario, mesons and muons are more likely to decay on the way rather than to interact.

As a result, the flux of galactic neutrinos can exceed the flux of atmospheric neutrinos at very high energies, at which the latter is typically suppressed by the energy loss of mesons in high-energy collisions. However, at the low energy end of the spectrum the atmospheric neutrino flux clearly dominates the galactic flux due to the increased rate of reaction by the cosmic rays with the dense atmosphere.

On the assumption that the cosmic ray flux on Earth is uniformly and isotropically distributed throughout the galaxy, the neutrino flux from the galactic disk has been calculated on the basis of density, with the interstellar medium in a column length of 1 kpc and a density of 1 nucleon/cm^3 [7]. The resulting fluxes for muon and electron neutrinos are shown in Figure 1.2 multiplied by E^3.

Extragalactic (cosmogenic) neutrinos

Very high-energy cosmic rays propagating in the extragalactic medium interact with the cosmic microwave background and infra-red (IR), optical (Opt), and

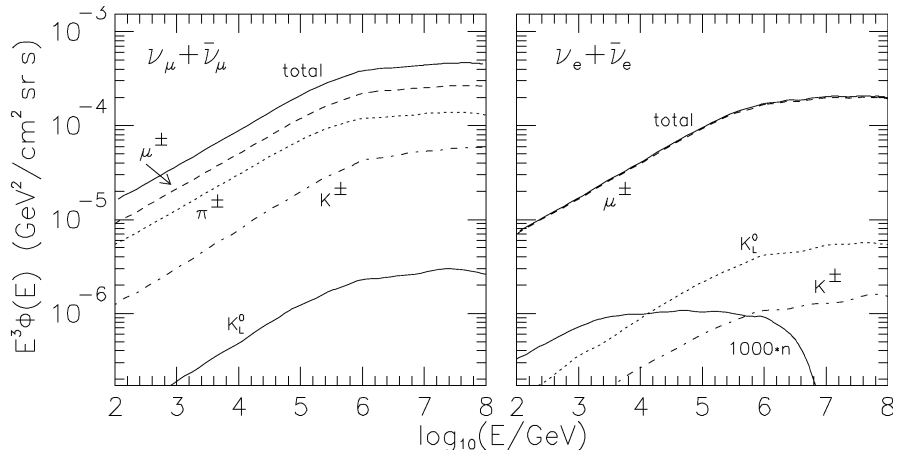

Figure 1.2: *Total galactic flux of muon and electron neutrinos and the contributions from the decay of the indicated particles. [7]*

ultra-violet (UV) background photons. These interactions produce features in the ultra-high-energy cosmic ray spectrum such as the GZK-cutoff (see introduction) and their decay products generate the cosmogenic neutrino flux, also referred to as GZK neutrinos.

The total cosmogenic flux was calculated by [8] and is displayed in Figure 1.3. Three distinct peaks appear in the total cosmogenic neutrino flux. In the TeV energy region the flux is generated purely by neutron decay, which gives rise to electron neutrinos only. At higher energies, in the PeV region, the contribution due to hadronic interaction with UV/Opt/IR photons dominates, while at the highest energies prior to the GZK-cutoff the neutrinos are produced via interaction of protons and nuclei with the CMB radiation. In these models, pions are generated via photoproduction and neutrinos emerge from the decay of π^+.

However, despite comprehensive knowledge of the particle physics behind the GZK-cutoff, the phenomenon itself has not been conclusively measured. It is still unclear whether the cosmic ray spectra are truncated above 10^{20} eV, mainly due to lack of data, which is understandable at the extremely low fluxes involved.

1.2 Candidate cosmic neutrino sources

In contrast to the guaranteed neutrino emission from processes involving cosmic rays hitting ambient matter or radiation, there are also astrophysical objects which might qualify as neutrino sources if the predicted hadronic interaction processes applied to them.

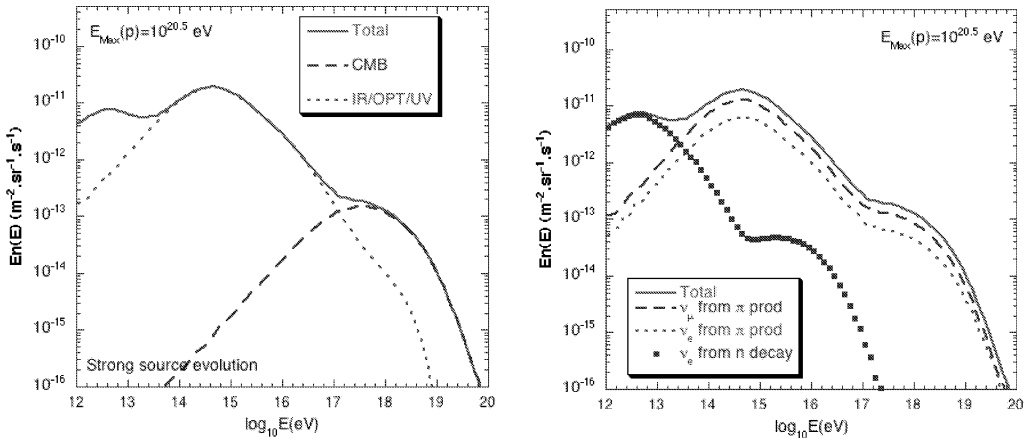

Figure 1.3: *Total cosmogenic neutrino flux from pure proton sources assuming strong source evolution. Left: The contribution from different backgrounds. Right: The contribution of different neutrino flavours (without oscillations). [8]*

The generic models of astrophysical neutrino production are based on the assumption of a highly relativistic hadronic beam hitting a target, which results in pion production and subsequent decay. From the observation of ultra-high-energy cosmic rays it is evident that particle acceleration exceeding EeV-energies is possible. Furthermore, shock acceleration of particles is known to occur in solar flares, for instance, so it is likely that charged particles undergo diffusive shock acceleration, also termed Fermi acceleration, on a much larger scale in the following objects:

- **Gamma-Ray Bursts (GRBs)**
  Gamma-ray bursts are sudden and extremely intense flashes of gamma-rays which, for a few seconds, outshine the entire gamma-ray sky. Their copious energy release amounts to $10^{51} - 10^{54}$ erg/s, which makes them, for a brief period of time, the most luminous objects known in the Universe[2]. Observations of an afterglow shifting slowly from x-ray to optical and eventually radio emission are the key factor in measuring the redshift distances and thereby identifying the host galaxies.

  This has confirmed the earlier assumption drawn from the isotropic distribution of GRBs that they are indeed located at cosmological distances. Hitherto, the highest measured redshift has been $z = 6.3$ for GRB 050904 [9], with a clear signature of a Gunn-Petersen trough [10] in the spectrum, otherwise detected only in high-z quasars. Since this feature is produced

[2] 1 erg $= 10^{-7}$ J $= 625$ TeV

by absorption through neutral hydrogen gas in the intergalactic medium, it provides evidence of the early Universe before reionisation.

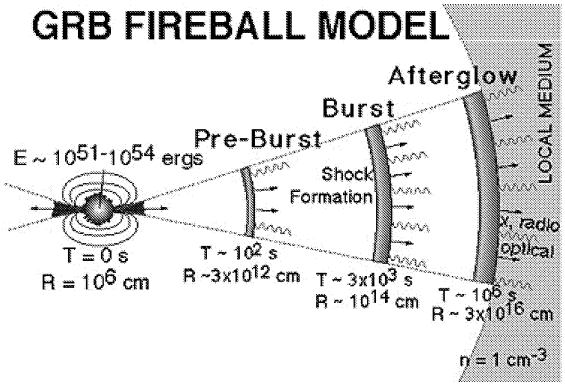

Figure 1.4: *Schematic view of a gamma-ray burst [11].*

The non-thermal gamma spectra suggest that GRBs are produced by the dissipation of the kinetic energy of a relativistically expanding wind, called a fireball, whose primal origin is still unclear. Regardless of what was the progenitor, the fireball shock model [12] (see also Chapter 5.1) provides a good explanation for the observed spectra and the small timescales. It is based on the fact that shock waves inevitably occur in an outflow as soon as the fireball becomes transparent and hence particles accelerate at these shock fronts. When the forward shock impinges on the external medium it decelerates and gives rise to the afterglow radiation (see Figure 1.4). At the same time a reverse shock moving back into the ejecta is also thought to accelerate particles.

It is assumed that the observed non-thermal gamma spectra are the result of such shock-accelerated electrons or positrons, which lose their energy by synchrotron radiation. If this model is accepted as valid, protons are also accelerated in the same shock waves, reaching energies of up to 10^{20} eV. Interaction with the fireball photons leads to the production of pions, which in turn decay into muons and neutrinos. It is estimated that 10% of the gamma luminosity is emitted in the form of neutrinos [13].

- **Active Galactic Nuclei (AGNs)**
  Active galactic nuclei are powered by the gravitational energy release associated with the accretion of interstellar gas onto a supermassive black hole of about 10^8 solar masses in the centre of a galaxy. Observations [15] indicate that the outermost regions of the accretion disc (at one parsec from the central object) probably rotate with Keplerian velocity, which is referred to as "standard disc". This standard disc is assumed to emit continuum ra-

diation peaking in the visible but extending into X-ray and gamma ranges due to a relativistic jet of particles, and also into the far-infrared range due to the presence of dust surrounding the central region. Superimposed onto this wide continuum emission, AGN spectra also display broad emission lines emitted by ionised gas. The spectral lines show a Doppler broadening, which increases the closer they are to the centre due to the higher Keplerian velocities.

The whole family of AGNs may be unified by using one model, which is then viewed from different angles (see Figure 1.5). The supermassive black hole at the centre is surrounded by an accretion disc from which jets emanate perpendicularly. In the same plane as the disc there are clouds of material in orbit around the black hole. Blazars, the brightest objects, are those in which the jets are aligned with our line of sight. The emission from the core fades away as the angle from the jet axis increases.

Blazar flares emitting TeV-energy gamma-rays are believed to be produced by the relativistic jets. As in GRBs, protons are also expected to be accelerated in AGN jets. In hadronic interactions with ambient gamma-rays and hadrons, pions are produced via the Δ-resonance. While the neutral pions decay into TeV-gamma-rays and thus explain the observed spectra, charged pions are supposed to give rise to neutrino fluxes ranging from TeV to EeV energies.

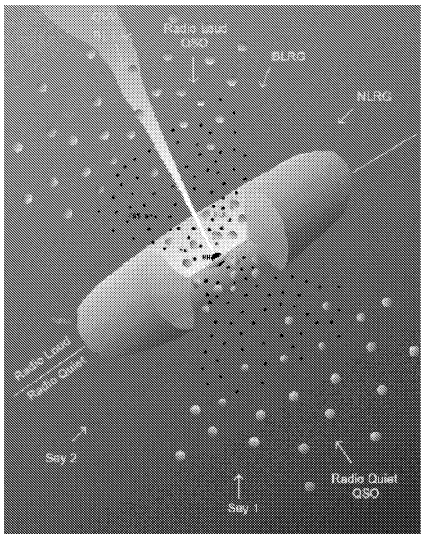

Figure 1.5: *Schematic view of what an AGN looks like depending on the angle that we view it from [16].*

Besides the above-mentioned extragalactic sources, there are a number of galactic neutrino-emitters associated with stellar objects:

- **Supernova Remnants (SNRs)**
  A supernova remnant is the structure resulting from the core collapse of a massive star into a supernova. The supernova remnant is bounded by a powerful expanding shock wave, and consists of ejected material expanding from the explosion as well as the interstellar material it sweeps up and shocks along the way (see Figure 1.6). As the shells of supernova remnants are capable of accelerating particles up to 10^6 GeV via the Fermi mechanism, SNRs are the best candidates for the origin of the galactic component of cosmic rays. Besides providing sufficient power to sustain the galactic CR-flux, they feature non-thermal power-law spectra indicating Fermi acceleration and they display chemical abundances similar to those found in cosmic rays. TeV gamma-ray emission has been observed from the Crab nebula and from numerous other SNRs measured by the HESS telescope [18],[19]. However, the gamma-ray flux cannot prove beyond doubt the acceleration of hadrons, as they might also originate from inverse Compton scattering on accelerated electrons instead of π^0-decays. Nevertheless, SNRs with TeV gamma-ray emission might also be good candidates for neutrino sources.

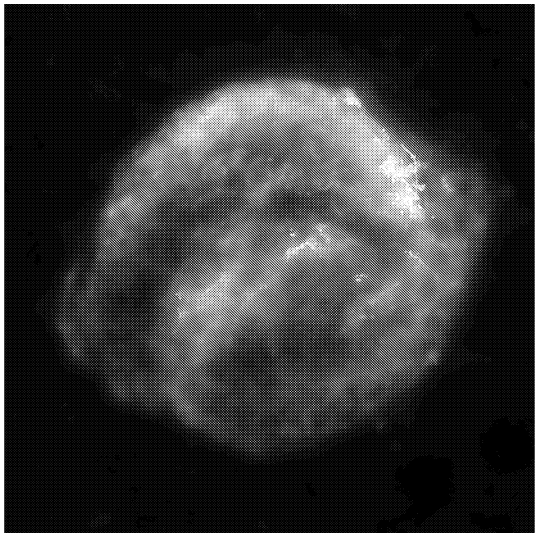

Figure 1.6: *Multiwavelength observation of Kepler's supernova remnant SN 1604. The image is a superposition of infrared, visible and x-ray images taken by the Spitzer, Hubble and Chandra space telescopes [17].*

- **Microquasars**
  Microquasars are named after quasars because they have some common characteristics: strong and variable radio emission, often resolvable as a pair of radio jets, and an accretion disc surrounding a black hole or neu-

tron star. While in quasars the black hole is supermassive (millions of solar masses), in microquasars it is of the order of a few solar masses. Also, the accreted mass in microquasars comes from a companion star, and the accretion disc is very luminous in optical regions and X-rays. A part of the radio emission comes from relativistic jets, often showing apparent superluminal motion. The jets are formed close to the black hole, and as time-scales near the black hole are proportional to the mass of the black hole, microquasars display variations on the a scale of days rather than centuries, as do ordinary quasars. Like AGNs, they are assumed to accelerate hadrons and thereby emit neutrinos. However, the maximum possible energies to which protons can be accelerated due to the gyrolimitation of Fermi acceleration are smaller by a factor of 10^4 than for relativistic AGN jets. However, due to their vicinity in our galaxy, microquasars might well contribute to the galactic CR flux and also yield detectable neutrino emissions. For example, the microquasar LS I +61 303 has been recently discovered [20] to emit VHE gamma-rays, which were recorded by the MAGIC telescope.

- **Pulsar Wind Nebulae**
  A pulsar wind nebula (also known as a "plerion") is a nebula powered by the relativistic wind of an energetic pulsar. At the early stage of their evolution, pulsar wind nebulae are often found inside the shells of supernova remnants. Unlike SNRs, they do not have a shell-type structure. Pulsar wind nebulae are believed to be powered by active rotation-powered pulsars through a relativistic wind of particles and magnetic fields. Due to the pulsar's rotation there is a very strong gradient in the magnetic field capable of accelerating charged particles. The pulsar's wind is decelerated to a sub-luminal speed across a strong standing shock. The emission from the plerion is seen beyond this radius and results mainly from synchrotron radiation of the high-energy particles injected by the pulsar in the presence of the strong magnetic field. However, neutrons escaping the plerion without adiabatic losses might represent an interesting source of high-energy neutrinos. Moreover, pulsed neutrinos from the magnetosphere might arise from secondary reactions when accelerated electrons and positrons hit the polar caps.

In addition to the potential neutrino sources relying on Fermi acceleration, there are more hypothetical neutrino emissions conceivable, which are based on relic Big Bang particles.

- **Dark matter (DM)**
  While the existence of dark matter and its proportion were precisely measured by the WMAP experiment [21], its particle nature has not yet been

revealed. Weakly interacting massive particles (WIMPs) or the lightest supersymmetric particle are favoured candidates and are thought to conglomerate in gravitational centres, where they annihilate each other. Neutrinos emerging in the decay chain may be the only observable particles due to their ability to escape from very dense regions. Therefore, a neutrino signal from the Sun or the galactic centre could provide indirect evidence of the existence and possible also the nature of WIMPs.

- **Topological defects**
  Topological defects are (often) stable configurations of matter predicted by cosmology theories to form at phase transitions in the very early universe. Topological defects arise naturally if the structure of the vacuum manifold is such that it has at least two disconnected sets of ground states which can be occupied during spontaneous symmetry breaking in the early universe. As the universe expands and cools, symmetries in the laws of physics begin to break down in regions that spread at the speed of light. Topological defects occur wherever regions with different ground state configurations come into contact with each other. Depending on the nature of symmetry breakdown, various solitons are believed to have formed in the early universe according to the Kibble-Higgs mechanism [22], such as magnetic monopoles, cosmic strings, domain walls etc. As topological defects are a concentration of energy which can move but cannot dissipate easily, they could theoretically be observed. No topological defects of any type have been observed yet, however, magnetic monopoles might be detectable by ANTARES due to their direct Cherenkov light emission or the Cherenkov light produced by the δ-rays generated by the monopole.

1.3 Bounds on diffuse high-energy neutrino radiation

The observation of ultra-high-energy cosmic rays (UHECR) may provide an upper bound for the diffuse cosmic neutrino flux. Since the observed cosmic rays above the knee cannot be confined by the galactic magnetic field, they inevitably have to be of extragalactic origin. Knowing the energy-dependent generation rate of protons in the energy range $10^{19} - 10^{21}$ eV to be [14]

$$E_{CR}^2 \frac{dN_{CR}}{dE_{CR}} \approx 10^{44} \quad \text{erg Mpc}^{-3}\ \text{yr}^{-1} \tag{1.3}$$

and assuming photoproduction of pions with total energy transfer from proton to pion, the maximum muon-neutrino intensity was estimated by Waxman and Bahcall (WB) [14] to be

$$E^2_{\nu_\mu+\bar{\nu}_\mu}\Phi_{\nu_\mu+\bar{\nu}_\mu} = 0.25\frac{ct_H}{4\pi}E^2_{CR}\frac{dN_{CR}}{dE_{CR}} \approx 1.5\cdot 10^{-8} \quad \text{GeV cm}^{-2}\ \text{s}^{-1}\ \text{sr}^{-1}. \tag{1.4}$$

The factor 0.25 arises since neutral pions and charged pions are produced with approximately equal probability, but only charged pions decay into neutrinos $\pi^+ \rightarrow \nu_\mu + \mu^+ \rightarrow \nu_\mu + \bar{\nu}_\mu + \nu_e + e^+$ where the resulting muon neutrinos carry approximately half of the pion energy.

However, extragalactic sources generally show considerable evolution in the course of cosmic time in the sense that they were much more active in the past than they are today. Therefore, redshift losses and source evolution, following the rapid luminosity-density evolution of quasi-stellar objects, were included in Eq. (1.4), leading to an increased upper bound (see Figure 1.7).

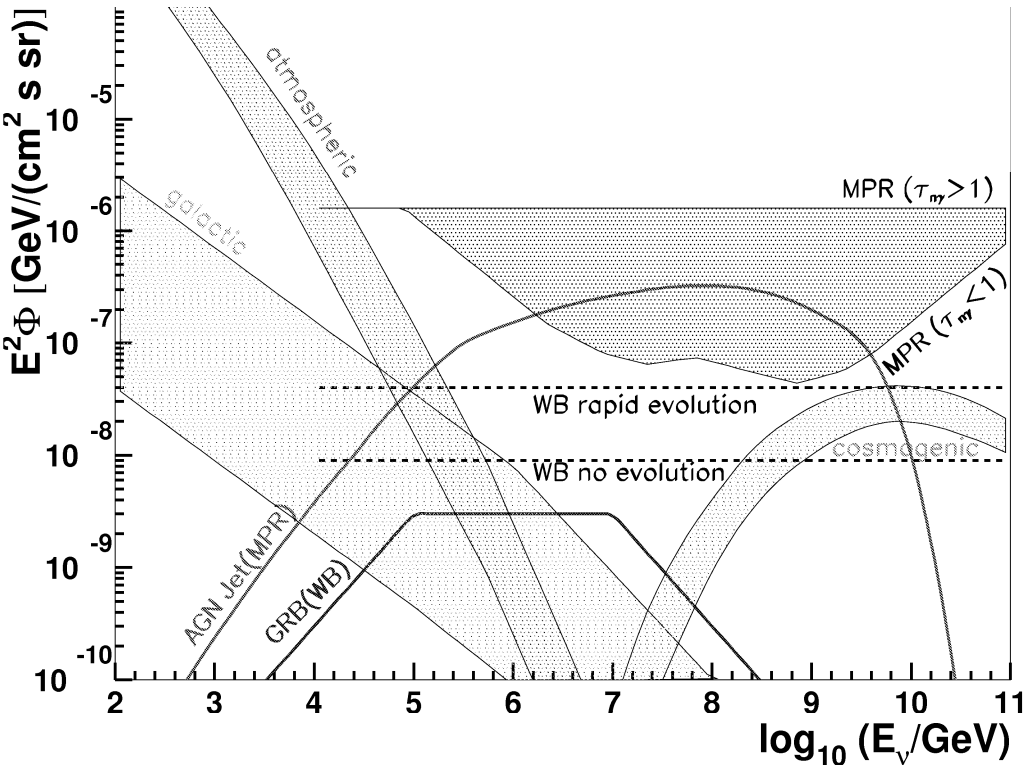

Figure 1.7: *Summary of theoretical $\nu_\mu+\bar{\nu}_\mu$ fluxes for diffuse emission from various sources.*

The upper bound proposed by Waxman & Bahcall has been extended even further by Mannheim-Protheroe-Rachen (MPR) [23] by also taking into account cases in which protons are absorbed within the source or suffer adiabatic losses in large-scale magnetic fields. It is conceivable that neutrons, which were produced in previous hadronic interactions in the source such as $p + \gamma \rightarrow \pi^+ + n$, are – unlike protons – not confined by the magnetic fields and can thus escape the cosmic accelerator without energy losses, and undergo β-decay outside the host galaxy's magnetic field. The associated maximum neutrino flux including the effects of source evolution is presented in Figure 1.7.

The upper bound according to the model of Mannheim-Protheroe-Rachen (MPR) is indicated by the shaded area between the two extremes: the straight upper line, which represents sources optically thick to pion photoproduction, from which neutrons will not be able to escape without previous interactions ($\tau_{n\gamma} > 1$), and the lower curve, which illustrates the thin case, in which neutrons can escape freely ($\tau_{n\gamma} < 1$). At low energies the allowed region for upper bounds is well above the bound obtained by Waxman and Bahcall. The MPR limit decreases to a minimum at 10^9 GeV, where it meets the WB-limit, after which it increases again. The reason for this rise is that neutrinos are received from the entire cosmic volume including the particularly active sources in the early Universe, whereas protons suffer energy losses while propagating through the CMB, thus reducing the horizon from which their sources can contribute to the measured diffuse background.

From the experimental point of view, currently operated detectors have started to approach the theoretical limits, and detectors still under construction (like ANTARES and IceCube) will soon enter the realm left open by theoretical constraints. Figure 1.8 shows the upper limits obtained by different experiments such as Frejus [24], Macro [25], Baikal [26], Amanda-B10 [27] and Amanda-II [28].

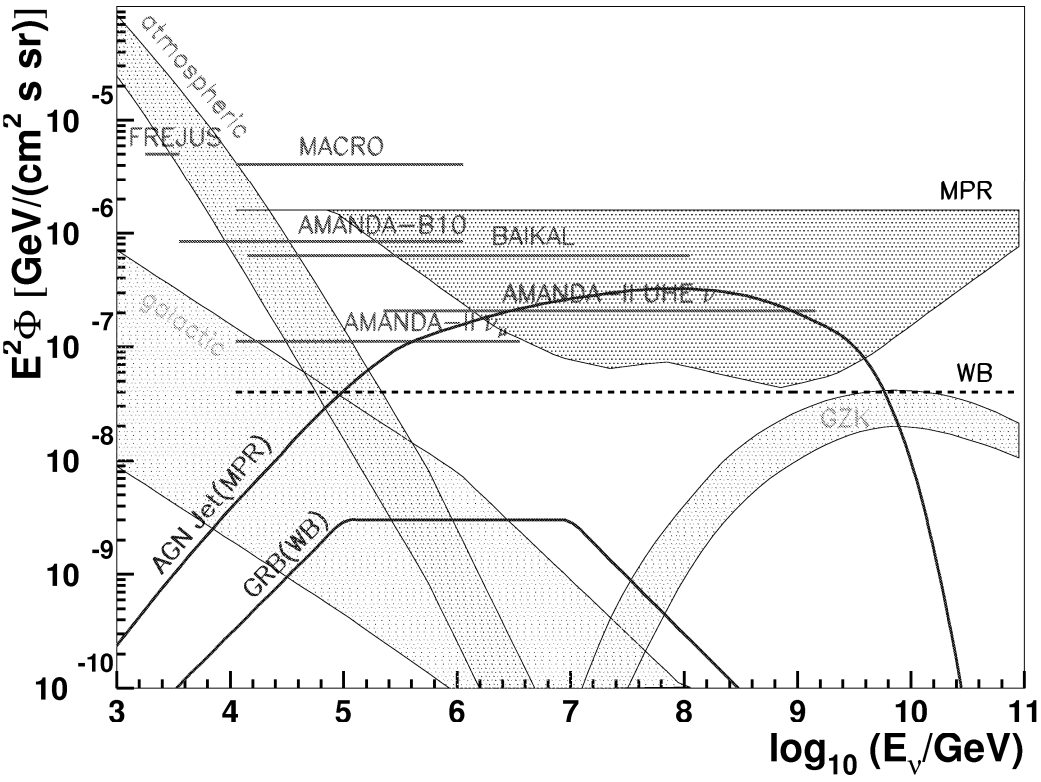

Figure 1.8: *Summary of experimental upper limits on the differential $\nu_\mu + \bar{\nu}_\mu$ flux of cosmic neutrinos.*

2 The age of neutrino telescopes

Compared to millennia-old photon astronomy, neutrino astronomy is still in its infancy due to the weakly interacting nature of neutrinos. Since the cross-sections involved are very small, neutrino telescopes need to compensate by instrumenting very large volumes of target material, which poses a technical challenge.

Following in the footsteps of the pioneering instruments, which demonstrated the detection technique and thereby discovered neutrino oscillations, present-day prototype neutrino telescopes like BAIKAL, AMANDA and ANTARES are starting to explore the high-energy neutrino sky, and will be succeeded by cubic-kilometre-scale observatories needed to pursue neutrino astronomy with better statistics.

2.1 Principles of detection

In general, neutrinos interact with nuclei via the exchange of W and Z bosons, thereby producing either leptons by charged current (CC) interactions and hadronic cascades as a result of the deep inelastic scattering processes, or the latter in neutral current (NC) interactions (see Eq. 2.2). The emerging lepton inherits the flavour $l = e, \mu, \tau$ of the incident neutrino.

$$\nu_l + N \rightarrow l + X \quad \text{(CC)} \quad (2.1)$$

$$\nu_l + N \rightarrow \nu_l + X \quad \text{(NC)} \quad (2.2)$$

The cross-section for neutrino nucleon interactions at high energies depends greatly on the parton distribution of the nucleon. Since these distribution functions have been measured in accelerator experiments only, they have to be extrapolated to cover the whole energy range relevant to astroparticle physics. For neutrino energies of up to 10^{16} eV, all the standard sets of parton distribution functions give very similar cross-sections. At higher energies, the behaviour of the parton distributions at very low values of the momentum fraction x become increasingly important, thus giving rise to uncertainties in the cross-section around 10^{20} eV [29].

In Figure 2.1 the inclusive neutrino nucleon cross-section is presented as a function of the neutrino energy. The total cross-section is the sum of charged current and neutral current partial cross-sections. At energies of below 10^4 GeV, the cross-section increases linearly in energy, whereas at higher energies the cross-section is damped by the W,Z-boson propagator term in the matrix element.

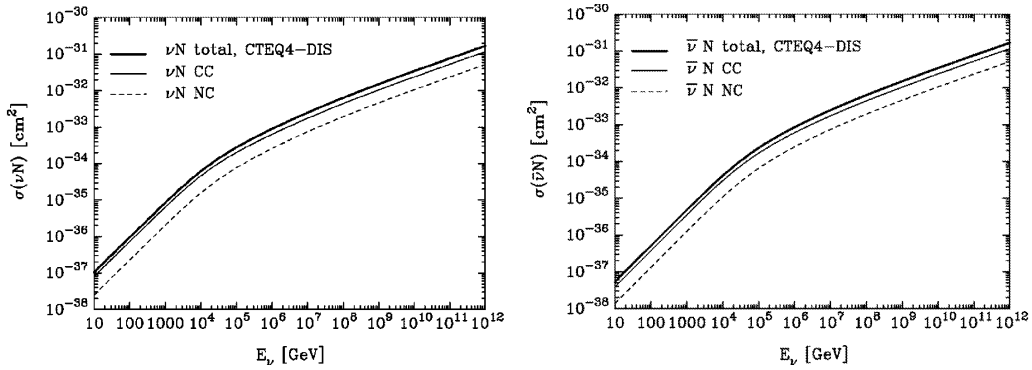

Figure 2.1: *Cross-section for $\nu_l N$ (left) and $\bar{\nu}_l N$ (right) interactions [29].*

At low energies, the anti-neutrino nucleon cross-section is smaller than the neutrino nucleon cross-section due to the dominant contribution of the valence quarks. This effect becomes negligible at energies of above 10^6 GeV, which results in a convergence of the neutrino and anti-neutrino cross-sections.

The increase in cross-section with neutrino energy suggests that neutrino detectors are expected to measure higher rates at higher energies (provided the flux is constant). However, since the cross-section is inversely proportional to the interaction length, very high-energy neutrinos are likely to interact while traversing the Earth before reaching the site of the telescope. Figure 2.2 illustrates the differential shadow factor versus nadir angle for different neutrino energies and three sets of parton distribution functions.

In the PeV energy range neutrinos are increasingly absorbed in the Earth, and at higher energies the Earth can be considered opaque to neutrinos. Tau-neutrinos are an exception to this rule because the tau lepton, which emerges from the interaction, will itself decay quickly, thus producing a new tau-neutrino with a lower energy. This decay and reproduction chain will continue until the tau-neutrino has lost sufficient energy so that the Earth eventually becomes transparent and the tau-neutrino can pass unhindered. Moreover, anti-electron neutrinos experience a significant attenuation at energies of around $6.35 \cdot 10^6$ GeV due to the Glashow [30] resonance $\bar{\nu}_e e \rightarrow W^-$.

In any case, the strategy for neutrino telescopes changes in the energy range of around 1 PeV. At energies below the shadowing effect, it is preferable for

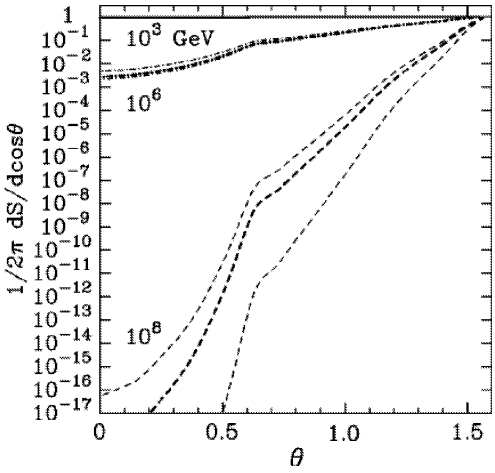

Figure 2.2: *Earth shadowing effect on neutrino propagation [29].*

neutrino telescopes to look for upward-coming events to ensure that the detected particle is a neutrino. Since the Earth acts as a filter allowing no particles except neutrinos to pass through, looking downwards ensures that only neutrinos are detected. However, atmospheric neutrinos still have to be discriminated. By contrast, at energies in the PeV range and above, when the shadowing effect becomes dominant, it is worthwhile to look for down-going events, especially since cosmic rays and their secondary particles, including atmospheric neutrinos, are no longer expected at such high energies.

2.2 Optical Cherenkov technique

The most established technique for the detection of high-energy neutrinos already used by the precursor instruments is the optical Cherenkov method in a transparent medium. Charged particles at relativistic energies which move faster than light in the medium are known to emit Cherenkov light, thereby dragging a cone of light in their wake with an opening angle corresponding to $\cos\theta_c = 1/\beta n$ (see Fig. 2.3). Here, $\beta = v/c$ is the velocity of the particle relative to the speed of light in vacuum, and n is the refraction index of the medium. The radiation arises due to effective polarisation of the medium, which is induced by the propagation of the charged particle at a velocity higher than the local speed of light and the subsequent relaxation of the atoms along the path.

The need to instrument large volumes of optically transparent and inexpensive target materials causes the natural resources of ice and water to become the

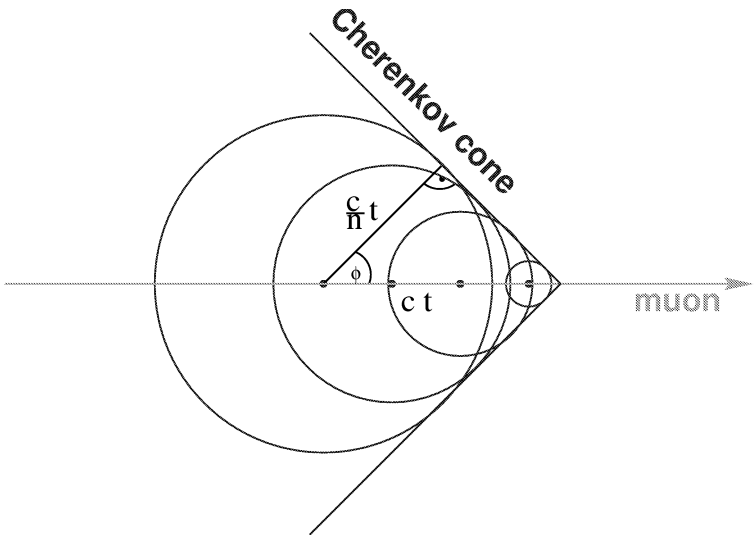

Figure 2.3: *Schematic view of the formation of the Cherenkov cone and derivation of its opening angle.*

focus of interest. Currently operated neutrino telescopes use the Antarctic ice, deep-sea water or the fresh water of Lake Baikal. Each of the chosen target media has its advantages and disadvantages: Ice seems particularly well-suited from the point of view of deployment since it provides a solid platform from which the detector elements can be lowered into the medium and installed. Lake Baikal, which freezes in winter, provides a layer of ice for deployment as well as maintenance work. By contrast, sea experiments need boats and submarines or remotely operated vehicles (ROVs) suited for the deep sea in order to install and maintain the detector elements. Also, the background noise in sea water is much greater than in ice due to ^{40}K-decays and bioluminescence, which generates about ca. 60 kHz per photomultiplier tube (PMT), whereas the detector in ice is affected only by the phototube's dark noise, which is around 500 Hz per PMT.

The advantages of water-based detectors are the uniformity of the medium and the detector response. While the Antarctic ice has incorporated dust layers and bubbles, water is always homogeneous, which facilitates the understanding of the detector efficiency. Moreover, the scattering length λ_{sc} is much shorter in ice, but the absorption length λ_{abs} is shorter in water (see Table 2.1). The resulting attenuation length λ_{att}, which is the inverse sum of the scattering and absorption length,

$$\frac{1}{\lambda_{att}} = \frac{1}{\lambda_{sc}} + \frac{1}{\lambda_{abs}}$$

is around 46 m in the Mediterranean and 17 m in Lake Baikal and the Antarctic

Table 2.1: *Comparison of optical properties w.r.t. Cherenkov detection for blue and UV (in parentheses) light [31],[32].*

Parameter	Mediterranean Sea	Lake Baikal	Antarctic Ice
refraction index	1.35	1.35	1.32
Cherenkov angle	42°	42°	41°
Scattering length [m]	265(122)	104(35)	20
Absorption length [m]	60(26)	19(8)	110
Attenuation length [m]	46(23)	17(7)	17

ice. As a result, the angular resolution for muon neutrinos is below 0.5° for ANTARES[1] and around 2°-3° for AMANDA.

2.3 The ANTARES experiment

The ANTARES neutrino telescope is being installed at a depth of 2400 m in the Mediterranean, 40 km off the French coast near Toulon. Due to its location (42°50' N and 6°10' E) it has an annual sky coverage of 3.5π sr, with 0.5π sr instantaneous and 1.5π sr integrated common field of view with AMANDA/IceCube in the sub-PeV energy range, where both telescopes are restricted to looking below the horizon (see Figure 2.4). Hence neutrino telescopes in different hemispheres are complementary to each other with respect to their field of view. However, ANTARES has the special advantage of being able to observe the galactic plane with its numerous candidate neutrino sources for a large part of the day (67% on average). From the point of view of multi-messenger observations, the Mediterranean site is quite auspicious due to the inherent correlation between TeV-γ-sources and neutrino sources if hadronic acceleration is involved. Hence multi-messenger observations are important not just from the astrophysical point of view but can be used to leverage the signal to background ratio (see Chapter 6).

Detector setup

Upon completion, the ANTARES detector will consist of 12 lines (see Figure 2.5) that are anchored to the sea bed and tightened by a buoy at the top end (450 m

[1] in the energy region above 10 TeV, where the resolution is dominated by the reconstruction and not the intrinsic deviation between muon and neutrino direction,

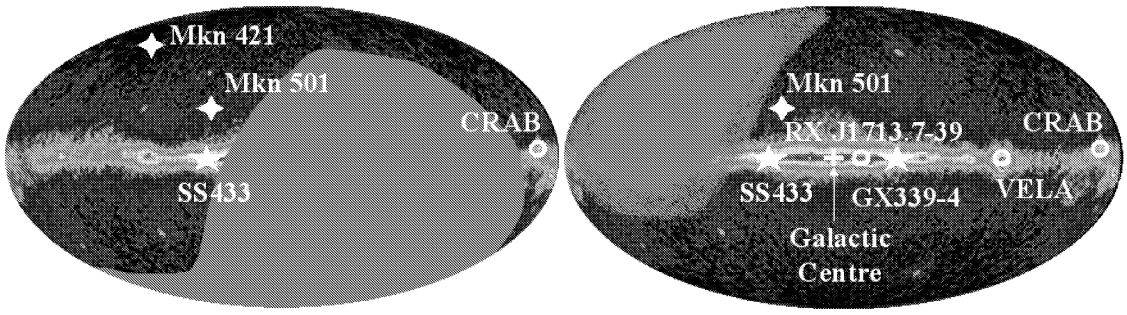

Figure 2.4: *Field of view in galactic coordinates of a neutrino telescope at 2π downward sensitivity for location at the South Pole (left) and the ANTARES site in the Mediterranean (right) superimposed on the EGRET sky map with prominent γ-sources added.*

height). The key components are the so-called storeys, each equipped with three optical modules (OMs) consisting of a 17" pressure-resistant glass sphere, which houses a 10" Hamamatsu R7081-20 photomultiplier, and a titanium electronics container, the so-called Local Control Module (LCM), which accommodates the electronics needed to digitise the OM signals, the compass, tiltmeter and various other optional devices connected to the LCM, such as a hydrophone or an optical beacon. The OMs are inclined at an angle of 45° towards the sea bed, thus looking aslant downwards and thereby having an excellent view of the Cherenkov photons emitted from upward-going muons, which is in accordance with the sub-PeV detection mode. The photomultipliers are capable of detecting single photo-electrons with the time resolution of 2.7 ns being limited by the transit time spread.

Each detector line comprises 25 storeys spaced at intervals of 14.5 m, with the lowest storey starting at 100 m above the sea bed. The storeys are interconnected with an electro-opto-mechanical cable, which supplies the active components with electric power and control signals and transfers data from the storey to the bottom of the line.

The layout of the lines is discernible in Figure 2.5. Submersible-deployed electro-optical interlink cables connect each line to the junction box, which acts as a fan-out between the lines and the main electro-optical cable to the shore station. In addition to the 12 principal instrumented detector lines, the Mini Instrumentation Line with Optical Modules (MILOM) and the prospective Instrumentation Line (IL) will be part of the detector setup whose function is that of constantly monitoring the environmental parameters and providing a platform for interdisciplinary deep-sea studies.

Currently, two completely instrumented detector lines have been collecting data

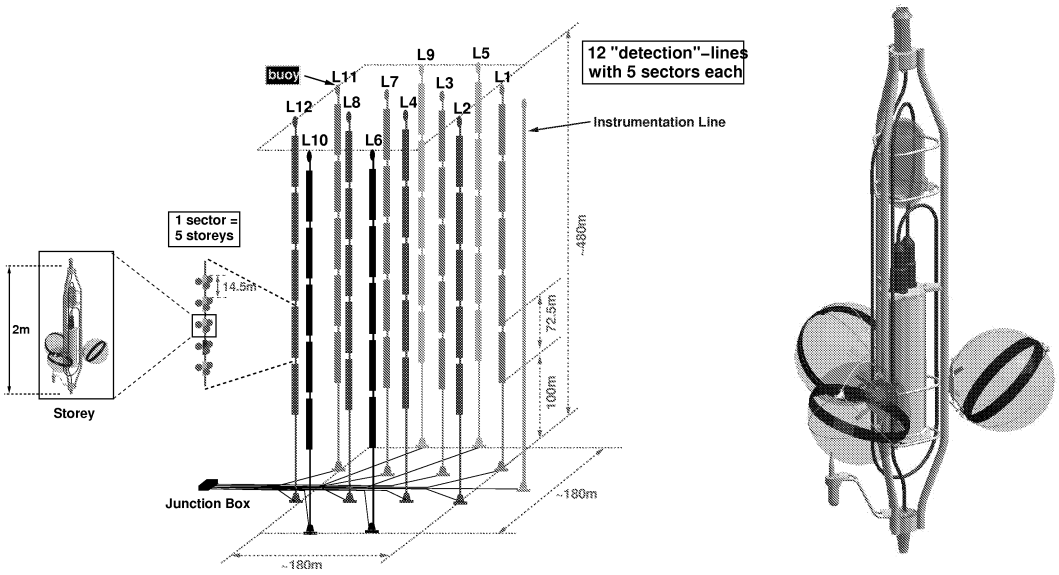

Figure 2.5: *Left: Schematic view of the planned arrangement of the detector strings at the ANTARES site. Right: The optical module frame as the basic detector element.*

continuously since their connection on 2/3/2006 and 22/9/2006. The MILOM is still being used to provide data on the environmental parameters. By the end of 2007 the detector is expected to be complete and fully functional in accordance with the design specifications.

Data acquisition and trigger

The default readout mode is the transmission of the digitised time and amplitude signal of any incoming light above a certain threshold, known as the "all-data-to-shore" concept (see [33] for a detailed description).

The readout architecture of the ANTARES detector has several levels of multiplexing of the photomultiplier signals. The first level is in the LCM, where the analogue electrical signal of each photomultiplier is digitised by the Analogue Ring Sampler(ARS)[2] before being buffered by the Field Programmable Gate Array (FPGA) and then sent to the processor, which outputs the signals of the

[2]Each OM has two ARS chips to avoid dead time whilst one of them is digitising the signal. The ARS readout has two modes: in the SPE mode the hit time and integrated amplitude are recorded, whereas in waveform mode the pulse waveform is digitised in 128 samples at a rate of 1 GHz.

three OMs on the storey on an ethernet optical link. Five storeys are grouped together to form a sector, which share a common ethernet switch located in the Master Control Module (MLCM) of every fifth storey. This MLCM represents the second level of multiplexing, since the combined output is sent on a particular wavelength to the String Control Module (SCM) at the bottom of each line, where the output from the 5 MLCMs of the complete line is multiplexed on to a pair of optical fibres. These fibres are connected via interlink cables to the junction box, which then gathers the data from all lines onto the 48-fibre main electro-optical cable going to the onshore PC farm.

To ensure that all ARS chips are synchronised, a common clock signal has to be provided by a clock system. A master clock onshore generates a 20 MHz clock signal, which is distributed to all offshore clock transceivers on each LCM. This local clock synchronises the ARS with a relative time accuracy of 50 ps. The output of each ARS chip within a certain time window is buffered in a frame, whose length can be adjusted from 10 to 100 ms. All frames belonging to the same time window are sent to a single PC and form a time slice (see Figure 2.6).

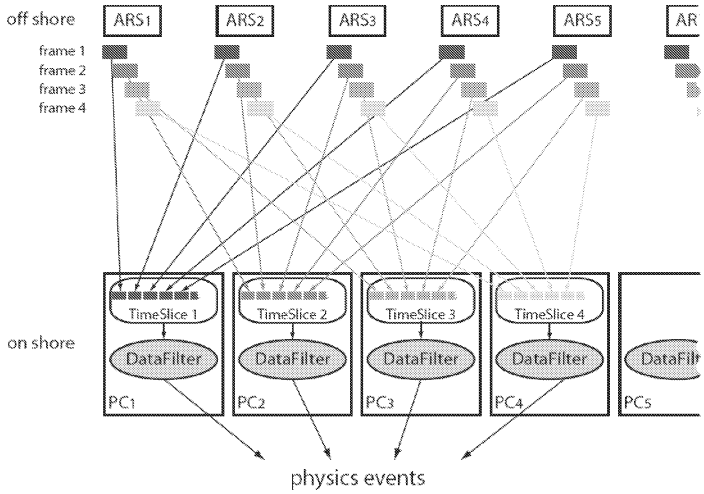

Figure 2.6: *Data processing based on TimeSlices. The DataFilter programme running on each PC processes the data in the TimeSlice.*

The onshore handling of the raw data is done in the form of time slices and is subject to the DataFilter programmes, which have several algorithms implemented to provide for different physics signals. For instance, the standard muon filter seeks for typical muon signals by scanning in all directions. By contrast, the Flash-Back programme, which is activated by a GRB alert message (see [69] for more details), searches only in the direction of the potential GRB to see whether any particular signal could be attributed to a neutrino coming from that particular direction.

In general, when a time slice is complete it is passed down to the trigger algorithm for further processing. The trigger logic again has several levels of processing [34] and is optimised to select the hits which are likely to originate from a physics signal rather than the random background:

- **L0: conversion and calibration of raw data**
  The raw data of a time slice is converted into a data format readable by the trigger software and at the same time the charge and time of the hits are calibrated according to a table in the database.

- **L1: local trigger search**
  The first-level trigger focuses on local coincidences and big hits, e.g. it looks either for hits arriving in coincidence on the same storey within a time window of 20 ns or for hits with an amplitude above the threshold of about 2 photoelectrons (pe) (see the paragraph about calibration below for more details).

- **L2: global trigger search**
  The second-level trigger looks for causally related hits, called clusters. It scrutinises all hits to see whether they could in principle have been produced by unscattered light originating from a muon trajectory. Taking into account the geometry of the detector, the maximal causal time allowed is `tMaxCausal` $= 2.2\mu$s. Since the muon is highly relativistic, the lowest velocity is c/n and the causality relation hence reads

$$|\Delta t| < \frac{|\Delta \vec{r}|}{c/n}$$

- **L3: merging of overlapping events**
  Each event contains a snapshot of all hits within a certain time window around the cluster. This time interval of snapshot hits is constructed such that it starts `tMaxCausal` earlier than the last triggered hit and ends `tMaxCausal` after the first triggered hit. Two events overlap when the cluster of one event falls into the snapshot of another event. In this case, the hits in both clusters are merged to form a single one and the corresponding snapshot is redefined.

- **L4: event building**
  All raw hits of a snapshot are collected and combined to form a physics event, which is then stored on disk for further processing by the reconstruction software.

Calibration

The timing resolution of the detector is dominated by the transit time spread (TTS) of the photomultipliers, which is the spread in measured times due to the photoelectron (pe) taking different lengths of time between production at the photocathode and arrival at the last dynode. The TTS is measured in situ using an LED built into the OM, which is fired at a given time. The time difference between the LED trigger and the hit time recorded by the ARS is attributed to the TTS, and is found to be 2.7 ns at FWHM.

Equally important are the timing calibrations using external optical beacons, such as four LED beacons along the top of each detector line and one LED at the MILOM together with a Nd-YAG laser beacon located at the base of the MILOM. The individual LEDs in the beacons are pre-selected in order to have very short rise times of about 2 ns in the 10%-90% signal range and 5 ns at FWHM.

Figure 2.7 shows an example of a measurement in which the three OMs of storey 3 of Line 1 were illuminated by the flashes of the MILOM LED beacon. As can be seen, the two OMs facing the MILOM receive direct light, thus having narrow Gaussian distributions of 0.6-0.7 ns, whereas the OM on the opposite side of the storey mainly sees scattered light, which becomes manifest in the long tail of late photons.

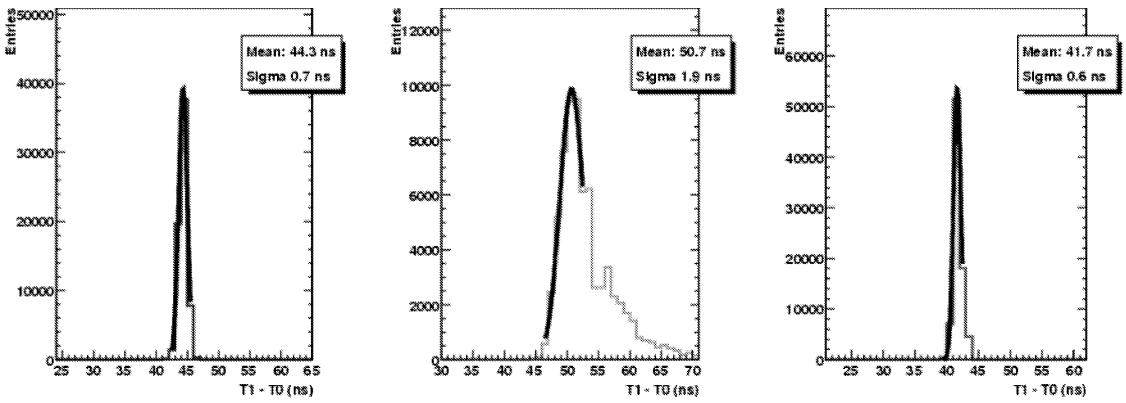

Figure 2.7: *Data recorded in storey 3 of Line 1 during timing calibrations with the MILOM LED beacon.*

For charge calibration, it is necessary to know the response of each PMT to a single photoelectron. A typical measurement is shown in Figure 2.8. The Analogue to Digital Converter (ADC) channel is proportional to the charge deposited at the anode, each channel corresponding to 0.25 pC. The charge spectrum starts

with a pedestal, which represents the intrinsic noise of the PMT. Due to this feature no measurement is possible below this threshold, which corresponds roughly to 0.3 pe. For a given number of photoelectrons the deposited charge follows a Gaussian distribution, which can be fitted. Therefore, by measuring a given charge distribution, it is possible to calculate the corresponding number of photoelectrons. Although it may seem unphysical, fractions of photoelectrons are also possible values.

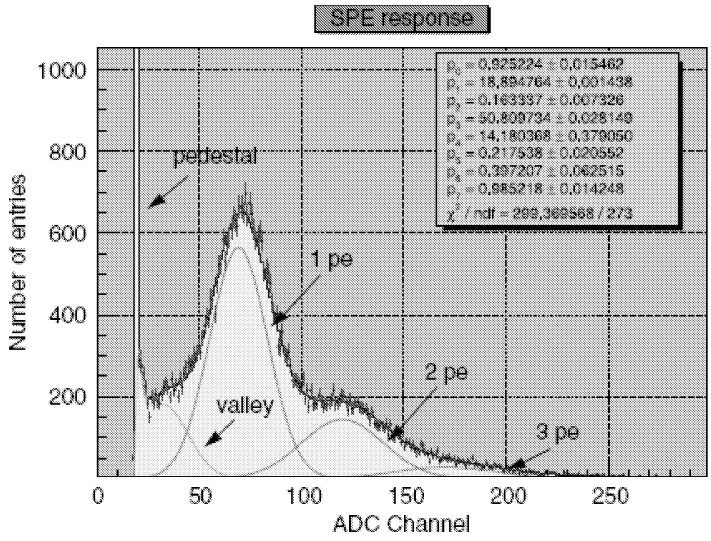

Figure 2.8: *Example of a charge spectrum [35].*

Positioning system

Since the lines of the ANTARES detector are flexible and thus move in the water as a result of the sea current, the position and orientation of each OM have to be constantly monitored to ensure a precise track reconstruction. For this purpose, five receiving hydrophones are installed on each line, which, together with the network of emitting transponders on the sea bed, can be used for acoustic triangulation.

In addition to the acoustic positioning system, compasses and tiltmeters have been installed on the TCM2-cards in each LCM to measure the components of the magnetic field (B_x, B_y, B_z) and the pitch and roll values of the LCM, thereby providing a relative orientation measurement along the line. The magnetic field vector is a prerequisite for calculating the heading of the storey, which is the angular deviation of OM0 from north in the plane of the OMs. The azimuth and

zenith angles of each OM can be computed from the heading and the inclination of the storey. The hydrophone positions obtained by means of acoustic triangulation are absolute positions and therefore used as a reference for the computing of absolute OM positions and at the same time they provide a consistency check.

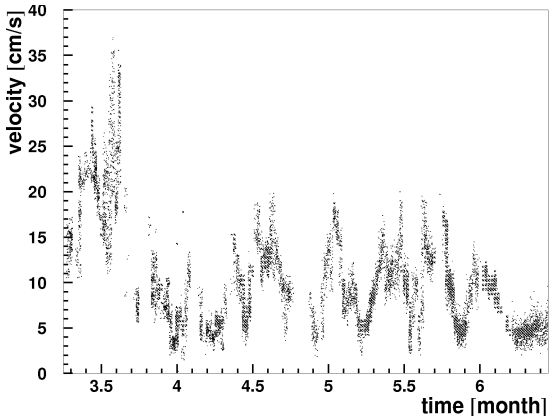

Figure 2.9: *Sea current velocity obtained by direct measurement with the ADCP monitor (black) and from the reconstruction of the line shape (red). [36]*

The expected correlation between the sea current velocity and the line shape is illustrated in Figure 2.9, where the velocity of the sea current is shown as obtained from direct measurements with the acoustic doppler current profiler (ADCP) and from the reconstructed line shape. The higher the velocity of the sea current, the greater the incline of the storeys on the line. The zenith angle of the storey therefore increases with the velocity of the current. On the other hand, in the case of strong sea currents, the azimuth angle traces the direction of the sea current, since the storey aligns with the current to produce the best stream-lined shape possible. This is the case when one of the three OMs points directly into the current. If the sea current is weak, there is no constraint on alignment, and neighbouring storeys will not display similar headings.

2.4 Optical background in the deep sea

The optical properties of the deep sea have a critical impact on the detector performance. Not only do scattering length and absorption have to be taken into consideration but also important sources of background light prevalent in the deep sea, which are recorded by the PMTs and can be mistaken for Cherenkov light, thereby contaminating the neutrino signal.

One class of background light is generated by radioactive decay of potassium-40, which occurs naturally in salt water but also in the glass spheres housing the PMTs. Two decay modes have been observed, the β-decay with a branching ratio of 89.3% being more common than the electron-capture process:

$$^{40}K \rightarrow {}^{40}Ca + e^- + \bar{\nu}_e \qquad \beta\text{-decay (2.3)}$$

$$^{40}K \rightarrow {}^{40}Ar^* + \nu_e \rightarrow {}^{40}Ar + \gamma. \qquad \text{e-capture (2.4)}$$

With an energy of 1.5 MeV the γ scatters to produce Compton electrons, which in turn will generate Cherenkov photons due to their high energy. Similarly, the electron produced by the β-decay will also emit Cherenkov radiation. Both processes give rise to a continuous and random background with an expected rate of 40 kHz per 10" PMT. Since this rate depends only on the salinity, which remains constant over time, it is referred to as the baseline rate.

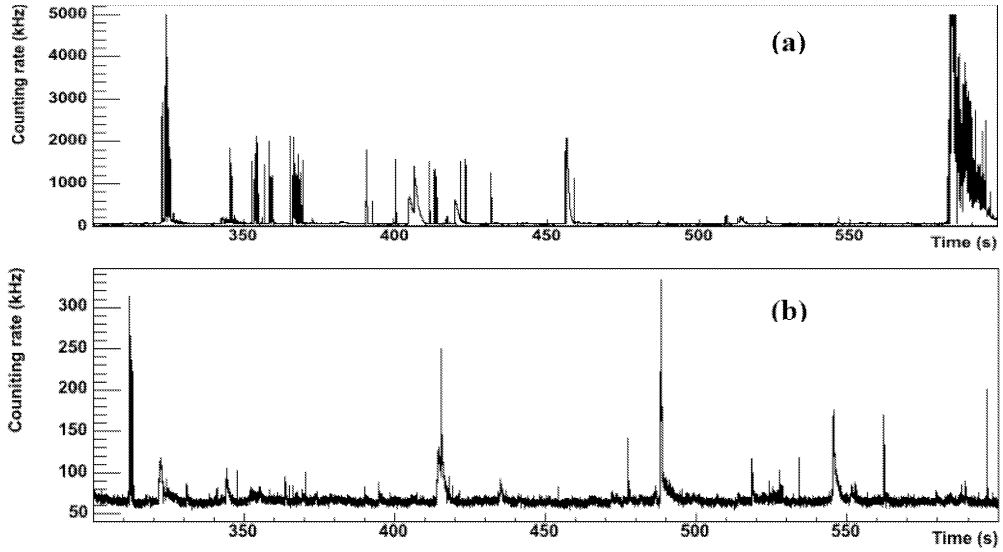

Figure 2.10: *Raw counting rates measured with a photomultiplier of the ANTARES Prototype Sector Line. Two different excerpts are shown, featuring an optically active (a) and a quiet (b) 5-minute period.*

However, there is another contribution to the optical background in the deep sea known as bioluminescence. Various sea-dwellers ranging from microorganisms to deep-sea fish emit light for purposes of communication, hunting, etc. The microorganisms, especially dinoflagellates – a form of unicellar algae – are known to emit bluish flashes of uncorrelated light, thereby contributing significantly to

the random background. The overall baseline rate thus rises from 60 kHz per 10" PMT in quiet periods to many hundred kHz in active intervals (see Figure 2.11). To take into account these variations, the baseline rate is recalculated every 5 minutes by averaging the counting rate during the 5-minute time interval.

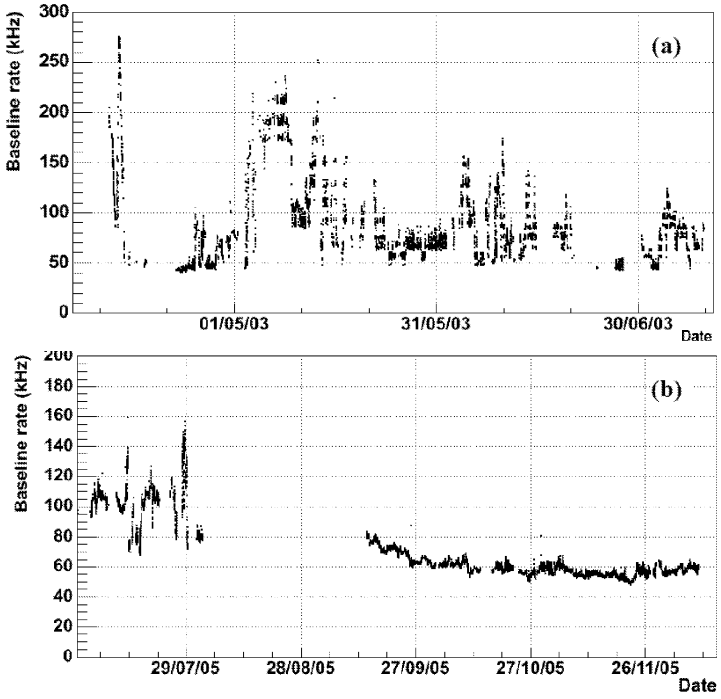

Figure 2.11: *Measurement of the baseline rate at the ANTARES site during a period of several months. (a) with the PSL in 2003 and (b) with the MILOM in 2005.*

Moreover, macroscopic organisms featuring special bioluminescent organs are capable of generating visible flashes of light. If this bioluminescent activity occurs in the vicinity of a PMT, a large burst signal is recorded above the baseline. Due to the locally increased photon counting rate (see Figure 2.10) over a long period compared to the duration of a typical neutrino event, these burst signals are easily identified, and the affected PMTs can be removed temporarily from the event-reconstruction algorithms. In this context, the burst fraction rate is defined as the fraction of time during a 5-minute interval in which the counting rate of a PMT exceeds the baseline rate by more than 20%.

As studies of the MILOM data have shown, there is a strong correlation between the burst rate and the velocity of the sea current. Above a sea current of 4 cm/s the burst rate increases quickly and reaches almost 50% (see Figure 2.12) due to the stimulated bioluminescence activity, which is considered to result from me-

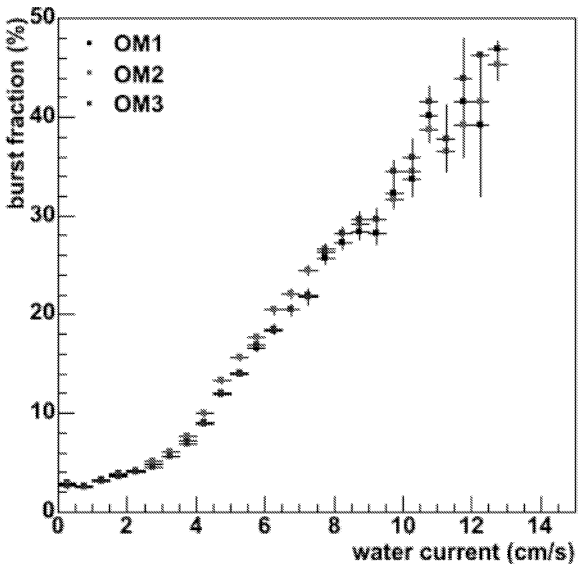

Figure 2.12: *Correlation between the burst fraction and the velocity of the sea current observed in the MILOM 2005 data.*

chanical excitation of organisms by turbulences in the wake of the detector components. However, although bioluminescence bursts can be easily eliminated, they still introduce some dead time on the affected PMTs, which reduces the overall performance of the ANTARES detector. By contrast, the bioluminescent activity leading to an increase in the baseline rate cannot be removed a priori, but its effects on track reconstruction and detector performance have to be studied and the reconstruction algorithms adapted to suit conditions with variable baseline rates.

3 ANTARES detector performance under high optical background

To assess and improve the detector capabilities for muon-neutrinos at high optical background rates, Monte Carlo (MC) studies were conducted, starting with a full simulation of muon-neutrinos. The already existing reconstruction algorithms were reviewed and modified to suit variable baseline rates. The purity of the altered reconstruction algorithm was tested on atmospheric muons, and the performance of the detector was assessed with particular regard to effective volume and area as well as the angular resolution – the key parameters of any telescope.

3.1 Simulation and analysis chain

For the generation of Monte Carlo signal events, simulation tools provided by the ANTARES software packages were used. The MC neutrino simulation and analysis chain is presented in Figure 3.1.

Neutrino-induced muons were simulated using the `Genhen` programme, which allows the user to choose the energy spectra of the generated neutrinos. While atmospheric neutrinos form a background over the entire sky with a steeply falling spectrum of $dN/dE \propto E^{-2.7}$, the energy spectrum of shock-accelerated cosmic neutrinos is expected to be as hard as E^{-2}. The muon-neutrino samples used for this study were generated in the energy range of 100 GeV - 100 PeV with a spectrum of $E^{-1.35}$ to ensure better statistics at high energies. The muon tracking and Cherenkov light generation were performed by the `Geasim` and `KM3` packages, which are described in detail below.

The cosmic-ray-induced muons, which form an important background for muon-neutrinos, were already simulated with the `CORSIKA` 6.014 package [37] for different energy ranges of the primary cosmic rays: 1 - 10 TeV/nucleon, 10 - 100 TeV/nucleon and 100 - 10^5 TeV/nucleon. Two zenith angle bins 0° - 60° and 60° - 85° were also chosen for the production [38]. The QGSJET model [39]

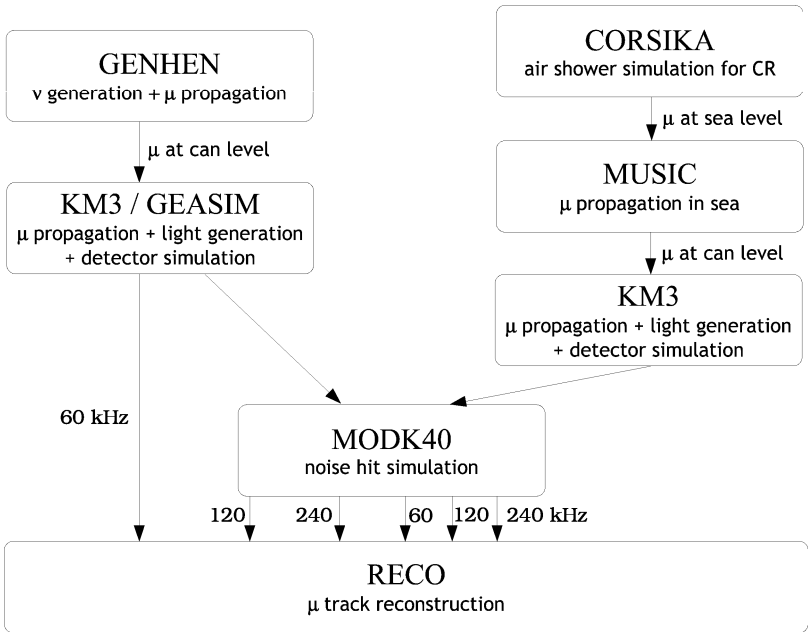

Figure 3.1: *Overview of the simulation and analysis chain. See text for more details.*

was used to simulate high-energy hadronic interactions. The muons with sufficient energy to reach the sea level were tracked down as far as the vicinity of the detector using the `MUSIC` [40] package. The muon tracking in the detector and light generation were again performed by `KM3`.

Random background noise corresponding to a baseline rate of 60, 120 and 240 kHz was added to all muon samples using `ModK40` in order to study the effects of optical background on track reconstruction and detector performance.

Event generation and muon propagation

`Genhen` [41] is used as event generator for all neutrino flavours up to energies of 10^9 GeV, where it is limited by the muon and tau propagation codes. The neutrino interactions are based on the LEPTO package [42] to simulate deep inelastic scattering, and the RSQ package [43] is used for resonant and quasi-elastic events. The CTEQ6D parton distribution functions [44] are used as default. Muon-neutrinos can be generated according to the user-defined abundance, energy range, power law spectrum and zenith angle distribution. The direction is sampled from an isotropic distribution or to correspond to a point source with a given declination. Moreover, a cylindrical volume, referred to as "can" (see Figure 3.2), can be specified at a distance around the detector. For events produced inside the can, both a muon and hadronic shower are generated and stored,

whereas for events produced outside the can but still within the total generation volume V_{gen} only the muon is generated and stored in case it propagates to reach the can. By default, the can size exceeds the instrumented volume by 200 m in all directions except from below, where it is bounded by the sea floor, from which no Cherenkov light will escape to reach the detector.

Earth shadowing effects (see chapter 2.1) are also taken into account by calculating the transmission probability of the generated neutrino according to its incident direction and energy. For a known density profile of the Earth $\rho_E(r)$, the integrated column density $\rho_l(\theta_\nu) = \int_L \rho_E(r)dL$ can be computed from the neutrino's zenith angle. The overall survival probability thus depends on the neutrino's energy and zenith angle:

$$P_E(E_\nu, \theta_\nu) = e^{-N_A \sigma(E_\nu)\rho_l(\theta_\nu)}. \tag{3.1}$$

This shadowing effect strongly suppresses the neutrino flux at energies close to the PeV range and especially for vertical neutrinos, whose attenuation is most pronounced due to the large amount of traversed matter.

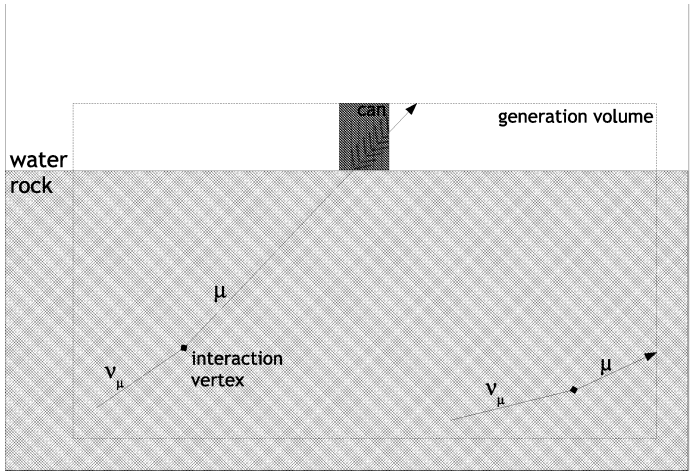

Figure 3.2: *Schematic view of the detector geometry at different stages of the event simulation chain for neutrinos.*

For the simulation of high-energy muon propagation to the can, the muon energy loss mechanisms (see Figure 3.3) and muon ranges in rock and water have to be taken into consideration. At low energies, the muon loses its energy continuously, mainly by ionising the atoms of the traversed medium in accordance with the Bethe-Bloch formula. The energy transferred to the atomic electrons by scattering is low, except in some rare cases where "knock-on electrons" are produced, also referred to as δ-rays, which are likewise capable of producing Cherenkov

light. In the TeV energy region muons start to radiate Bremsstrahlung or produce e^-e^+ pairs due to their interaction with the electric field of the nucleus. For these processes, the energy loss of the muon is approximately proportional to its initial energy. At very high energies, photonuclear processes, in which a virtual photon is exchanged directly with the nucleus, are becoming increasingly important.

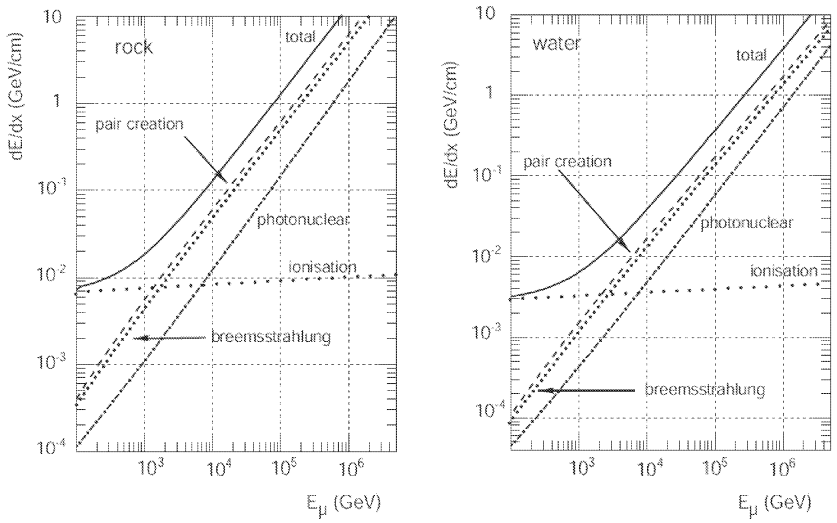

Figure 3.3: *Total and partial energy losses of muons in water (left) and standard rock (right) as a function of muon energy [45].*

Detector response simulation

Further tracking of the muons inside the can volume and light generation is done either by the `Geasim` package or the `KM3` [46] package. `Geasim` is based on `Geant 3.21` [47] and provides a full tracking algorithm for all particles. The number of Cherenkov photons emitted by each particle and their arrival at the OMs are calculated analytically, thereby including the measured attenuation length. However, scattering of Cherenkov light is not taken into account, which clearly detracts from a precise description of the detector medium.

By contrast, the `KM3` package allows a full simulation of the ANTARES detector response to the passage of high-energy muons and electromagnetic showers only, including the effect of photon scattering in water. The muon tracking is performed by `Music` [40], which computes the muon energy losses in one-metre steps and also takes into account multiple Coulomb scattering. Unlike `Geasim`, the Cherenkov photons are not generated and propagated individually due to their

numerousness at high energies, which would lead to time-consuming processing. Instead, KM3 uses "photon tables", which have been precalculated using Geant 3 to store the distributions of the numbers and arrival times at the OMs at different distances, positions and orientations with respect to a given muon track or electromagnetic shower. This method clearly improves the simulation speed although it has incorporated the effects of light scattering in water.

Photon scattering is described in terms of two types of scattering centres, generally referred to as Rayleigh scattering, which occurs on particles much smaller than the wavelength of light (molecules), and Mie scattering from spherical particles larger than about a tenth of the illuminating wavelength, e.g. sedimentary particles or microorganisms. The latter shows a strongly forward peaked angular distribution, whereas the angular distribution of Rayleigh scattering, governed by the $(1 + \cos^2\theta)$ term, is symmetric in the plane normal to the incident direction of the light, and so the forward scatter is equal to the backwards scatter. Scattering has a major impact on the reconstruction algorithms due to the time delay imposed on the photons and the change in the angle under which scattered photons hit the OMs.

The response of the OM to the Cherenkov photons is implemented in both packages, Geasim and KM3. It comprises the angular acceptance of the OM depending on its orientation with respect to the direction of the incident photon (see Figure 3.4 right) and the quantum efficiency of the PMT as a function of wavelength. However, the overall quantum efficiency of the OM decreases towards shorter wavelengths due to the effect of the glass sphere and the optical gel in which the PMT is embedded (see Figure 3.4 left).

The other key parameters for simulating the OM concern the timing response, such as the transit time spread (TTS) already mentioned in chapter 2.3 and the dead time. The ARS chip integrates the analogue signal from the PMT over a time window of 25 ns and digitises the integrated signal before output. This operation causes a dead time of 250 ns, in which the ARS cannot process any more signals. To minimise the dead time each PMT is equipped with two ARS so that the second can take over signal processing whilst the first is occupied. These effects of the front-end electronics are included in the detector simulation: two or more photons arriving within a time interval of 25 ns in a PMT cannot be separated due to signal integration during this time period. Instead, their signals are merged, producing a hit with higher amplitude – corresponding to several photoelectrons – and the hit time corresponding to the arrival of the first photon. Other effects of the front-end electronics such as afterpulses, which also cause a higher amplitude although only a single photoelectron is generated at the photocathode, are not incorporated into the simulated detector response. The TTS is taken into account by smearing every hit time according to a Gaussian distribution with $\sigma = 1.3\ \text{ns}/\sqrt{N_\gamma}$, where N_γ is the number of simultaneously

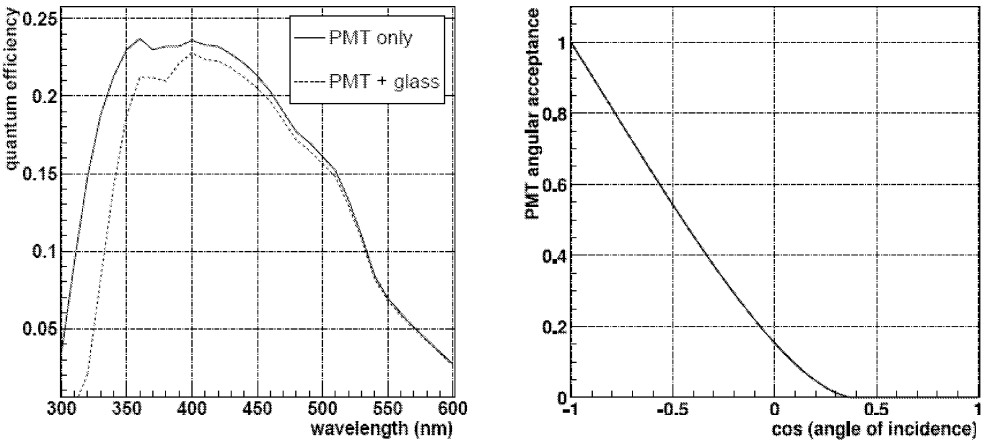

Figure 3.4: *Left: Quantum efficiency of the PMT as a function of wavelength for the bare PMT and the PMT embedded in a glass sphere. Right: Angular acceptance of a PMT as a function of the incident photon angle.*

detected photons.

In addition to the hits generated by the Cherenkov light of the tracked particles, hits from the background noise are included randomly to simulate the baseline rate. The background rate of a simulated sample of events can be changed using the `ModK40` software, which is part of the `Geasim` package. In this work, event samples have been generated with the default value of 60 kHz per PMT – corresponding to periods of very low bioluminescent activity – and altered to 120 kHz and 240 kHz for busy periods.

3.2 Muon track reconstruction and selection criteria

The trajectory of neutrino-induced muons passing the detector is characterised by the interaction vertex position, the direction and the energy. The reconstruction algorithm computes these parameters from the time and amplitude information provided by the hits in the OMs, whose position and direction at any instant are known from in-situ line alignment.

The existing muon reconstruction algorithm `AartStrategy` has been used to analyse the effects of high background noise and also served as a starting point for the development of a robust muon reconstruction strategy applicable at variable baseline rates from 60 to 240 kHz. The `AartStrategy` is a complex algorithm

consisting of several consecutive hit selection and fitting procedures. In the following, a brief synopsis of the key components of the strategy is given. The detailed description of the `AartStrategy` can be found in [48].

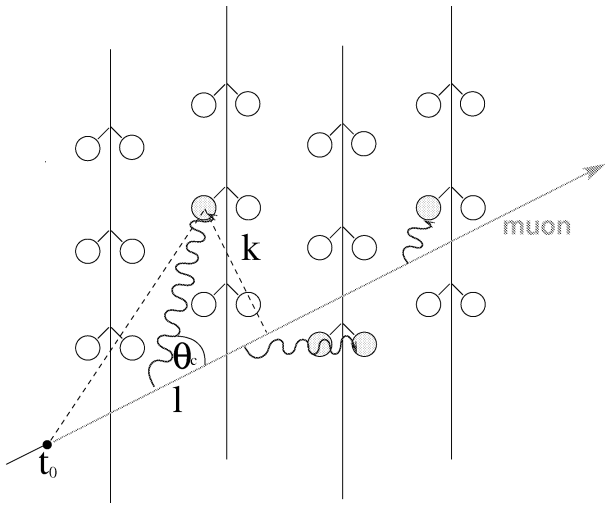

Figure 3.5: *Geometry of the neutrino-induced muon track and Cherenkov light relation in the detector.*

The original `AartStrategy`

As a first approximation, the muon track is assumed to be a straight line starting at the interaction vertex at the time t_0 and radiating Cherenkov photons at a specific angle, referred to as the Cherenkov angle θ_C (see Figure 3.5). In this simplified model the theoretical arrival time t^{th} of the photon in an OM can be computed analytically:

$$t^{th} = t_0 + \frac{1}{c}\left(l - \frac{k}{\tan\theta_C}\right) + \frac{1}{c/n} \cdot \frac{k}{\sin\theta_C}, \tag{3.2}$$

where l and k are the components parallel and perpendicular to the muon track. Since the muon is relativistic at energies above the ANTARES threshold, it is assumed to propagate at the speed of light in vacuum c, whereas the photon travels at the speed of light reduced by the refraction index of the medium c/n. Other crucial parameters that are calculated from this model are the photon path length

$$b = \frac{k}{\sin\theta_C} \tag{3.3}$$

and the cosine of angle between the incident photon and the pointing direction of the OM a, which are used to predict the number of detected photons.

The key component of the reconstruction algorithm is Maximum Likelihood (ML) fits. The concept behind the ML fit is that for each possible track the probability of obtaining the detected set of hits can be computed. For a given track and a given PMT, labelled i, the probability of observing the event at given track parameters is:

$$P(event|track) = \prod_i P(t_i|t_i^{th}, a_i, b_i, A_i), \tag{3.4}$$

where t denotes the measured arrival time, t^{th} the expected arrival time according to the given track, and A is the hit amplitude.

This probability is referred to as the likelihood of the event, which is expressed in terms of a Probability Density Function (PDF). This function was developed by modelling the detector response for muon events. It comprises the time residual τ_i of hit i, which is the difference between the measured arrival time of a hit t_i^{hit} and the expected arrival time t_i^{th} according to the assumed muon track:

$$\tau_i = t_i^{hit} - t_i^{th}. \tag{3.5}$$

These time residuals of signal hits for different amplitude bins were parametrised to fit the distribution obtained from simulation (see Figure 3.6). They include contributions from scattered and direct photons originating from the muon itself and from secondary particles.

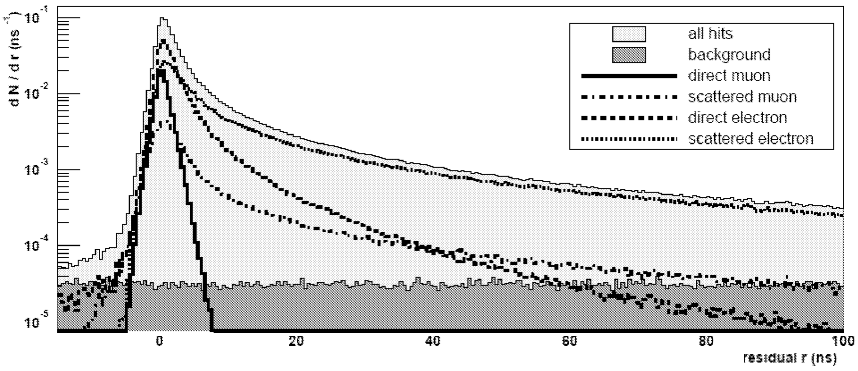

Figure 3.6: *Distribution of time residuals of photon arrival times relative to the direct muon signal (from [48]).*

Moreover, the PDF takes into account the expected number of signal hits N^{sig} of a given amplitude, which is estimated from the parameters a and b assuming they are independent:

$$N^{sig}(a, b) = N^{sig}(b) \cdot f(a). \tag{3.6}$$

$N^{sig}(b)$ denotes the expected number of signal hits taking into account the distance from the track, and the function $f(a)$ describes the angular acceptance of

the PMT, as shown in Figure 3.4 right. $N^{sig}(b)$ was parametrised to fit the simulations. The background hits, which are uniformly distributed in time during an event, are also included in the PDF. The total PDF is a weighted sum of the PDF for a signal hit $P^{sig}(t_i|t_i^{th})$ and the PDF for background hits $P^{bg}(t_i|t_i^{th})$:

$$P(t_i|t_i^{th}, a_i, b_i, A_i) = P^{sig}(t_i|t_i^{th})P_i(sig|a_i, b_i, A_i) + P^{bg}(t_i|t_i^{th})P_i(bg|a_i, b_i, A_i) \quad (3.7)$$

$P_i(sig)$ and $P_i(bg)$ are the probabilities that the hit is a signal or a background hit respectively.

However, it was found that the ML is very sensitive to the quality of the track estimate, which is used as starting point for the calculation of the track parameters. If this input track is too far from the true track parameters, the minimisation algorithm will converge on a local maximum in the PDF instead of finding the global maximum. The efficiency of finding the global maximum is related to the gradient of the likelihood function and the quality of the starting point. In order to ensure that the starting point is already as close as possible to the true track parameters, a chain of consecutive fitting procedures was combined with hit selection procedures to form a full reconstruction algorithm (see Figure 3.7).

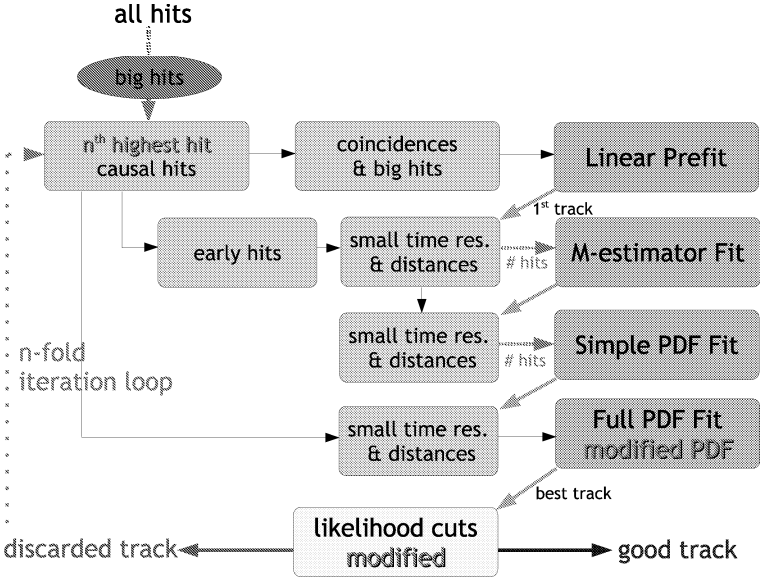

Figure 3.7: *Illustration of the reconstruction algorithm featuring hit selections (blue) and fit algorithms (green). The original* `AartStategy` *is displayed in black and the modifications are shown in pink.*

Prior to reconstruction, a simplified trigger is applied to the events, selecting only those events that have produced at least 6 hits in 5 different OMs, which is the minimum number of hits needed to calculate the 5 parameters defining a track $(\vec{r}, \theta, \phi)$. Moreover, to provide a sensible lever arm to fit the track, it is

necessary for the hits to be distributed in at least 2 different storeys on 2 different strings. This simplified trigger had been established before the ANTARES trigger software was completed and is still part of all reconstruction algorithms.

The first stage of reconstruction starts with the selection of hits. Only those hits are considered suitable for reconstruction which are causally related to each other. The hit with the highest amplitude is selected as the reference hit with which all other hits are causally correlated. In most cases, this hit is indeed a signal hit.

A linear prefit with constraint of the muon velocity is performed by analytically fitting a straight line through the hit positions. This prefit is performed on a subsample of hits, which are considered to be very likely signal hits and are therefore selected either as potential hits with amplitudes higher than 3 pe or hits occurring in coincidence, that is hits in the same storey within a time interval of 25 ns (the integration time of the ARS). The linear prefit provides the first track needed as the starting point for the successive ML fits.

The hits for the next fit are selected on the basis of the prefit track. Early hits are preferred since they are likely to originate from unscattered photons. From the sample of early hits, only those are selected as input for the next fit which have small time residuals and distances with respect to the prefit track. The M-estimator fit, which belongs to a special class of minimisation solutions, is performed on these hits and was selected for its robustness. The next stage is an ML fit using a simple PDF which is based solely on time residuals. The input hits are almost the same as for the M-estimator fit, except that they are selected because of having small time residuals and distances with respect to the track produced by the M-estimator.

Finally, an ML fit is carried out that uses the full PDF containing information on time residuals, amplitudes and expected photon numbers. To be unbiased, the hits for the final fit are selected from all causal hits to show small time residuals and distances with respect to the last fitted track, which serves as a starting point. However, the time window for small residuals is set to 250 ns, which is much larger than in the previous hit selection. Since the PDF also takes the noise hits into consideration, this larger window allows us to use a larger sample of hits without compromising the reconstruction quality. Finally, cuts on the likelihood are performed to reject poorly reconstructed muon tracks.

The original `AartStrategy` was used to study the effects of high optical background noise: the 60 kHz noise rate – for which the strategy is optimised – was taken as a reference for comparison with the results at 120 kHz and 240 kHz. The effects on the pointing accuracy of the reconstructed track and the expected muon-neutrino rates in the detector are shown in Figure 3.8 and 3.9 respectively.

In general, the higher the background noise, the more tracks can be reconstructed

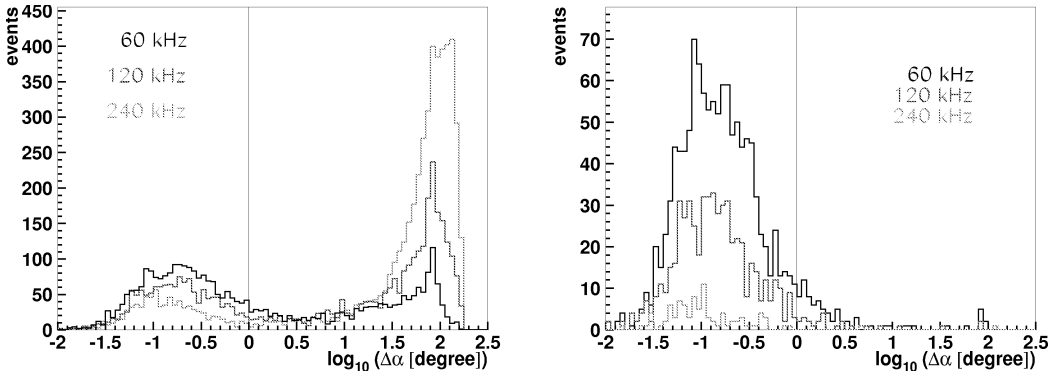

Figure 3.8: *Pointing accuracy of reconstructed neutrino events using the original* `AartStrategy` *at different baseline rates before (left) and after (right) quality cuts. The vertical line indicates a resolution of 1°.*

at the expense of quality. Since the fit algorithms require a minimum number of input hits, this condition is likely to be satisfied if plenty of noise hits are present. (Especially at low energies, where the muon produces only a limited amount of signal hits, noise hits can slip through the hit selection criteria and provide the missing hits needed to fulfil the minimum hit number. However, the fit algorithms are misguided by these noise hits and cannot converge on the true muon track. This leads to a large number of falsely reconstructed events with huge angular deviations (see Figure 3.8 left). The quality cuts applied by the `AartStrategy` reject these fake tracks very rigorously at the expense of signal events (see Figure 3.8 right and 3.9). The surviving events correspond to only 70% (20%) of the total number of well-reconstructed events at 60 kHz. The problem of this tremendous loss in reconstruction efficiency has to be tackled in such a way that it is unnecessary to compromise in pointing accuracy and reconstruction purity.

The modified strategy for high background noise

While the original `AartStrategy` is explicitly optimised to perform well at a background rate of 60 kHz, it is not suited for higher background rates without modifications. The most obvious alteration concerns the adjustment of the background rate in the PDF to ensure that the noise hits are likely to be recognised as such and not treated as signal hits. Furthermore, the selection procedure for causal hits has been modified. Since only causal hits are used in all fitting algorithms, the selection process must be examined carefully. In the original version

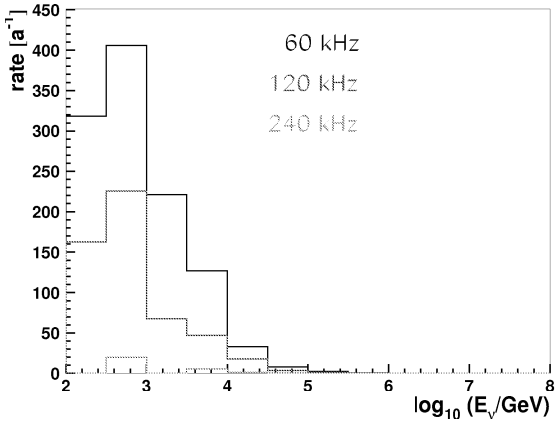

Figure 3.9: *Expected rates of atmospheric neutrinos at different baseline rates using the original* `AartStrategy`.

the causality filter takes the hit with the highest amplitude as the reference hit to which all other hits are put into a causal relationship. If the causal relationship is viable, these hits are selected and the entity of these hits forms the sub-sample of causal hits. All the others are rejected and no longer used as input for any fits. It was found that at 60 kHz this kind of causality filter is quite viable since the highest hit is likely to be a signal hit. However, at higher noise rates the probability that the highest hit is a background hit increases, in which case the whole sample of causal hits is invalidated and the fitting algorithms are completely thwarted. If this happens and the fitted track is rejected by the quality cuts, the causality filter is reactivated and a new sample of causal hits is selected in accordance with a new reference hit, which shows the second-highest amplitude. The reconstruction procedure is repeated with the new sample of causal hits. It has been determined that, in general, one out of five hits which have the highest amplitude is very likely to be a signal hit. This means that, at most, five iterations of the reconstruction procedure suffice to reconstruct a decent track based mainly on signal hits. However, selecting the right reference hit does not imply that the whole sample of causal hits also consists of signal hits. The higher the background rate, the more noise hits emerge which meet the causality condition.

Therefore, an amplitude cut was applied before the causality filter. Hits with an amplitude below a given threshold, which depends on the actual noise rate, are rejected altogether at the start of reconstruction. This remedial action disposes of a vast number of noise hits while retaining the majority of signal hits. The optimal threshold amplitude which gives the highest efficiency of well-reconstructed events was determined by studying samples of events with varying amplitude cuts at different noise rates. The 60 kHz sample with no amplitude cut was used as

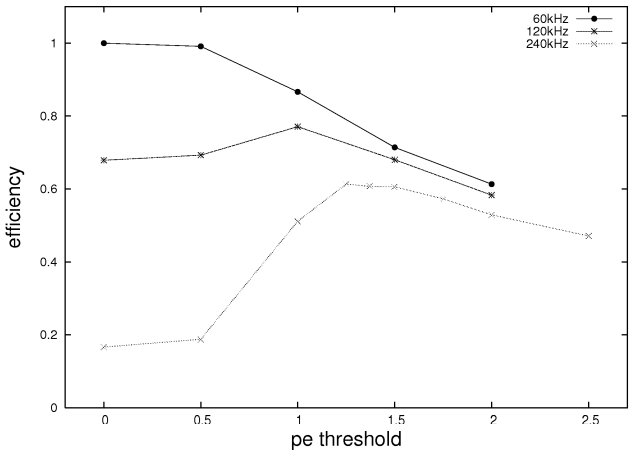

Figure 3.10: *Efficiency of well-reconstructed tracks as a function of the threshold amplitude of the hits used. Different noise rates have different optimum threshold amplitudes.*

a reference for establishing the relative efficiency. As can be seen in Figure 3.10, the 120 and 240 kHz samples display efficiency losses when no amplitude cut is applied. This effect is most evident at 240 kHz, when the efficiency falls below 20%. However, the efficiency can be recovered significantly if amplitude cuts are placed at 1 pe (1.25 pe) for the 120 kHz (240 kHz) samples. The implementation of this action is also the cause of the drop in total reconstructed events in Figure 3.11 left, as compared to Figure 3.8 left. Since many hits, especially noise hits, are missing, the minimum hit number criteria are no longer easily met, which in the former case leads to an enormous increase in fake muon tracks.

The amplitude cut is very striking but in some cases, especially where low energy muons are concerned, the number of remaining hits is reduced to such an extent that the minimum hit number condition needed for some fitting algorithms is no longer satisfied. Therefore, the minimum hit numbers for the "M-estimator fit" and "simple PDF fit" have been reduced to the lowest possible minimum required by the fit strategy.

The modifications presented above all aimed at increasing the reconstruction efficiency especially at high background rates (compare Figure 3.12 to Figure 3.9). However, a gain in efficiency is often accompanied by purity losses, as was also the case in this study. An easing of conditions in the reconstruction algorithm leads to a higher number of falsely reconstructed events, which cannot be singled out and removed by the usual quality cuts. This is especially critical if down-going events are reconstructed as up-going events because the usual means of discriminating atmospheric muons is a cut on the zenith angle. If this measure fails to hold, atmospheric muons, which are much more abundant than neutrinos,

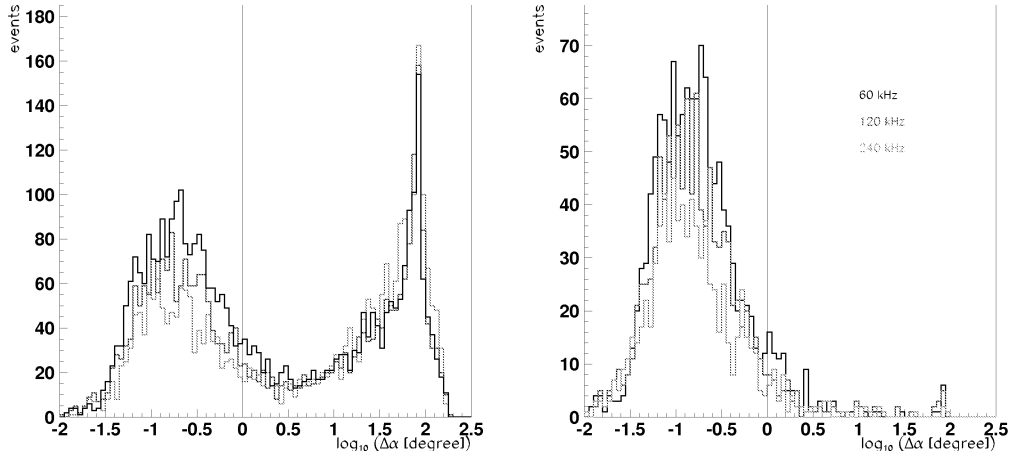

Figure 3.11: *Pointing accuracy of reconstructed neutrino events using the modified strategy for high background noise at different baseline rates before (left) and after (right) quality cuts. The vertical line indicates a resolution of 1°.*

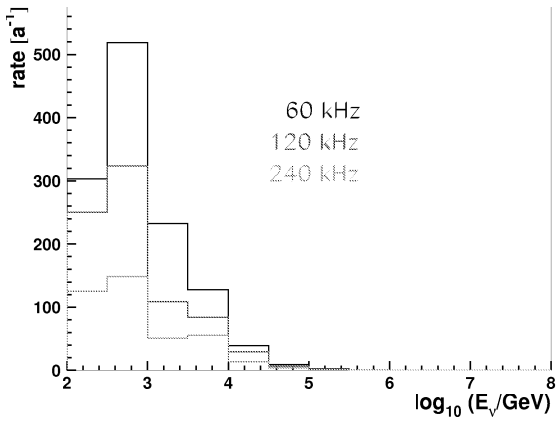

Figure 3.12: *Expected rates of atmospheric neutrinos at different baseline rates using the modified strategy for high background noise.*

are falsely identified as neutrinos, thus spoiling the results of an observation.

In order to restore the purity of the reconstruction algorithm, a study on atmospheric muons was carried out. First, the reconstruction algorithm – in the state after augmenting the efficiency to the maximum – was used to reconstruct a large sample of atmospheric muons and thereby assess the extent of contamination by atmospheric muons. The sample of atmospheric muons used in this analysis was

previously produced by simulating the interaction of cosmic ray nuclei in the atmosphere (see [38] and section 3.1 for more details). The number of muons originating in these hadronic interactions is large and, in spite of being shielded by 2400 m of water, muon bundles with multiplicities of up to several hundred still reach the detector. Since the reconstruction algorithm is designed for single muons it is not impossible – although extremely rare – for an atmospheric muon to be reconstructed as an upward-going muon.

Table 3.1: *Expected rates per day in ANTARES for atmospheric muons and neutrinos for different baseline rates and reconstruction algorithms: a – maximum efficiency; b – maximum efficiency and purity; c – original* `AartStrategy`

baseline	down-recon. atm. μ	up-recon. atm. μ	atm. ν	WB-bound ν
60 kHz	23220^c	9.2		
	38598^a	18.7		
	29313^b	3.4	12.7	0.019
120 kHz	19494^a	72.6		
	12114^b	2.2	6.6	0.014
240 kHz	7681^a	46.7		
	3964^b	2.7	2.8	0.0097

Applying the reconstruction algorithm modified for maximum efficiency to both atmospheric muons and neutrinos alike leads to higher rates of muons compared to neutrinos (see Table 3.1). However, from the astrophysical point of view it is desirable to keep the rate of atmospheric muons below the rate of neutrinos. This can be achieved by tuning the cuts on the likelihood to make them less prone to falsely reconstructed events. The limit on the likelihood cut is reached when the atmospheric neutrinos outnumber the muons. Since atmospheric neutrinos represent an intrinsically irreducible background to any astrophysical observation, there is no reason to go much below their rate. Naturally, at higher background rates the likelihood cut has to be more stringent to avoid contamination due to noise hits. The final results obtained by using the above-mentioned cuts are presented in Table 3.1 and also in Figure 3.13 to illustrate the energy dependence of the rates. Two different curves are shown for the atmospheric neutrinos representing the maximum rate to be expected from horizontal neutrinos and the minimum rate from vertical neutrinos.

In conclusion, it must be pointed out that the dependence of the event rates in ANTARES from the baseline rates is different for signal and background events. Since varying baseline rates primarily cause a drop in efficiency, which is a function of energy, atmospheric muons and neutrinos featuring softer spectra ($E^{-2.7}$)

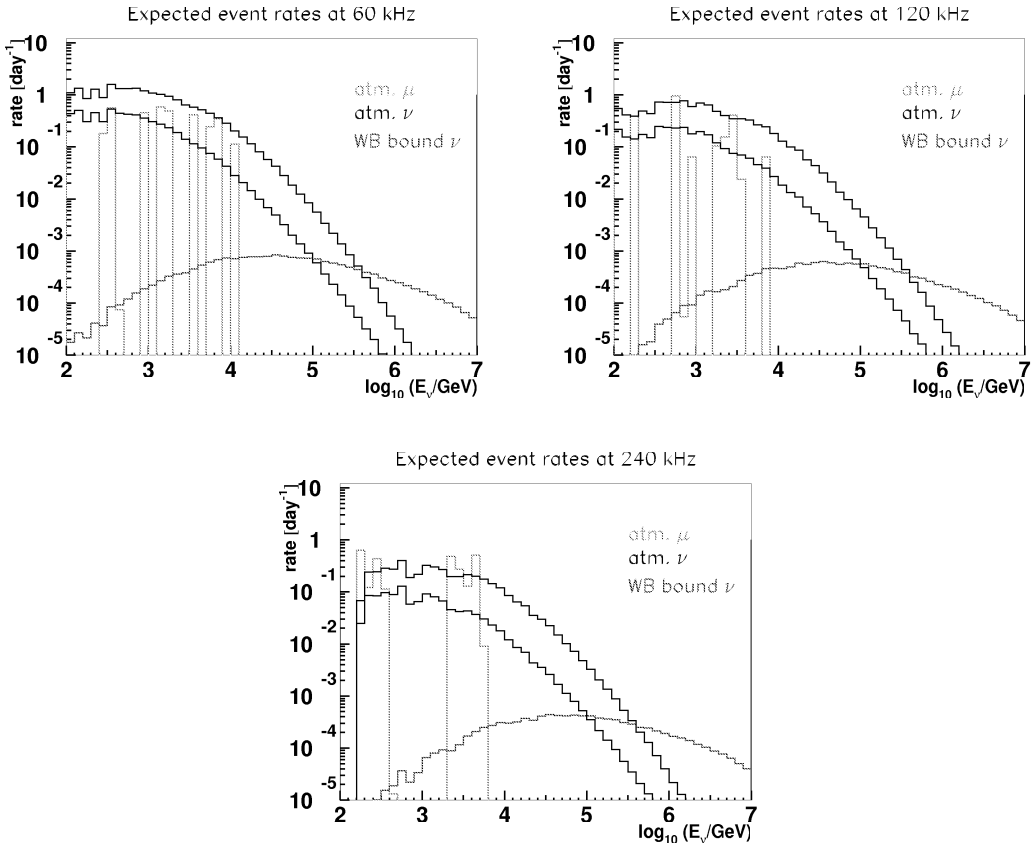

Figure 3.13: *Expected signal and background event rates in ANTARES for baseline rates of 60, 120 and 240 kHz.*

than the expected signal neutrinos (E^{-2}) will suffer more from the efficiency loss than the signal neutrinos. As can be seen in Table 3.1, the rate of neutrinos corresponding to the Waxman-Bahcall bound decreases from 100% at 60 kHz to 75% at 120 kHz and 50% at 240 kHz, whereas the rates of atmospheric neutrinos fall much more dramatically to 50% at 120 kHz and 22% at 240 kHz. Thus, this is good news for all neutrino sources with spectra that are not too soft.

Effects of bioluminescence bursts on the reconstruction

In the following, the results of the bioluminescence burst study are presented in terms of their impact on the reconstruction efficiency. Due to their nature, bioluminescence bursts can be easily identified on the basis of their duration, which is usually on a scale of seconds and therefore cannot, for instance, be

mistaken for Cherenkov light from a hadronic shower. In the end, optical modules affected by bursts will be eliminated from the reconstruction process.

In the present study a software burst filter was applied to simulate the loss resulting from OMs affected by bursts. In the beginning, it was assumed that a burst rate of 10% corresponds to 10% of the optical modules being randomly deactivated and thus eliminated from the reconstruction procedure. A more precise modelling of bioluminescence bursts takes into account the fact that the bursts are not distributed completely statistically among the optical modules but seem to affect all the OMs located on the same storey. Therefore, in a second version of the burst filter these correlations between neighbouring OMs were implemented. However, the relative difference from the uncorrelated version of bursts proved to be negligible for burst rates below 20%. In the case of a 40% burst rate the maximum observed discrepancy in the results amounted to a 5% effect.

In general, bursts cause a decline in reconstruction efficiency due to the lack of signal hits. If the rate of missing hits is low compared to the total number of hits induced by a neutrino signal, the reconstruction algorithm can compensate for the loss with virtually no adverse effect on the overall efficiency and purity of the reconstructed track. This is the case when either the burst rate is low (e.g. below 20%) or sufficient hits have been generated, which is a characteristic feature of high-energy events. The results are shown in Figure 3.14 for different baseline and burst rates in combination, expressed in terms of effective detector volume. A gradual reduction in effective volume is observable towards low neutrino energies. As a rule, the decrease in efficiency is greater the higher the baseline and burst rate are. A significant drop in effective volume occurs at a baseline rate of 240 kHz in combination with a burst rate of 40%. Since the two phenomena are interconnected and both effects lead to a loss of signal hits, the limit seems to be exceeded below which it would be possible to compensate for missing hits.

3.3 Effective detector volume and area

For the evaluation of relative effects resulting from particular changes at different stages of reconstruction it is often helpful to present the results as ratios of event rates or changes in the angular resolution. However, if a quantitative measure is emphasised to present the predictions concerning the performance of the ANTARES detector, effective volume and effective areas for neutrinos and muons are the preferred means.

The effective volume of ANTARES is defined as the volume of a 100% efficient detector for observing neutrinos which interact within that volume. To calculate the effective volume V_{eff}, the generation volume V_{gen} has to be multiplied by the

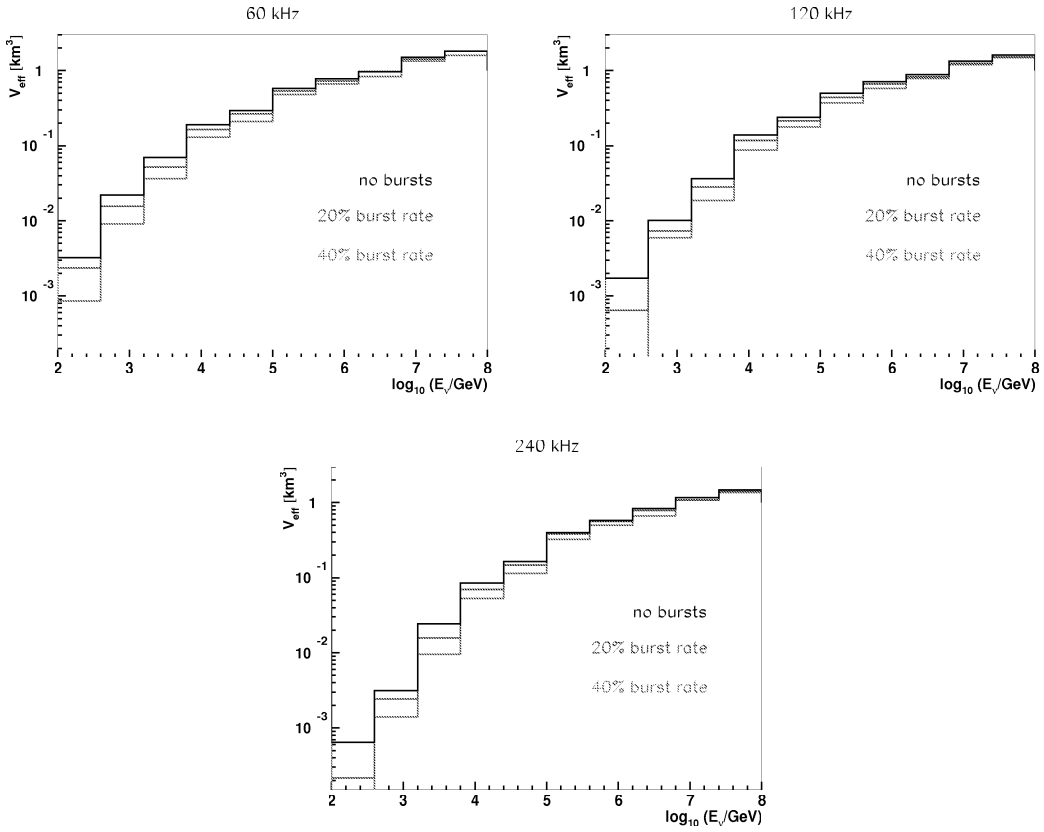

Figure 3.14: *Effective detector volume corresponding to baseline rates of 60, 120 and 240 kHz. The burst rates are indicated in the figures.*

ratio of selected events after reconstruction N_{sel} to the total number of generated events N_{gen} (in the same energy and angular bins):

$$V_{eff}(E_\nu, \theta_\nu) = \frac{N_{sel}(E_\nu, \theta_\nu)}{N_{gen}(E_\nu, \theta_\nu)} \cdot V_{gen}. \tag{3.8}$$

Given the effective volume, the rate of neutrino interactions can be calculated for a given theoretical flux model Φ_ν based on the neutrino interaction cross-section $\sigma(E_\nu)$, its transmission probability through the Earth $P_E(E_\nu, \theta_\nu)$ and using the knowledge of the target nucleon density ρN_A:

$$\dot{N}_\nu(E_\nu) = \int V_{eff}(E_\nu, \theta_\nu) \cdot \sigma(E_\nu) \rho N_A \cdot P_E(E_\nu, \theta_\nu) \cdot \Phi(E_\nu, \theta_\nu, \varphi_\nu) dE_\nu d\Omega_\nu. \tag{3.9}$$

However, for astrophysical calculations it is more convenient to use the effective neutrino area of a telescope to be able to compute the expected event rates directly. Thus the effective area of a neutrino detector is defined by the relation

$$\dot{N}_\nu(E_\nu) = \int A_{eff}(E_\nu, \theta_\nu) \cdot \Phi(E_\nu, \theta_\nu, \varphi_\nu) dE_\nu d\Omega_\nu. \tag{3.10}$$

This quantity is indeed an effective area corresponding to neutrino fluxes arriving at the detector:

$$A_{eff}(E_\nu, \theta_\nu) = V_{eff}(E_\nu, \theta_\nu) \cdot \sigma(E_\nu) \rho N_A \cdot P_E(E_\nu, \theta_\nu). \tag{3.11}$$

In Figure 3.15 the effective area for upward-going and downward-going neutrino fluxes arriving at the surface of the Earth is presented. The black curve shows the area for an isotropic flux of upward-going neutrinos. Three zenith angle ranges of $0° - 30°$, $30° - 60°$ and $60° - 90°$ are resolved to demonstrate the effect of absorption within the Earth, which is most pronounced at vertical directions and becomes dominant in the PeV energy region. In the low-energy region however, the detector seems to be more efficient for neutrinos arriving closer to the vertical since the detector volume is comparatively longer at these angles and thus provides a greater length for observing muon tracks.

The detector is less efficient for downward-going neutrino fluxes due to the fact that it was designed to see mainly upward-going neutrinos and hence the OMs are looking 45° downwards. Since this kind of observation mode is only interesting at energies well in the TeV region, where atmospheric neutrinos are virtually nonexistent and therefore cannot be confused with cosmic neutrinos, only the high-energy behaviour of the effective area for downward-going neutrinos is important. Since no absorption in the Earth occurs, the effective area for downward-going neutrinos is perfectly competitive with the area for upward-going neutrinos above 100 TeV.

The effects of different baseline rates have also been illustrated by their corresponding effective areas (see Figure 3.15 lower). The effective areas presented here correspond to the effective volumes in Figure 3.14 with burst rates set to zero. The loss in effective area resulting from increasing baseline rates is most pronounced at low energies, where noise hits generally outnumber signal hits, which hampers the reconstruction.

Another way of displaying the ANTARES detector performance is the effective area for muons. Like the effective area for neutrinos, it can be considered as the area of an equivalent "flat" detector and thus can be used to compute the number of detected muons at a given differential muon flux. The effective area for muons is calculated by dividing the effective volume $V_{eff}(E_\nu)$ by the effective muon range $\langle R_{eff}(E_\nu) \rangle$:

$$A^{\mu}_{eff}(E_\nu) = \frac{V_{eff}(E_\nu)}{\langle R_{eff}(E_\nu) \rangle} = \frac{N_{sel}(E_\nu)}{N_{gen}(E_\nu)} \cdot \frac{V_{gen}}{\langle R_{eff}(E_\nu) \rangle}. \tag{3.12}$$

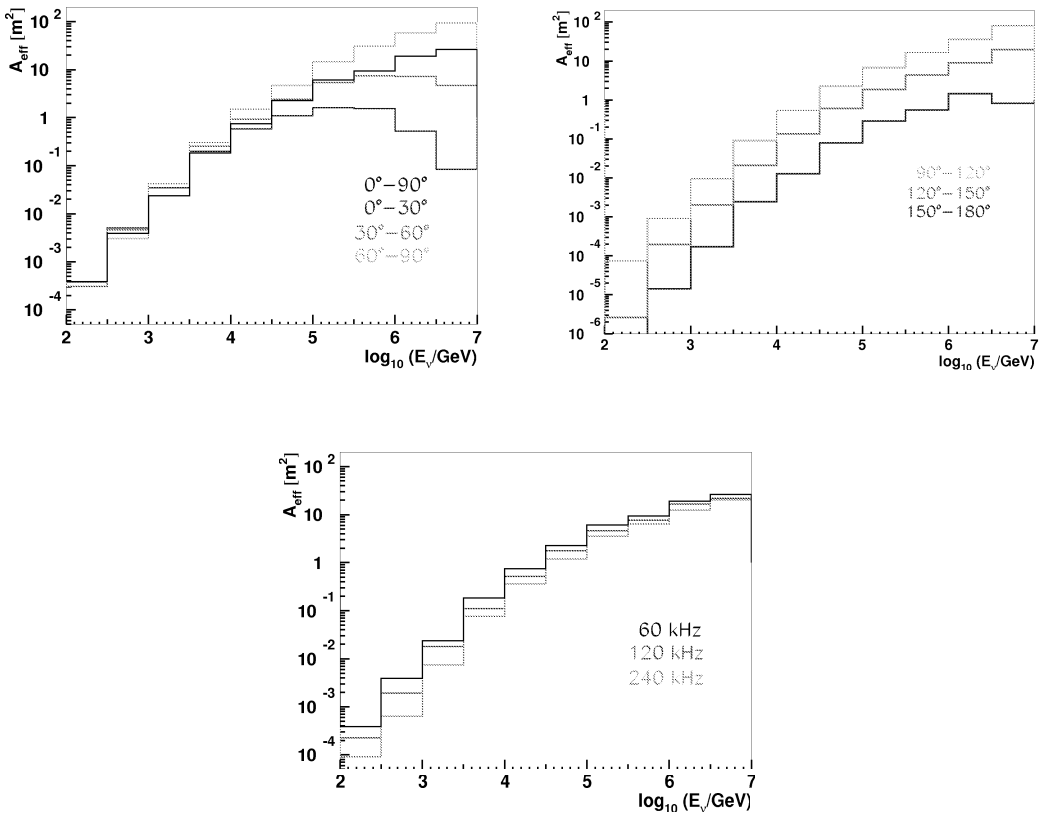

Figure 3.15: *Effective muon neutrino area of ANTARES obtained when using the modified reconstruction strategy for high optical background. Upper: Effective areas for different neutrino zenith angles at 60 kHz background rate. Lower: Effective areas for varying baseline levels and zenith angles between 0°-90°.*

3.4 Angular resolution and point-spread function

Knowing the pointing accuracy of the telescope, in other words the precision with which neutrinos from a point-like source are reconstructed in terms of direction, is equally important for astrophysical studies. The angular resolution is an important quantity in the search for neutrinos, especially those from point sources. A higher angular resolution leads to smaller search bins, thus lowering the background rate per bin and thereby increasing the signal-to-noise ratio. The angular resolution is defined here as the median of the distribution of angles between the original neutrino and the reconstructed track.

Figure 3.17 shows the angular resolution of ANTARES for neutrinos as a function of the neutrino energy and its dependency upon the muon angular resolution,

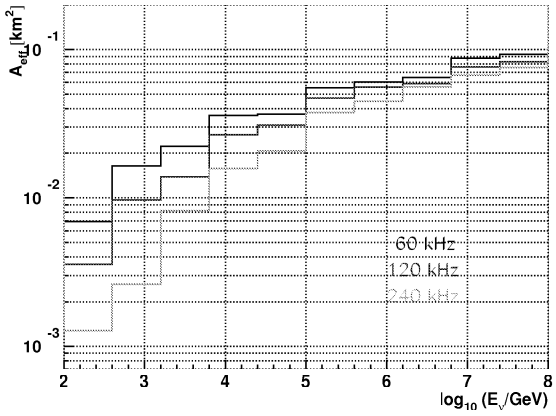

Figure 3.16: *Effective detector area for muons.*

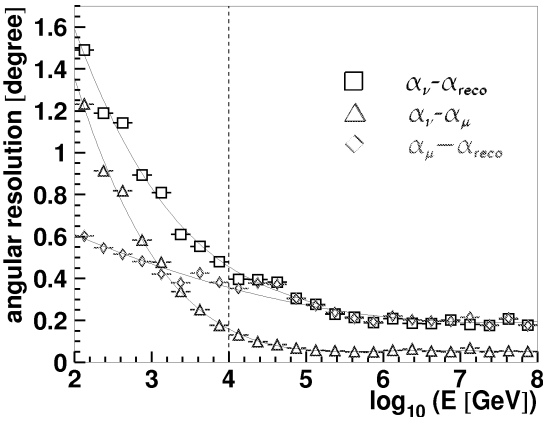

Figure 3.17: *Angular resolution as a function of neutrino energy.*

which is the actual resolution of the detector, and the angular deviation between incident neutrino and resulting muon. The upper curve (black squares) showing the neutrino angular resolution is the important parameter for astrophysical studies, whereas the lower curve (red rhombi) corresponding to the muon resolution states the reconstruction accuracy of the telescope. At low energies, the discrepancy between the resolution of the detector for neutrinos and the resolution for muons is especially pronounced because the incident neutrino and the generated muon do not have the same direction in the first place. The angular deviation between neutrino and muon is illustrated by the blue triangles. As the neutrino

energy increases, the muon will experience a stronger Lorentz-boost and its direction will be aligned more precisely with the neutrino direction. The vertical line at 10 TeV indicates the energy above which the resolution of the detector for neutrinos coincides with the resolution for muons and is limited only by the reconstruction procedure and the underlying finite time and spatial resolution of the detector.

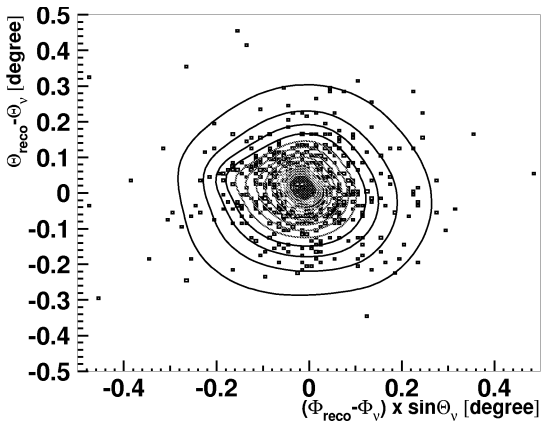

Figure 3.18: *Point-spread function in detector coordinates.*

Figure 3.18 illustrates the point-spread function of the ANTARES telescope. This is another way – adopted from the astronomers – of characterising the reconstruction resolution in terms of the width of the angular deviation expressed in spherical detector coordinates θ and ϕ, so that all bins span equal solid angles.

3.5 Impact of systematic uncertainties on efficiency and resolution

Data analysis is always subject to systematic uncertainties, whose origin is both theoretical and experimental. Since complex detectors like ANTARES rely on Monte Carlo studies to establish high-efficiency and good-quality reconstruction algorithms, theoretical uncertainties with regard to the underlying physical models similarly affect the results of data analysis, as do experimental uncertainties due to imperfect knowledge of the detector components and the instrumented target medium.

Theoretical uncertainties affect the primary cosmic ray flux, composition and energy spectrum and also the physical interaction models implemented in the

simulation programmes used for the analysis. This translates into an uncertainty of about 20% in the flux of atmospheric neutrinos and muons in the relevant energy region (see chapter 1.1). Besides, the muon bundle multiplicity is also known to have been underestimated by the `CORSIKA` programme when compared to experimental results.

Experimental uncertainties are related to the detector response, which depends on the precise knowledge of each component, including the detector medium itself. Although water is a homogeneous medium, the scattering and absorption length at the ANTARES site can be affected by seasonal variations in the degree of pollution. Similarly, the optical noise rate is subject to temporal variations, which are taken into account in the modified reconstruction strategy, but also to spatial variations – besides bioluminescence bursts – in such a way that OMs at the top of a detector line can be affected by higher noise levels than OMs a the bottom. Most important for the determination of angular resolution and effective area – which are essential for absolute flux measurements – are the timing and position information from the OMs. While the transit time spread of the OMs and light scattering are already included in the simulations used, the position and orientation of the OMs are usually assumed to be known beyond doubt.

The study dedicated to fathoming the impact of systematic uncertainties therefore focuses on alignment issues, which can be a major source of systematic errors in ANTARES. Line alignment depends on hydrophone position information obtained by triangulation to acoustic beacons on the sea floor. If the accuracy of the hydrophone position is assumed to be 10 cm instead of perfect, this will have an effect on the accuracy of track reconstruction. Simulations have been performed using different detectors for reconstruction: the perfectly aligned detector, a detector whose lines have been distorted corresponding to a sea current of 10 cm/s, and the same distorted detector whose line shape has been reconstructed with the aid of hydrophones and tiltmeters, thereby assuming an error on the hydrophones' position of 5 cm and on the tiltmeters of 1° [36]. The impact of the misaligned detectors on the angular resolution is shown in Figure 3.19.

Clearly, the angular resolution of the non-aligned detector is deteriorated as compared to the perfectly aligned detector. However, the angular resolution of the distorted detector, whose line shape has been reconstructed on the basis of realistic errors on the hydrophones and tiltmeters, is comparable to the angular resolution of the perfectly aligned detector.

Another study has been carried out to assess the importance of TCM2 cards on each storey, which house the compasses needed to determine the heading of each storey. The heading information is very important for track reconstruction because it indicates the orientation of OM0 with respect to north. Without the knowledge of the orientation of the OMs, the likelihood function in the reconstruction algorithm, which assumes a certain hit probability depending on the

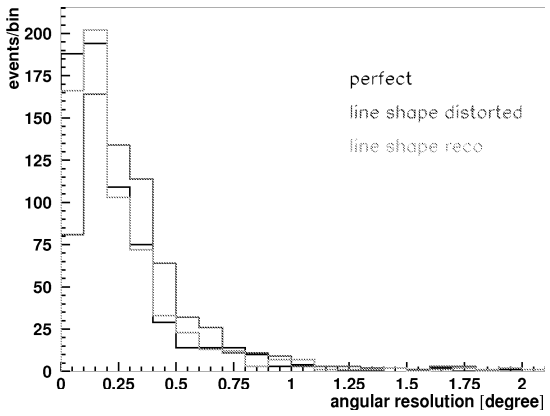

Figure 3.19: *Angular resolution depending on the detector alignment.*

relative photon angle with respect to the OM, cannot yield good results. Therefore, unknown headings represent a source of systematic errors which need to be investigated.

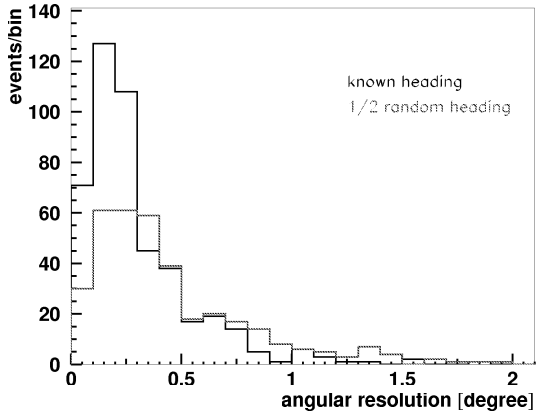

Figure 3.20: *Angular resolution depending on the heading knowledge.*

A new simulation generating a sample of neutrinos with an E^{-2}-spectrum in the energy range between $10^2 - 10^6$ GeV has been performed. The simulation was performed using a detector with random headings. For reconstruction a different detector was used. In this case every second heading was identical to the headings of the detector used for simulation, and the headings in between were

rotated randomly [36]. This corresponds to a situation in which compass cards are omitted on every second storey, an omission which could become necessary due to economic constraints, and interpolation from neighbouring floors is not possible due to the uncorrelated movement of the optical module frames in general – with the possible exception of very strong sea currents. The results are shown in Figure 3.20. The overall angular resolution clearly deteriorates by almost a factor of two and, moreover, there is a loss in efficiency of about 30%. It is conceivable that a reconstruction strategy with a likelihood function adjusted to this special situation may alleviate the effects of efficiency loss. However, there seems to be justification for integrating a compass on each storey provided the funding is available.

4 Line 1 data analysis

The ANTARES collaboration has taken a major step forward with the deployment and operation of the first complete detector line – Line 1. Prior to the successful operation of Line 1 several test lines had been deployed and operated (a "demonstrator line" in 1999/2000, the Mini Instrumentation Line (MIL) and Prototype Sector Line (PSL) in 2003, and the MILOM since 2005), which proved the validity of various design aspects in situ but in some cases also indicated certain problems concerning the loss of optical transmission and leaks in the cables and containers. From the experiences with these prototype lines lessons were learnt, which accounted for the successful operation of Line 1.

4.1 Principles of muon-track reconstruction with one line

The offline physics data analysis of Line 1 is performed within the framework of a software package consisting of the modules `Calibrate`, `Real` and `Physics` [49]. It is preceded by the Datafilter, which triggers and filters the raw data online and stores it in the form of "Physics Event" and "Summary Timeslices" on disk.

The `Calibrate` package is used to calibrate the raw data by accessing the relevant ARS calibration information stored in the database. Moreover, the calibration is intended to be extended to include the position and orientation of the OMs once the detector has been aligned. While the ARS calibration values are constant, the position and heading information for each OM is expected to change every 3 minutes, which corresponds to the read-out interval of the tiltmeter, compass and hydrophone data. This high sampling frequency is essential to keep trace of the varying detector geometries as the line, and with it the OMs, move in the sea current. Thus the `Calibrate` software has to deal with varying detector geometries during a run as alignment data are supposed to change accordingly. A precise calibration of the raw data is unavoidable in order to prevent systematic errors caused by misaligned OMs and other offsets in the ARS. The main output of `Calibrate` is the "Full Event" containing all the calibrated hits.

The `Real` package contains the actual reconstruction algorithm which reads the information from the `Calibrate` output file, consisting of calibrated hits (position, time and amplitude), and performs the muon track reconstruction, thereby supplementing the "Full Event" with the fit information. Finally, the `Physics` package provides some examples of how the fit and possibly Monte Carlo information can be extracted from the `Real` output file and stored in histograms. The `Calibrate`, `Real` and `Physics` processing chains are capable of processing both real and Monte Carlo data, provided the MC data comes in the right format containing "Physics Event" and "Summary Timeslices".

Within the framework of the `Real` software package the reconstruction algorithm was modified to test the applicability of different algorithms to real data. The reconstruction algorithms tested involved different hit selections and χ^2-minimisation procedures. Starting from the triggered hits, those hits were selected first that produced the highest amplitudes. In a further attempt [50], hits were selected which lay within a cylinder of 120 m radius around the probed track and all the other hits were ignored. However, as these hit selections did not render the desired result in terms of a more accurate reconstruction of the zenith angle and smaller hit-time residuals, and, furthermore, proved to be quite time-consuming, they were abandoned in favour of all triggered hits together.

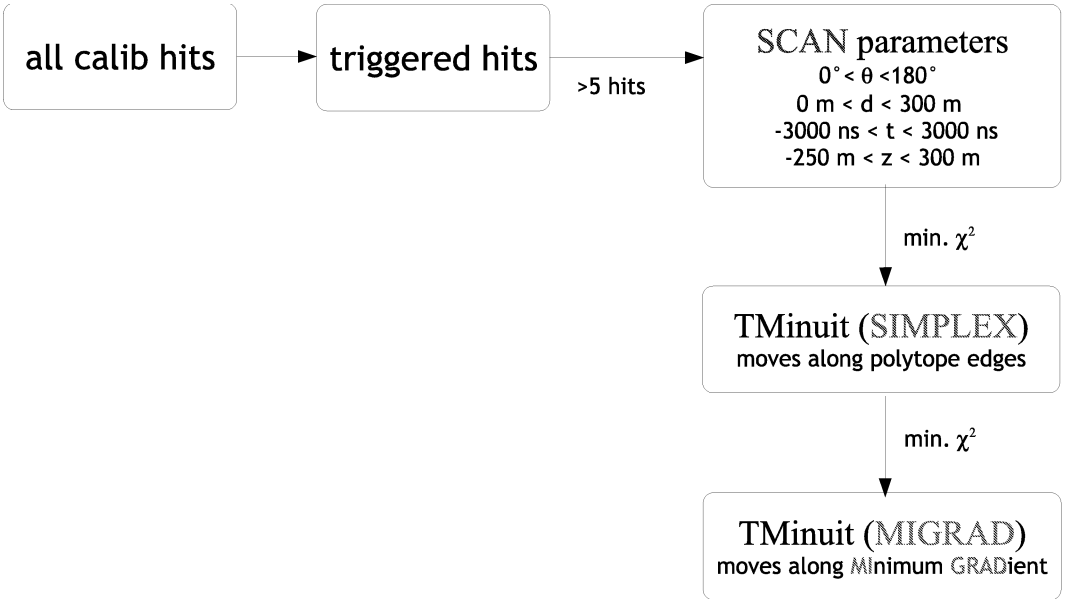

Figure 4.1: *Illustration of the reconstruction algorithm used for Line 1 data.*

Whereas in the previous reconstruction strategies the muon track was defined by the interaction vertex and direction of the muon (x, y, z, θ, ϕ), the `Real` strategy uses a different reference frame with a new set of parameters to characterise the

track consisting of the zenith angle θ, the shortest distance between the track and the line (assumed to be straight) d, the interaction time t_0, and the altitude z_0 at the closest approach of the muon to the detector line. These variables have been chosen because they are better suited for the simple geometry of one line, which is essentially azimuth-symmetric and thus yields poor results on the azimuth angle of the muon. By contrast, in the new reference frame the muon track can be described adequately by a simple hyperbolic equation between hit times t_i and altitudes z_i:

$$c(t_i - t_0) = (z_i - z_0)\cos\theta + \tan\theta_{Ch}\sqrt{d^2 + (z_i - z_0)^2\sin^2\theta}. \tag{4.1}$$

The reconstruction algorithm for Line 1 data used in this work (see Fig. 4.1) starts by reading in all triggered hits but, instead of using a pre-fit on the basis of the time-altitude hyperbola equation, in which the zenith angle is derived from one of the hyperbola's asymptotes, a scan is carried out on the four relevant parameters: the zenith angle θ, the distance between the track and the line d, the interaction time t, and the altitude z. However, instead of sampling the complete parameter space, the scanning is restricted to a certain interval for each parameter, which is physically motivated and does not cut away useful parts of the parameter space. While the zenith angle is naturally constrained to be between 0 and 180 degrees, the other parameters are not a priori restricted. Nevertheless, it seems justifiable to assume that the minimal distance between the muon track and the detector line should be less than 300 m, given the attenuation length at the site (46 m). In addition, the time of the closest approach of a muon t_0 has been limited to $\pm$3000 ns, which is still well above the typical duration of the maximum time period between causally related hits of 2200 ns. Similarly, the altitude of closest approach z_0 is restricted to the interval $[-250\ m; +300\ m]$, where the centre of the line is set to 0.

The introduction of predefined intervals on the parameter space, which is physically motivated, provides guidance for the scanning and prevents the minimisation algorithms from running into minima which are very unlikely. The scan of the parameter space, as well as all the subsequent minimisation procedures, involve a chi-square minimisation of the time residuals on the triggered hits

$$\chi^2 = \sum_{i=1}^{nhit} \frac{(t_i - t_i^{th})^2}{\sigma^2}, \tag{4.2}$$

where t_i is the calibrated hit time in OM_i and t_i^{th} is the calculated time depending on the other parameters. The minimisation algorithms used involve the SIMPLEX and MIGRAD algorithms, which are numerical methods for optimising multi-dimensional unconstrained problems. The SIMPLEX method uses the concept of a simplex, which is a polytope of $N + 1$ vertices in N dimensions. A series of linear inequalities defines a polytope as a feasible region. The simplex

algorithm begins at a starting vertex and moves along the edges of the polytope until it reaches the vertex of the optimum solution.

However, as the simplex algorithm does not always converge to the absolute minimum, a second minimisation technique, MIGRAD, is applied, which uses an approximation to the gradient vector at the current best point. In practice, MIGRAD usually yields good estimates of the minimum, but it also has the disadvantage of not being absolutely reliable. The consecutive implementation of both minimisation algorithms appears to be useful as they apply different techniques, but a further repetition of both – as is implemented in the original `Real` strategy – does not seem to be more advantageous because the additional improvement is small (see also Fig. 4.3) in comparison to the increase in computing time.

4.2 Monte Carlo studies for Line 1

In contrast to the complete ANTARES detector, muon-track reconstruction with a single detector line is very challenging due to the limited efficiency and poor angular resolution, the latter being mostly the result of azimuth symmetry and geometric ambiguity. Therefore, the muons reconstructed with Line 1 will most probably be atmospheric muons because they are much more abundant than atmospheric neutrinos.

The Monte Carlo simulations used for the Line 1 analysis consist of atmospheric muons generated by the `CORSIKA` programme in interactions of primary cosmic protons with nuclei in the atmosphere (see also chapter 3.1 for further details). The muons were propagated further from the sea level to the can level using the `MUSIC` code, from which they were tracked through the detector, thereby generating hits in the OMs with the `KM3` programme. The two detectors used for input were distorted in shape in accordance with sea currents of 7.5 cm/s and 23 cm/s. At this stage the Monte Carlo files were converted from ASCII to ROOT format by the `MonteCarloEventWriter` code. In addition, background noise could be added from a real data file (here: 022924), provided the latter has been previously processed by the `SummaryTimeSliceWriter` programme, which extracts the time slice summaries from raw data and simulates the background for a given detector geometry. Finally, the `TriggerEfficiency` programme triggers on hits and generates the "Physics Event" tree – similar to the "Physics Event" written by the `Datafilter`, which is used on real raw data. Thenceforward, both Monte Carlo and ANTARES data files can be processed by the same offline analysis programme package described above, consisting of `Calibrate`, and the modified `Real` and `Physics` programmes.

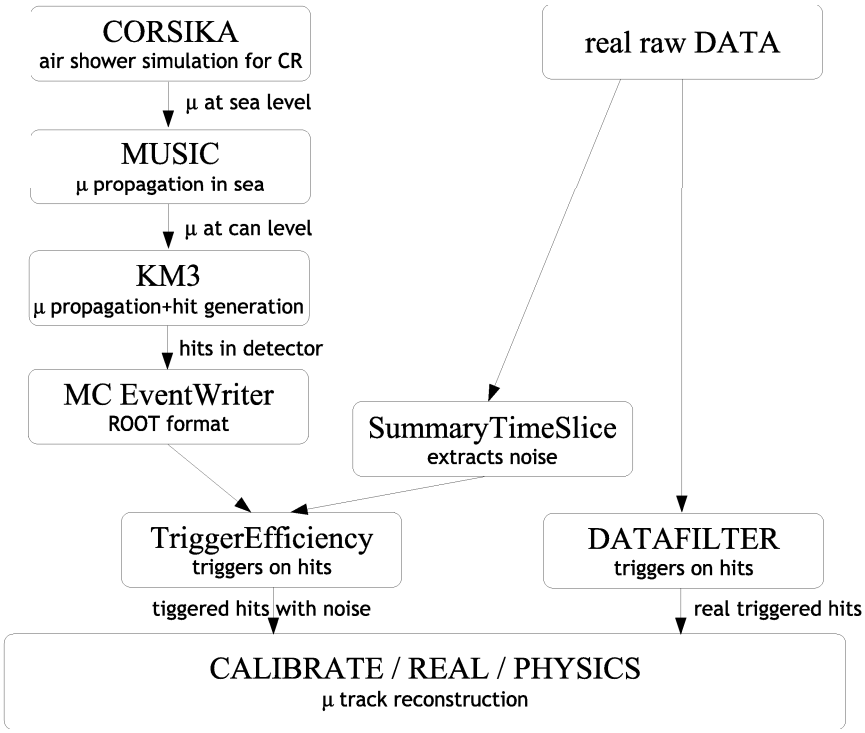

Figure 4.2: *Overview of the simulation and analysis chain for Line 1.*

The performance of the reconstruction algorithm was first studied on MC files with and without background noise. With the reconstruction algorithm shown in Figure 4.1 (and a repetition of the last two minimisation methods), the reconstructed (black) and true (red) zenith angles of the muons and the difference between the two are presented in Figure 4.3. The initial scan provides a first starting point which is already within 14° of the true zenith angle and is further used as input for the successive minimisation algorithms. The SIMPLEX algorithm yields a continuous angular distribution with the main peak resembling the true distribution and a small adjacent peak already emerging. The deviation from the true value is typically around 12°. The MIGRAD method further improves the resolution of the main peak to 6° at the expense of a more pronounced tail with errors of up to 100°. The zenith angle distribution also features two distinct peaks, the smaller secondary peak being due to geometric ambiguities in the reconstruction if only one side of the Cherenkov wavefront is detected. This effect can lead to a serious shift in the zenith angle of the reconstructed events, as a downward-going muon can be falsely identified as an upward-going muon (see Figure 4.4), thus introducing fake solutions. This ambiguity can also occur as fringe effect in a greater detector comprising more than one line if the geometry is such that only one side of the Cherenkov cone is detected. A further consec-

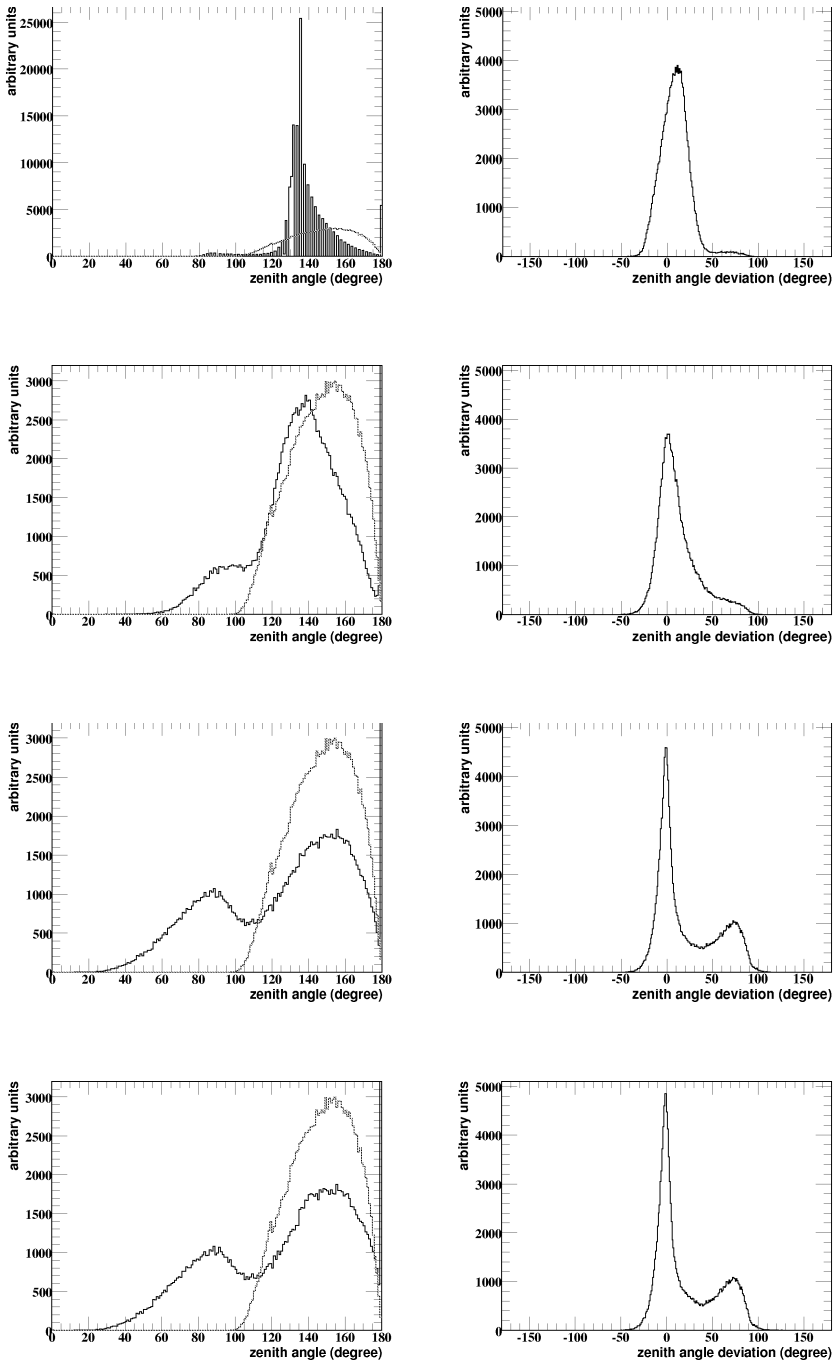

Figure 4.3: *Evolution of zenith angles and zenith angle deviations after the initial scan and different stages of the minimisation algorithms.*

utive implementation of the SIMPLEX and MIGRAD algorithms shows almost no improvement in track reconstruction and is thus no longer used.

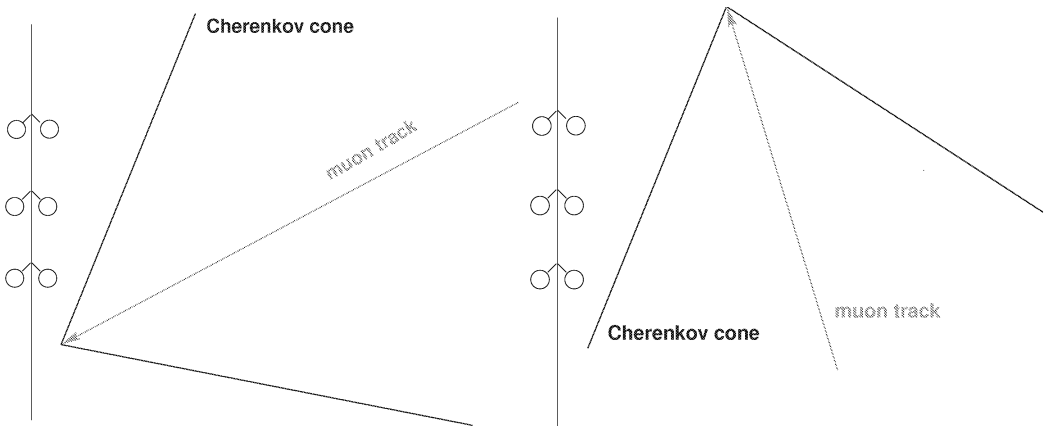

Figure 4.4: *Origin of the zenith angle ambiguity at Line 1: if only one side of the Cherenkov cone is detected, a downward-going muon (left) can be mistaken for an upward-going muon (right).*

Another explanation for the poor reconstruction quality with Line 1 is provided by the fact that atmospheric muons, which have been dealt with here, are very likely to arrive at the detector in bundles. As these muons are produced in abundance in air showers, bundles of parallel muons with multiplicities of up to 20 can simultaneously penetrate the detector. As the reconstruction algorithm assumes that a single muon track traverses the detector, the calculated hit time residuals which have to be minimised are no longer valid a priori, thus degrading the resolution.

Moreover, it was not possible to take the deflection of the detector line and, as a result, the uncertainty in the position and heading of the OMs into consideration in the reconstruction study presented above, as the relevant alignment information is not available for the analysed period. However, it was possible to study the impact of distorted line shapes due to different sea-current velocities on the angular resolution by using a detector distorted by sea current in the simulation and a straight line detector for reconstruction. Figure 4.5 left illustrates the change in the zenith angle distribution for weak and strong sea currents. The red curve represents the zenith-angle deviation corresponding to a line shape at 23 cm/s and background noise, whereas the blue curve corresponds to a more moderate sea current velocity of 7.5 cm/s and likewise includes background noise. The main difference is the drop in well-reconstructed events due to the increasing uncertainties in the OM positions, which are the result of more pronounced line deflections: the top storey of the line suffers a displacement of about 20 m at a sea current of 23 m/s.

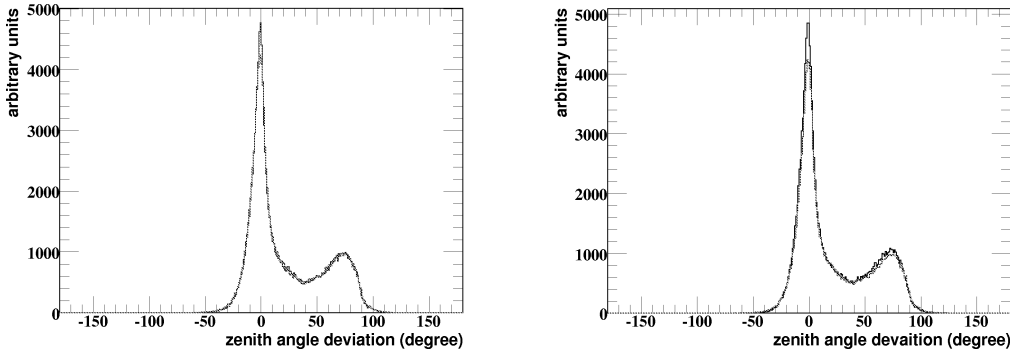

Figure 4.5: *Difference between reconstructed and MC zenith angle of a sample of atmospheric muon events. Left: Background noise and sea current of 7.5 cm/s (blue) and 23 cm/s (red) respectively. Right: With (red) and without (black) background noise.*

Changes in the zenith angle distribution have also been studied with regard to dependence on the presence and absence of background noise. Figure 4.5 right illustrates the difference in zenith-angle deviation due to added background light (red) compared to the case of pure signal hits (black). As the reconstruction algorithm uses only triggered L1-hits as input, which have been checked for coincidences and high amplitudes, chances are generally small that random background hits will intrude into the reconstruction algorithm and detract from its purity.

Examples of real data events reconstructed with the Line 1 strategy described in section 5.1 are presented in Figure 4.6. All the hits belonging to an events are displayed with the triggered hits represented as dots and the untriggered hits as crosses. The hit altitude – with the zero-point at the centre of the line – is plotted against the hit time so that hits belonging to a muon track lie on a hyperbola. The hyperbola obtained as a fit to the hits is also shown. However, the track direction is not immediately obvious from the hyperbolas shown in Figure 4.6. All the events shown have been reconstructed as down-going events and are therefore considered to be atmospheric muons.

In the current state, no quality cuts are being applied to the reconstructed events since the data and Monte Carlo have not been comprehended in detail. Therefore it seems precarious to exclude events without a profound understanding of the reason. However, as Line 2 is also operational now, it may be expected that the reconstruction quality will improve rapidly as the geometric ambiguity and azimuthal symmetry of the detector no longer provide sources of confusion. Instead

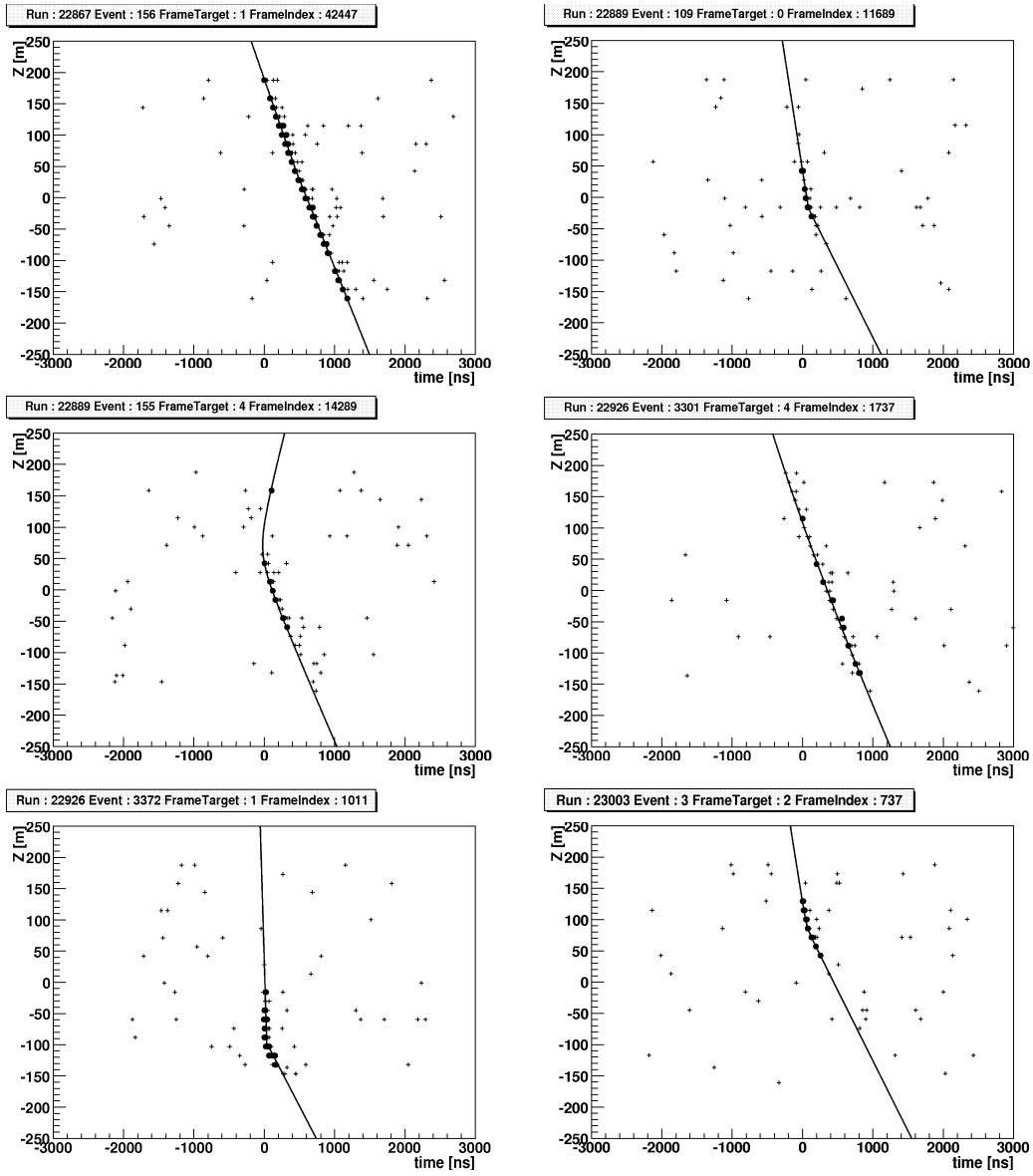

Figure 4.6: *Examples of real events reconstructed with the Line 1 strategy described in section 5.1. The black dots represent the triggered hits in the event, and the line shows the fitted hyperbola.*

of the ambiguities of a single line, the combination of two and more detector lines features a sensible lever arm better suited to the reconstruction of long-range muons. Figure 4.7 is an exemplary illustration of an event reconstructed with both detector lines, leaving no doubt of the muon's direction.

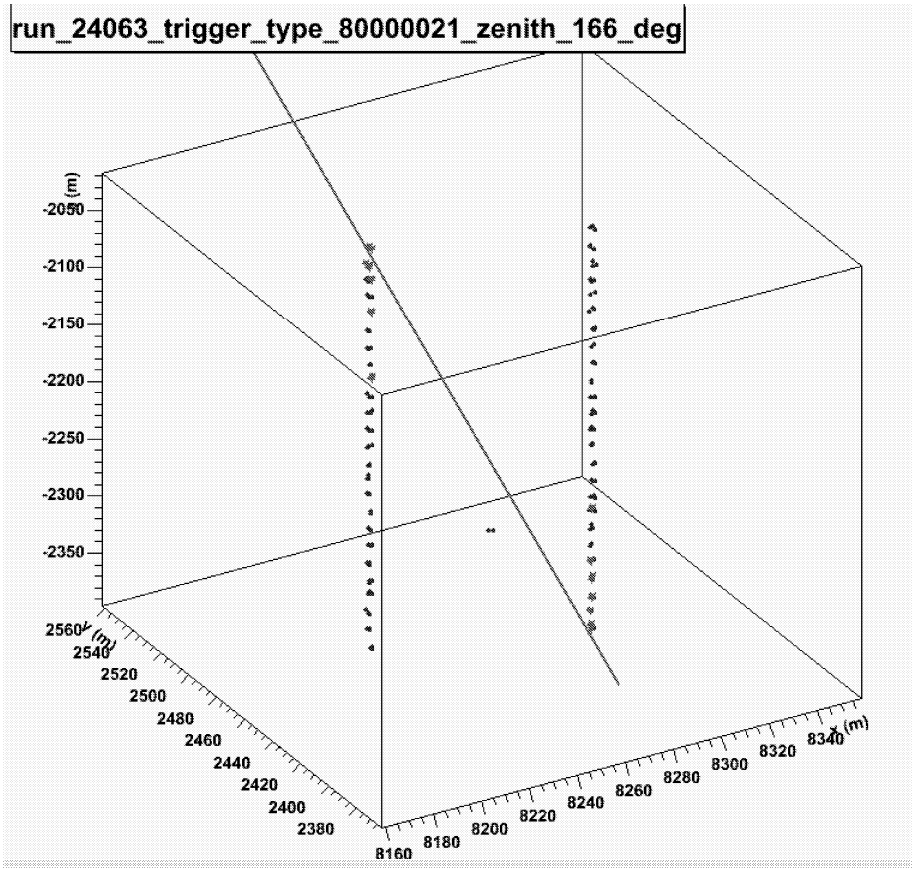

Figure 4.7: *Example of a reconstructed muon event recorded with both detector lines [51]. The red line represents the muon track.*

5 Gamma-ray bursts as candidate sources of neutrinos

The detection of high-energy neutrinos from Gamma-Ray Bursts (GRBs) would provide the ultimate evidence sought to confirm the acceleration of hadronic matter in astrophysical sources up to very high energies of 10^{15} eV. While the presence of electrons and their shock acceleration is indicated by the synchrotron and inverse Compton emissions, which are manifest in the prompt γ-rays of the observed burst, the acceleration of protons remains an assumption.

Photohadronic neutrino production is a result of the decay of charged pions originating from interactions of high-energy protons with ambient low-energy photons. While neutrinos are produced exclusively by charged pion decay, gamma-rays are not necessarily the product of π^0-decay, but may also originate from inverse Compton scattering of low-energy photons with shock-accelerated electrons. Therefore, even the observation of sources emitting TeV γ-rays with imaging air Cherenkov telescopes cannot demonstrate beyond doubt the acceleration of hadrons and thus the origin of cosmic rays. For this reason the detection of high-energy cosmic neutrinos would be a landmark observation because it has never been done so far, except in the case of a few low-energy neutrinos of the supernova SN1987A.

Gamma-Ray Bursts are particularly good candidates for a position among the first sources to be detected by ANTARES. First, they are among the most energetic known phenomena, releasing typically $10^{51} - 10^{54}$ erg/s in gamma-ray luminosity per burst[1], with additional $\sim 10\%$ of the total luminosity supposedly converted to a burst of $\geq 10^5$ GeV neutrinos. Second, as they are transient point sources, the directional and time information provided by multi-messenger observations, such as γ-telescopes, can be leveraged to undertake an essentially background-free search for neutrinos from GRBs.

[1] more than would be generated if the entire mass of the Sun were converted into γ-rays

A brief history of GRBs

GRBs were discovered accidentally on 2nd July 1967 by the Vela military satellites monitoring for nuclear explosions to verify compliance with the Nuclear Test Ban Treaty. The observation of short and very intense flashes of gamma-rays, which did not come from Earth's direction, was first considered to be a possible signal from an advanced extraterrestrial civilisation. However, it soon became clear that this was a fascinating new cosmic phenomenon and the discovery was eventually published in 1973 [52].

In the years that followed, a lack of key observational data led astronomers to believe that GRBs were of galactic origin, which appears reasonable in view of the extremely high intensity of the bursts. Real progress in the field began in 1991, when NASA launched the Burst and Transient Source Experiment (BATSE) on board the Compton Gamma-Ray Observatory (CGRO) (see section 5.2). The observations showed complete isotropy of GRBs throughout the sky, thus ruling out galactic origin. Since gamma-rays are hard to focus, BATSE was unable to pinpoint the location of GRBs to much better than 1 or 2 degrees, thus rendering impossible any follow-up observation of the predicted "afterglow" by ground-based telescopes.

The next breakthrough occurred in 1997, when the Beppo-Sax satellite succeeded in obtaining high-resolution x-ray images of the afterglow from GRB970228, followed by more observations made in optical and longer wavelengths with an angular resolution of arcminute precision. This accurate angular resolution allowed redshift measurements, which led to the identification of the host galaxies. Although a great deal of progress has been made in understanding the GRBs, many questions still remain unanswered, most importantly that of the progenitor(s) which is closely connected to the nature of the "inner engine".

Possible progenitors

Since afterglow observations suggest that GRBs are predominantly generated in host galaxies and are likely to be the result of stellar processes, research into stellar progenitors has been undertaken. These progenitor stars have to undergo a catastrophic energy release event towards the end of their evolution.

One class of candidate involves super-massive stars whose core collapses result in a failed supernova, often referred to as a hypernova or collapsar scenario. As matter falls into the black hole created in this process, gravitational energy is transferred to bulk kinetic energy, which generates the relativistic jet that penetrates the stellar envelope and produces the fireball. This scenario is supported by growing evidence for GRBs occurring in star-forming regions within their host

galaxies. Magnetars, which result in a rapidly spinning neutron star featuring an extremely strong magnetic field, are also a possible subset of the core collapse model. Another class of candidates consists of neutron star binaries or black hole binaries in close binary orbits which lose orbital angular momentum by radiating gravitational waves and finally undergoing a merger.

Both of these progenitor types are expected to lead to the formation of a black hole surrounded by a temporary debris torus which is accreted onto the black hole, thus giving rise to a fireball due to the enormous compressional heating and dissipation. Most of the star's binding energy could be released, providing strange matter were present. It is anticipated that a seed of strange hadrons could start a chain reaction leading to the conversion of what was once a neutron star to a completely strange star [53].

A link between GRBs and supernovae was first established by observing GRB030329, one of the brightest and closest gamma-ray bursts on record [54]. Ground-based follow-up observations of its afterglow, visible at x-ray, radio and visible wavelengths, revealed for the first time that a GRB and a supernova had essentially occurred simultaneously. However, only characteristic spectral features of a supernova observed directly in the fading afterglow of a GRB could provide direct evidence for the supernova connection. The recent observation of the presence of emission lines in GRBs [55] seems to provide evidence in favour of the collapsing stars as progenitors.

An interesting modification of the collapsar model has been suggested [56], named the supranova model, thus reflecting its strong responsiveness to the supernova connection. The model presupposes a supernova explosion in the beginning, which leaves behind a supramassive neutron star of $\approx 2.5 - 3$ solar masses. Due to its excess of rotational energy, it fails to collapse further until it loses sufficient rotational energy to finally implode in a black hole and thereby trigger a GRB. The most natural process by which the supramassive neutron star can lose its rotational energy is by a strong pulsar-type wind, which is thought to create a pulsar wind bubble (PWB).

While the progenitors of GRBs have not been well identified so far, it is interesting to note that the bimodal time distribution of bursts may also point to multiple GRB classes and associated progenitors.

5.1 The fireball model

The widely accepted interpretation of the phenomenology of GRBs is summarised in the relativistic internal-external shocks fireball model (see [57] for review).[2] General phenomenological considerations based on GRB observations indicate that, regardless of the nature of the underlying sources which are not yet known, GRBs are produced by the dissipation of the kinetic energy of a relativistically expanding wind, a "fireball".

The non-thermal spectra indicate that the observed emission emerges from an optically thin region, and at the same time the rapid variability times imply that the sources must be very compact and therefore optically extremely thick to pair production, suggesting the existence of a thermal plasma of photons, electrons and positrons, which seems to be in contradiction to the first observation. The optical depth is therefore reduced by the assumption of an ultra-relativistic expansion of the source powered by radiation pressure, which leads to the relativistic fireball model. In this model relativistic expansion with increasing velocity will occur until the fireball becomes transparent and the radiation can be released, which is what we observe as GRB. Moreover, the relativistic expansion reduces the photon energy in the source frame by the factor Γ, the wind bulk Lorentz factor, compared to the energy in the observer frame, thus lowering the photon energy below the pair production threshold. To obviate the compactness limit, the shocks have to be extremely relativistic with $\Gamma \approx 300$.

For a relativistically expanding source, the size constraint implied by the short variability time has to be modified: since the radiation seen by a distant observer originates from a conical section of the source with opening angle $\propto 1/\Gamma$, photons emitted at the edge of the cone are delayed, compared to those emitted on the line of sight by $R'/2\Gamma^2 c$. Thus the limit on the source size set by the variability time scale Δt is

$$R' \approx 2\Gamma^2 c \Delta t \tag{5.1}$$

with primed quantities referring from now on to the rest frame of the fireball.

In the fireball model, an inner compact source produces a variable relativistic wind. During expansion, the opaque fireball cannot radiate and any particles present, leptons and baryons alike, will be shock-accelerated, thus converting radiation into bulk kinetic energy. When radiation is eventually emitted, the fireball expands at constant velocity, which is determined by the amount of baryonic matter present because it increases the optical depth due to Thompson scattering. The flow of the relativistic ejecta is not steady but, similar to the emission of jets in AGNs, composed of multiple shocks expanding with a range

[2] Other models that describe the GRB observations also exist, such as the so-called "Cannonball Model", but they are not considered in this work.

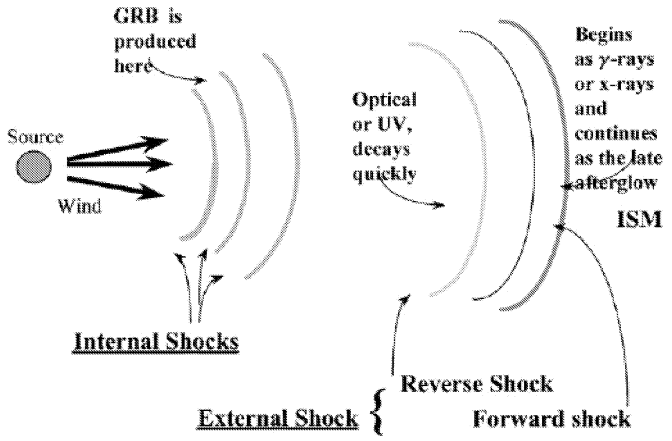

Figure 5.1: *The internal-external shock scenario of the fireball model taken from [57]. See text for further explanation.*

of velocities. Relativistic internal shocks arise in this irregular flow when faster shells overtake slower ones (see Figure 5.1). As the fireball expands further, it drives the relativistic forward shock into the ambient medium, for instance into the interstellar matter (ISM) if the GRB occurs within a galaxy, and a reverse shock moves backward into the ejecta as the latter is decelerated by interaction with the external medium.

As the fireball continues to plough into the external medium, it is slowed down further by the surrounding matter, thereby continuously heating new gas and producing relativistic electrons which give rise to the delayed afterglow radiation observed on time scales typically in the order of days to months. In this phase the flow is regular and approaches the adiabatic self-similar solution. The radiation emitted by the reverse shocks during the transition to self-similar expansion is the afterglow emission. It evolves progressively and peaks in the x-rays, then UV, optical, IR and radio.

The question of the fireball geometry is raised when observing GRBs at large redshifts, whose γ-ray fluences imply a total photon energy of $10^{52}-10^{54}(\Omega_\Gamma/4\pi)$ erg, where Ω_Γ is the solid angle into which the γ-rays are beamed. If the fireball were spherically symmetric, the released energy would correspond to more than the entire mass of the Sun or a neutron star converted into gamma-rays, whereas a beamed jet would alleviate the energy requirements, and corroborative observational evidence suggests that the outflow from a GRB is collimated. Several afterglow emissions have been observed to fade more quickly over time, which hints at changes in the geometry of the emitting regions. When the jet expands into the surrounding medium, it decelerates and beams its radiation to a larger

angle. As the beam becomes less collimated it causes the afterglow to start to fade more rapidly than expected without beaming. Since this sudden break in the afterglow light curve occurs at all wavelengths, it can be used to calculate the initial opening angle of the cone and hence the total energy release at the source. To understand the break in the light curve due to beaming, it is essential to differentiate between "geometric" beaming into an angle θ_j and purely relativistic beaming due to the Lorentz boost Γ, which in the observer frame results in a net beaming into a cone with opening angle $\theta_\Gamma \approx \Gamma^{-1}$. But the relativistic beaming simply sets a lower limit on the beaming angle. A distant observer will only be able to distinguish between a spherical fireball and a jet-like fireball if the source has an opening angle $\theta_j < \Gamma^{-1}$, which leads to a break in the light curve as the received flux decays faster when no new radiating surface is added (see Fig. 5.2).

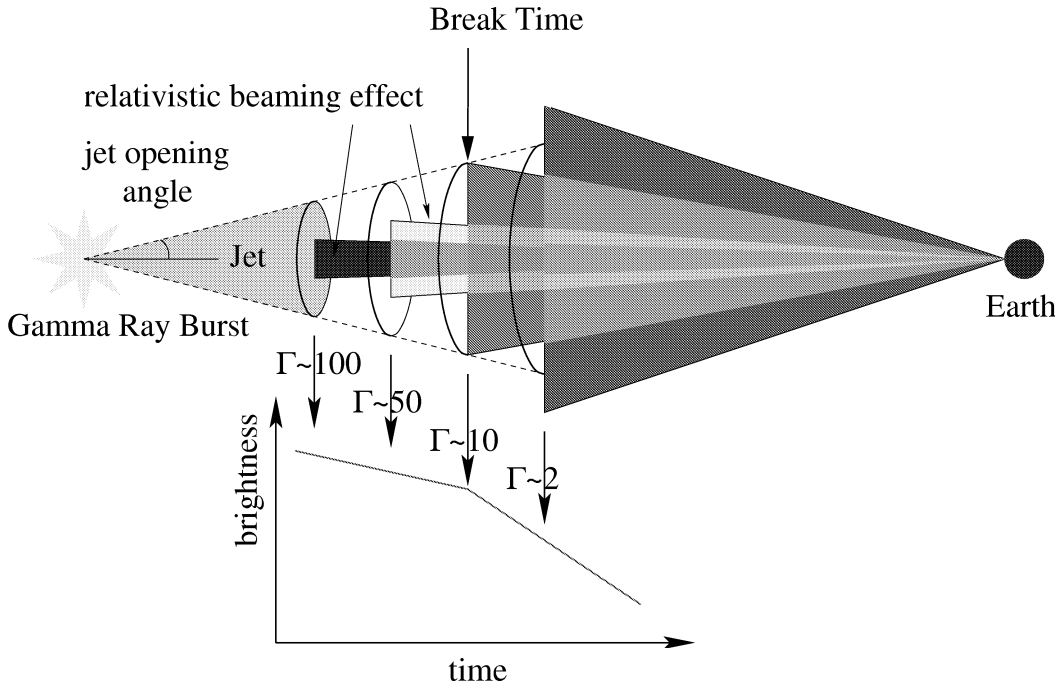

Figure 5.2: *An illustration in the break of a decelerating conical jet with a constant geometrical opening angle θ_j, here to be taken as 0.1 radian. The coloured cones represent the cones within which photons emitted by the jet can reach the observer on Earth.*

If the outflow from a GRB is indeed collimated, then the number of GRBs occurring is much higher than what is observed because only a fraction of the ensuing jets will be aimed at the Earth. However, depending on the angular structure of the jet, off-axis emissions from more slowly moving matter will occur. This material will be less affected by Doppler shifting and its intensity will therefore be expected to peak at lower frequencies than the on-axis emission. Hence a

particular class of objects, referred to as X-ray flashes, could be associated with GRBs seen slightly off-axis [58][59].

5.2 Pilot GRB survey with BATSE

The experiment with the best statistics in collecting data on GRBs so far has been the Burst and Transient Source Experiment (BATSE, [60]) on board the NASA Compton Gamma-Ray Observatory (CGRO). It consisted of eight detector modules made of 58.5 cm in diameter by 1.27 cm thick NaI scintillator discs, sensitive to gamma-rays from ∼25 to ∼1000 keV. The geometry of the experiment made burst direction reconstruction with an accuracy down to very few degrees possible.

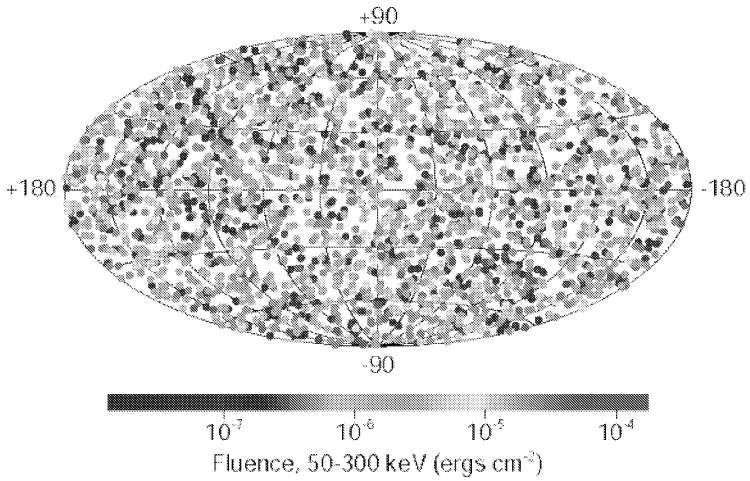

Figure 5.3: *The final BATSE sky map of GRB locations and fluences comprising 2704 measured GRBs shows them to occur at random locations in the sky. [61]*

While in operation during 1991-2000, BATSE detected and classified 2704 individual GRBs. Our knowledge about the cosmological distances of the bursts, as indicated by their isotropic distribution in the sky with no dipole or quadrupole moments (see Figure 5.3) and their non-thermal spectra is due in large part to the precise measurements made by BATSE. The duration of the bursts is measured in T_{90}, which denotes the time in which 90% of the total flux (at MeV energies) is emitted, and ranges from 10^{-3} to about 10^{3} s (Figure 5.4 left). Since the time distribution is markedly bimodal, the bursts are generally classified as long- and short-duration bursts. The X-Ray Flash candidates among the bursts are also shown.

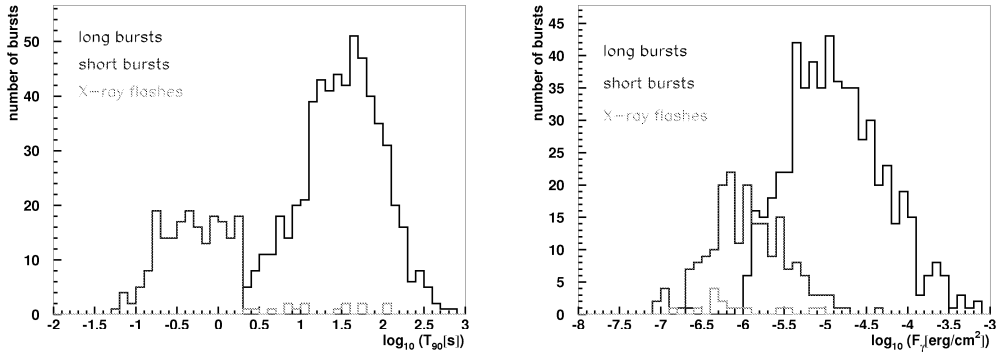

Figure 5.4: *Time and fluence distribution of BATSE bursts, which are used for analysis in this work.*

The measured γ-spectrum

The spectrum of a GRB can provide information about the burst energetics, acceleration mechanisms and the overall expansion of the fireball. Unlike the extreme variations in the light curves, the spectra of GRBs are fairly homogeneous. The photon spectrum of most GRBs in the BATSE spectral energy range can be parametrised by a broken power-law with a break energy E_b, at which the spectral slope changes from a low-energy index α to the high-energy index β [62]. However, the spectral parameters α, β, and E_b vary from burst to burst with no universal values.

$$F_\gamma = E_\gamma \frac{dN_\gamma}{dE_\gamma} \propto \begin{cases} E_\gamma^{-\alpha}, & E_\gamma < E_b \\ E_\gamma^{-\beta}, & E_\gamma > E_b. \end{cases} \tag{5.2}$$

Figure 5.4 right illustrates the wide range of fluences measured by BATSE for different burst categories. The break in the spectrum, E_b, ranges from below 100 keV to above 1 MeV, but peaks below 200 keV with only a small fraction of spectra breaking above 400 keV. In most emission models the break energy usually reflects some characteristic electron energy and could indicate the energy above which all electrons "cool" - rapidly radiating all of their kinetic energy within the source [12]. Although it has been suggested that synchrotron emission is a likely source of radiation from GRBs [63], there has since been a lot of controversy over what radiation mechanism actually gives rise to the observed spectra.

The BATSE burst samples the following analysis is based upon are extracted from [64] due to the fact that it is necessary for the key burst parameters beyond

the ones given in the catalogue to be known, which would require a detailed astrophysical analysis of the lightcurves. These parameters are the spectral coefficients α and β together with the break energy E_b and the fluence F_γ, which determine the photon spectrum. Furthermore, the variability time Δt, the redshift z, the gamma-ray luminosity L_γ and the bulk Lorentz factor Γ of the burst have to be already known. Since the redshift was measured only for 13 long-duration bursts, Guetta et al. [64] had to estimate the redshift of the others using the variability of the GRBs. As this method applies only to long-duration bursts, the short duration bursts and X-ray flash candidates in the sample were set to $z = 1$. From the redshift, which is a measure of the co-moving distance, and the fluence the isotropic-equivalent luminosity was calculated, which provided the final ingredient for the calculation of the bulk Lorentz factor. All the BATSE GRBs for which these parameters could be extracted were included in this sample: 579 long-duration bursts, 199 short-duration bursts and 15 X-ray flash candidates. A detailed description of the determination of the above-mentioned parameters is given in [64].

5.3 Neutrino flux calculation in the standard fireball model

In the case of synchrotron radiation from accelerated electrons as a viable emission process, it can be assumed that protons are also accelerated along with the electrons.

The calculation of the neutrino flux is performed in the standard fireball model with internal shock waves [13], whereby Fermi shock-accelerated protons interact with GRB photons via photo-meson production to produce neutrinos. The basic idea of the fireball model with internal shocks is that the fireball energy is dissipated equally in electrons and protons. The physical conditions in the dissipation region allow Fermi shock acceleration of both particles to the highest energies, the only difference being their cooling mechanisms. While electrons lose their energy emitting synchrotron radiation and interact with their own synchrotron photons to produce "self-inverse Compton" radiation, protons tend to interact with the synchrotron photons to produce pions. In this process, the Δ-resonance is excited, which subsequently decays into either π^+ and neutron, or π^0 and proton. The branching ratios for the two reaction chains are almost identical, which leads to the assumption that π^+ and π^0 are produced in equal amounts[3]. In the

[3]While at the Δ-resonance π^0 are produced with higher probability than π^+, the simplified assumption of equal amounts still holds with regard to the wider energy region starting at the threshold energy for pion production at 150 MeV until 1200 MeV.

subsequent decay chain the neutral pion produces two high-energy photons, while the charged pion decays into leptons and neutrinos.

$$\begin{aligned} p\gamma \rightarrow \Delta^+ \rightarrow p\pi^0, \quad & \pi^0 \rightarrow \gamma\gamma \\ p\gamma \rightarrow \Delta^+ \rightarrow n\pi^+, \quad & \pi^+ \rightarrow \nu_\mu \mu^+ \rightarrow \nu_\mu \bar{\nu}_\mu \nu_e e^+. \end{aligned} \tag{5.3}$$

Normally, these first-generation gamma-rays cannot leave the emission region, but, instead, induce an electromagnetic cascade through pair production with low-energy background photons and subsequent synchrotron radiation of electrons and positrons. They cascade down in energy, until they eventually escape below some critical energy level at which the emission region finally becomes optically thin. Therefore, the only original outburst particles accompanying the GRB-photons visible at cosmological distances are the neutrinos.

In this model, the neutrino spectrum is determined by the observed low-energy gamma-ray spectrum, which is well described by a broken power-law (see above), and the proton spectrum. The latter is assumed to be a power-law distribution, $dN_p/dE_p \propto E_p^{-2}$, due to Fermi acceleration of the protons in a Newtonian (non-relativistic) shock up to energies greater than 10^{20} eV. The interaction of these protons with GRB photons results in a broken power-law neutrino spectrum, essentially tracing the photon spectrum, with the neutrino break energy E_ν^b fixed by the threshold energy of protons for Δ-photo-production:

$$E_p' \geq \frac{m_\Delta^2 - m_p^2}{4E_\gamma'}. \tag{5.4}$$

In our observer's frame this threshold energy translates to $E_p \geq E_p' \cdot \Gamma^2$, where Γ is the plasma bulk Lorentz factor. The energy of a neutrino produced in the decay chain (see Eq. 5.3) by a proton with energy E_p would yield $E_\nu = \frac{1}{4}\langle x_{p\rightarrow\pi}\rangle E_p$. The factor 1/4 reflects the fact that the energy is approximately evenly distributed between the π^+ decay products, and $\langle x_{p\rightarrow\pi}\rangle$ is the mean fraction of energy lost to pion production by high-energy protons, usually 20%. Hence the neutrino break energy results in

$$E_\nu^b = \frac{1}{4}\langle x_{p\rightarrow\pi}\rangle E_p = 5 \cdot 10^{14} \frac{\Gamma_{300}^2}{E_{\gamma,MeV}} eV. \tag{5.5}$$

Here $\Gamma_{300} = \Gamma/300$, which corresponds to the mean value of Γ, and $E_{\gamma,MeV} = E_\gamma/1MeV$. This does not take into account the evolution of the source. In cases in which the GRB redshift z could be measured by afterglow observations of iron K-α emission lines (of a pre-ejected shell), the observed break energy correctly reads

$$E_\nu^b = 5 \cdot 10^{14} \frac{1}{(1+z)^2} \frac{\Gamma_{300}^2}{E_{\gamma,MeV}} eV. \tag{5.6}$$

The dependence on the source redshift is quadratic since both the proton energy and the photon energy are shifted by the factor $(1+z)$. A second and third break energy in the high-energy region of the neutrino spectrum will occur due to the synchrotron losses of muons and pions. At very high energies the radiative losses of charged particles compete with the decay processes, and if the synchrotron loss time becomes shorter than the lifetime of the particle $t'_{snc} \leq \tau'$, cooling via synchrotron radiation will be preferred. Thus muons and pions producing neutrinos at energies higher than the respective synchrotron break energy E_μ^s or E_π^s will adiabatically lose a significant part of their energy before decaying. This effect results in reduced neutrino energies. For the sake of simplicity, it is generally assumed that the slope of the neutrino spectrum steepens by a factor of 2 above the synchrotron break energy E^s.

The particle's lifetime τ at rest is relativistically extended to $\tau' = \tau \cdot E/(mc^2)$. In comparison, the synchrotron energy loss of a charged particle in a magnetic field B' is

$$-\frac{dE}{dt} = \frac{4}{3}\sigma_T c \left(\frac{E}{mc^2}\right)^2 \cdot \frac{B'^2}{8\pi} \left(\frac{m_e}{m}\right)^2, \tag{5.7}$$

where σ_T is the Thomson cross-section. The magnetic field can be estimated from the observed γ-ray luminosity L_γ by the assumption that the internal energy carried by the magnetic field,

$$L_B = \frac{4\pi R^2 c \Gamma^2 B'^2}{8\pi}, \tag{5.8}$$

is a fraction of the total wind luminosity $L_B = \xi_B L_{tot}$, which in turn is related to the observed luminosity by $L_\gamma = \xi_e L_{tot}$. Here, $R \sim 2\Gamma^2 c\Delta t$ is the collision radius of different shells (see Eq. 5.1).

A comparison of the synchrotron loss time with the lifetime of a particle yields:

$$\frac{t'_{sync}}{\tau'} = \frac{12\pi m^5 c^8}{\sigma_T m_e^2 \tau} \cdot \frac{\Gamma^8 \Delta t^2 \xi_e}{E^2 L_\gamma \xi_B} \leq 1. \tag{5.9}$$

The equipartition fractions ξ_e and ξ_B cannot be determined by present observations and are basically unknown. However, in various fireball models they are estimated to be close to unity. In order to become the dominant process, the synchrotron loss time has to be shorter than the lifetime. This requirement defines the synchrotron break energy as follows

$$E_\mu^s = \frac{3 \cdot 10^{15}}{1+z} \cdot \frac{\Gamma_{300}^4 \Delta t_{ms}}{\sqrt{L_{\gamma,51}}} GeV \tag{5.10}$$

if we also take the energy redshift at the source into account. Here $\Delta t_{ms} = \Delta t/1$ ms and $L_{\gamma,51} = L_\gamma/10^{51}$ erg/s are the observed gamma-ray luminosity. Since the lifetime of π^+ is a hundred times shorter than that of a muon, and both have roughly the same mass, the synchrotron break energy of the pion will be 10 times higher: $E^s_\pi = 10E^s_\mu$.

The normalisation of the flux is determined by the efficiency of pion production in the fireball. The neutrino flux is normalised to the γ-fluence of a GRB by estimating the fraction f_π of fireball energy lost to pion production. The fraction of energy converted to pions f_π can be estimated either by looking at the ratio of the wind expansion time to the time available for pion production or by the ratio of the size of the shock $\Delta R'$ to the mean free path of a proton $\lambda_{p\gamma}$:

$$f_\pi = \frac{\Delta R'}{\lambda_{p\gamma}} \langle x_{p\to\pi} \rangle = \Delta R' \cdot n'_\gamma \sigma_\Delta \langle x_{p\to\pi} \rangle. \tag{5.11}$$

The number density of photons in the fireball n'_γ can be computed from the photon energy density U'_γ and the photon energy to $n'_\gamma = U'_\gamma/E'_\gamma$. The energy density is related to the fireball luminosity:

$$U'_\gamma = \frac{L_\gamma}{4\pi R'^2} \cdot \frac{\Delta t'}{\Delta R'}. \tag{5.12}$$

The radius of the fireball has been estimated to be $R' = 2\Gamma^2 c\Delta t$ (see Eq.5.1). Inserting this into the equation above and allowing for relativistic effects on the variability time and energy, the photon number density becomes

$$n'_\gamma = \frac{L_\gamma}{16\pi\Gamma^4 c^2 \Delta t \Delta R' E_\gamma}, \tag{5.13}$$

and hence the fraction of proton energy converted to pions is

$$f_\pi = \frac{L_\gamma \sigma_\Delta \langle x_{p\to\pi} \rangle}{16\pi\Gamma^4 c^2 \Delta t \Delta R' E_\gamma} \approx 0.20 \cdot \frac{L_{\gamma,51}}{(E^b_{\gamma,MeV})\Gamma^4_{300}\Delta t_{ms}}. \tag{5.14}$$

Thus, for a typical burst 20% of the fireball energy is expected to be converted into pions by photoproduction, which means that 10% of the energy will be transferred to neutrinos.

At first glance it seems as if the strong dependence on the bulk Lorentz factor Γ, which varies considerably from burst to burst, might result in the domination of the neutrino flux by a few bright bursts with f_π close to unity. However, f_π is also constrained by the fact that the observed characteristic photon energy is $\sim$ 1 MeV, which implies that the wind model parameters (Γ, L, Δt) are correlated. If Γ was much smaller than average, the fireball would become very dense, resulting in high values for f_π and abundant neutrino production. But in this case the

fireball would generate a thermal photon spectrum instead of the observed power-law spectrum. Thus, as a first approximation, it seems reasonable to simply fix $f_\pi = 0.2$ at the neutrino break energy and derive the neutrino flux directly from the γ-flux. However, it is circumspect to do the analysis both ways, also using the accurate expression for f_π, in order to be able to compare the results of the two models. In the following, model 1 denotes the neutrino flux which uses $f_\pi = 0.2$ – a kind of generic model –, and model 2 refers to the neutrino flux which uses Eq. 5.14 for normalisation and hence represents a more sophisticated and individualistic model. The flux for each of the neutrinos $\nu_\mu, \bar{\nu}_\mu, \nu_e$ is

$$E_\nu^2 \frac{dN_\nu}{dE_\nu} = \frac{1}{8\xi_e} \frac{F_\gamma}{\ln 10} f_\pi \cdot \begin{cases} (E_\nu/E_\nu^b)^\beta, & E_\nu < E_\nu^b \\ (E_\nu/E_\nu^b)^\alpha, & E_\nu^b < E_\nu < E_\nu^s \\ (E_\nu/E_\nu^b)^\alpha (E_\nu/E_\nu^s)^{-2}, & E_\nu > E_\nu^s, \end{cases} \tag{5.15}$$

where E_ν^s is the synchrotron break energy of the pion $E_{\nu,\pi}^s$ for the ν_μ flux, and $E_{\nu,\mu}^s$ for the $\bar{\nu}_\mu$ and ν_e flux components. The factor 1/8 indicates that 1/2 of the produced pions are π^+, which decay into neutrinos, and each neutrino will carry approximately 1/4 of the pion energy.

The difference between the two models reflects the systematic errors on the calculated neutrino spectra. Since the theoretical uncertainties in the fireball model are of the same order of magnitude as the errors on the measured parameters, especially the variability time Δt_{ms}, which can only be measured to the smallest time scale detectable with reasonable statistics, model 2 merely appears to be more accurate than the generic model 1 but this is not necessarily the case.

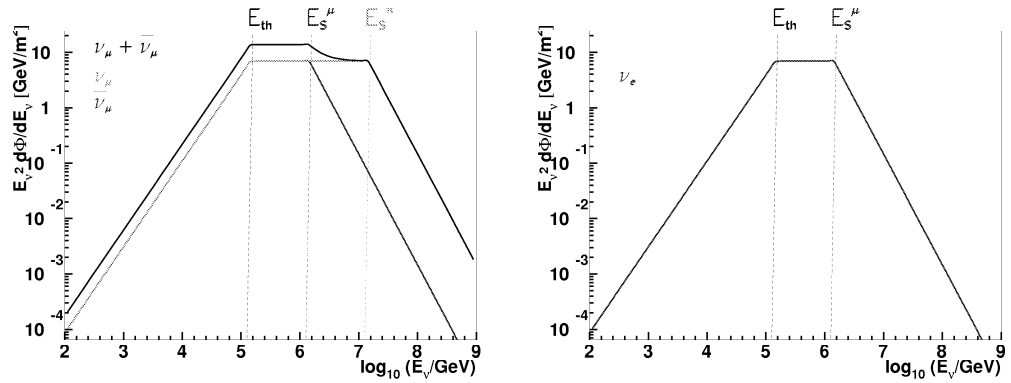

Figure 5.5: *E^2-weighted flux of muon neutrinos $\nu_\mu + \bar{\nu}_\mu$ and electron neutrinos ν_e from decays of the specified particles according to model 2.*

The electron neutrino and muon neutrino spectra with the components $\nu_\mu, \bar{\nu}_\mu$ are shown in Fig. 5.5 exemplary for GRB . The $\bar{\nu}_\mu$ and ν_e spectra are identical

because they both originate from the muon decay, whereas the ν_μ component breaks at a level of a decade higher in energy due to its parent particle, the pion.

In total, 793 individual neutrino fluxes have been calculated from GRBs listed in the pre-analysed BATSE sample, which constitute a representative sample, including strong and weak bursts alike, because no selection has been applied other than that concerning the possibility of extracting the necessary parameters. From these individual fluxes an average GRB neutrino flux has been determined without the application of any weights. Therefore the average flux is as realistic as possible but the deviation of individual fluxes from the mean is relatively high.

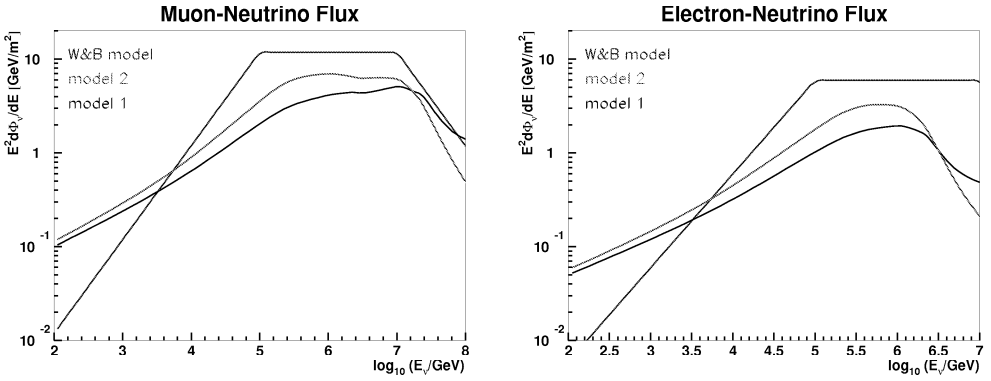

Figure 5.6: *E^2-weighted flux of muon neutrinos $\nu_\mu + \bar{\nu}_\mu$ and electron neutrinos ν_e for the specified models.*

Furthermore, it is interesting to compare the average flux of model 1 and 2 with the Waxman&Bahcall flux, which constitutes a universally diffuse neutrino flux produced by all the GRBs. In their derivation (see [14] and [65]), Waxman and Bahcall assume the GRBs to be the sources of ultra-high-energy cosmic rays (UHECRs) because the spectrum of UHECRs in the energy range $10^{19} - 10^{21}$ eV, where the extragalactic component is dominant,

$$E_{CR}^2 \frac{d\dot{N}_{CR}}{dE_{CR}} \approx 10^{44} \quad \text{erg Mpc}^{-3}\ \text{yr}^{-1}, \tag{5.16}$$

is remarkably similar to the generation rate of high-energy protons in the GRB fireball model (see Figure 5.7), which is estimated from the local characteristic GRB γ-ray energy $2 \cdot 10^{53}$ erg multiplied by the local GRB rate 0.5 $\text{Mpc}^{-3}\ \text{yr}^{-1}$ to be $(\epsilon_p^2 d\dot{n}_p/d\epsilon_p)_{z=0} = 0.8 \cdot 10^{44}$ erg/Mpc^3 yr.

The maximum muon neutrino intensity obtained from the UHECR spectrum

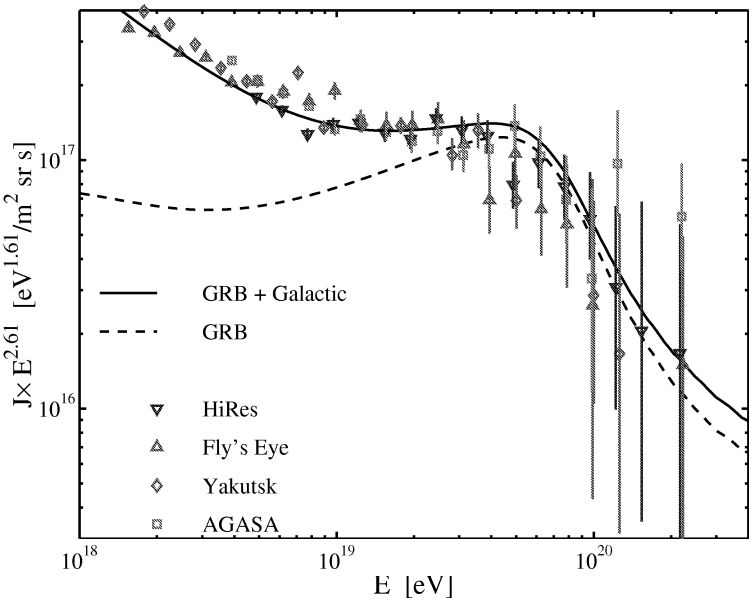

Figure 5.7: *The UHECR flux expected in a cosmological model where high-energy protons are produced at a rate of* $(\epsilon_p^2 d\dot{n}_p/d\epsilon_p)_{z=0} = 0.8 \cdot 10^{44} erg/Mpc^3 yr$ *as predicted in Waxman's GRB model compared to Fly's Eye, AGASA and Yakutsk data. The solid line is the sum of the GRB model flux (dashed line) and the Fly's Eye fit to the galactic heavy nuclei component (from [65]).*

assuming photomeson production of pions and subsequent decay in neutrinos is

$$I_{max} \approx \frac{1}{4} t_H \frac{c}{4\pi} E_{CR}^2 \frac{d\dot{N}_{CR}}{dE_{CR}} \approx 1.5 \cdot 10^{-8} \quad \text{GeV cm}^{-2}\ \text{s}^{-1}\ \text{sr}^{-1}, \tag{5.17}$$

which is precisely the Waxman&Bahcall upper bound for neutrino fluxes. From this equation the GRB neutrino flux is derived by introducing the factor f_π, the realistic fraction of proton energy lost to pion production (see Eq. 5.14). Thus, the GRB neutrino intensity becomes

$$E^2\Phi_{\nu_\mu} \approx E^2\Phi_{\bar{\nu}_\mu} \approx E^2\Phi_{\nu_e} \approx \frac{1}{2} f_\pi I_{max} \approx 1.5 \cdot 10^{-9} \quad \text{GeV cm}^{-2}\ \text{s}^{-1}\ \text{sr}^{-1} \tag{5.18}$$

in the energy range between $10^{14} - 10^{16}$ eV.

If the neutrino spectra in Fig. 5.6 are compared, the agreement between the W&B-flux and the average BATSE-flux is quite good in general. Given the fact that the W&B-flux is normalised to the generation rate of cosmic rays, it is not astounding to find the average flux in model 2 lower than the plateau region of the W&B-flux

by a factor of 0.6. The low-energy shape of the average fluxes is shallower than the W&B-flux, which may reflect the high variation in the spectral coefficients of the bursts. If a burst with a high flux happens to have a more shallow slope than the average slope, then this slope will dominate the shape of the average flux in models 1 and 2, whereas the W&B-flux uses the average spectral coefficient of the bursts. Another reason may be that different energy ranges are dominated by different kinds of bursts. For instance, fast-rising bursts with steep spectra in the low-energy region will reach the plateau region and yield high fluxes there, thus dominating the high-energy region. In contrast, bursts featuring a shallow spectrum in the low-energy region will have lower intensity in the high-energy region but dominate at lower energies.

The high-energy cutoff of the spectrum in model 2 is in very good agreement with the W&B-flux. Model 1 is different because a few individual bursts have been greatly overestimated because of fixing $f_\pi = 0.2$. In these cases, including X-ray flashes in particular, the generic model seems to fail.

Consequently, the same bursts used to calculate the average flux above were subdivided into different classes: long bursts, short bursts and X-ray flashes in order to find out the characteristics of their neutrino spectra. The results are compiled in Figure 5.8.

In general, long duration bursts exhibit much higher neutrino fluxes than short bursts, which is not particularly astonishing given the fact that the corresponding γ-ray fluence is also higher (see Figure 5.4) since more photons can be emitted during a considerably longer period of time. Thus, not being pulled down by the low fluxes of the short burst, the average long burst muon-neutrino flux is even more similar to the W&B-flux than the overall average muon-neutrino flux in Figure 5.6. The difference at the peak of the average long-burst neutrino flux has shrunk to 30% for both muon-neutrinos and electron neutrinos when compared to the W&B-flux.

It is usual to attribute the differences between long- and short-duration bursts to different types of progenitor candidates. The leading model for long-duration GRBs is the collapsar model (see introduction to chapter 5), whereas short-duration bursts have been associated with the merger scenario. So far, due to technical limitations related to the very short duration of the bursts, only the first hypothesis has been supported by observations. But theoretical estimates [66] suggest that binary neutron star or black hole mergers will lead to shorter bursts below 5 s.

As anticipated, the X-ray flash candidates show very low fluxes due to fact that their peak photon energy is below 40 keV. Accordingly, the proton energies have to be extremely high to provide the threshold energy needed for pion production. Consequently, the expected neutrino spectra from X-ray flashes are very low and

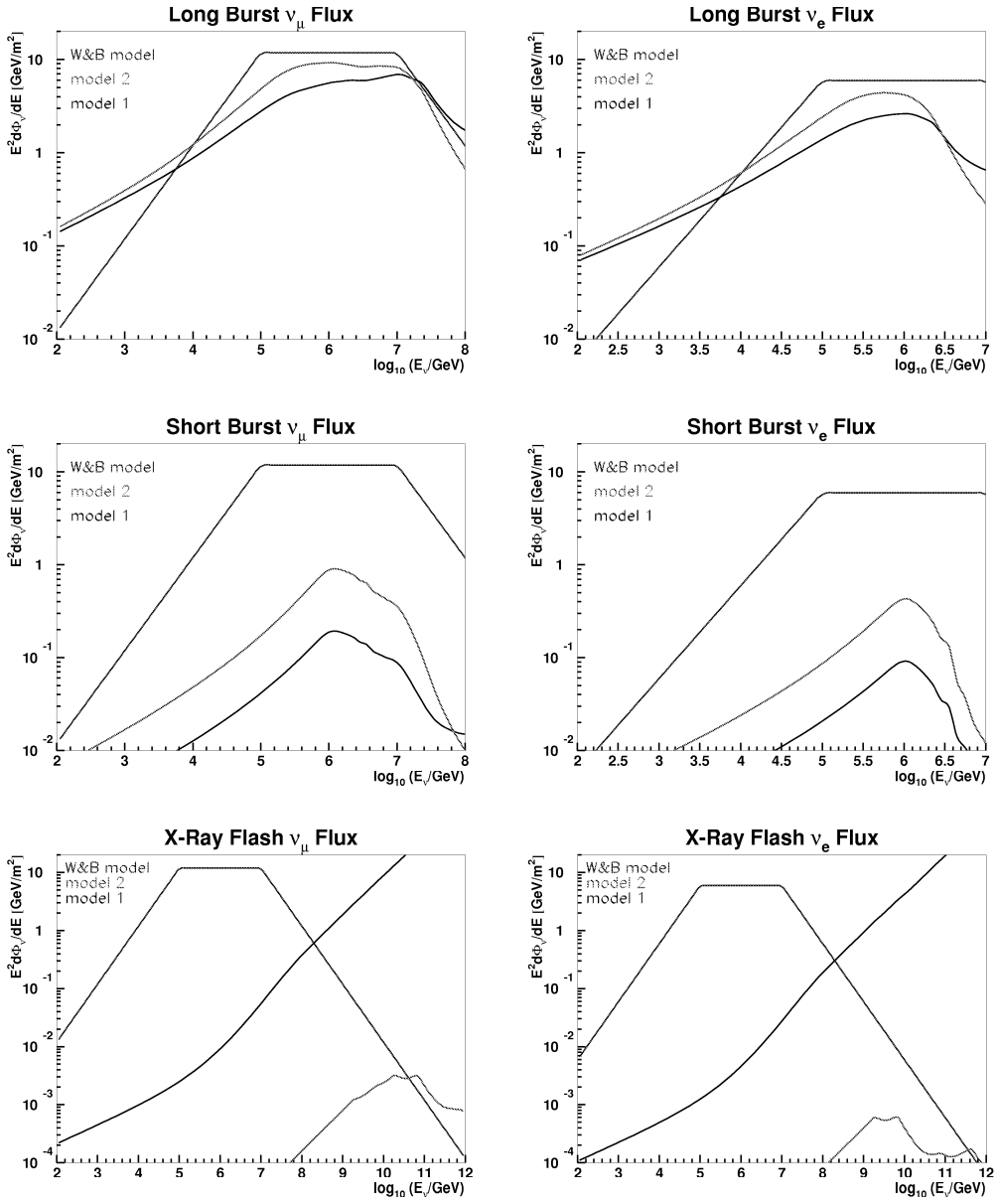

Figure 5.8: *E^2-weighted flux of muon neutrinos $\nu_\mu + \bar{\nu}_\mu$ and electron neutrinos ν_e for long-duration bursts (upper), short-duration bursts (middle) and X-ray flashes (lower) according to the specified models.*

shifted to energies well in the EeV range. The generic model of GRBs assuming $f_\pi = 0.2$ does not seem to be applicable to X-ray flashes because it gives fluxes far too high by several orders of magnitude, as can be seen in comparison with model 2, which takes into account the low luminosity of these objects.

6 ANTARES sensitivity to gamma-ray bursts

In the following, the so-called "hindsight method" for the identification of GRB-neutrinos with the ANTARES detector is presented, which uses multi-messenger information from gamma-ray satellites together with ANTARES data previously collected in normal sampling mode. Sensitivity calculations of the ANTARES detector for GRBs are also presented in two ways: first, by evaluating the level of GRB flux required to observe an excess at a given significance level – the discovery potential –, and by determining the limits that would be placed on GRB neutrino emission models if no events were observed above the background – the limit-setting potential.

6.1 The hindsight method

The hindsight search for neutrinos from past GRBs involves only stored ANTARES data, taken with the usual data filter, together with stored satellite data on GRBs from various catalogues. The latter need not be confined to telescopes on satellites but may also be derived from ground-based γ-telescopes as well if they happen to detect a GRB in their field of view.

Since the ANTARES data analysis would be carried out long after the GRB in question had occurred, there might be the advantage of using very precise astronomical data, in which the burst coordinates would be fully analysed and in many cases even improved by later observations of the afterglow with optical ground-based telescopes of high resolution. Thus, a retrospective study of GRB-neutrinos, similar to the detection method of the SN1987A-neutrinos with Kamiokande [67] and IMB [68], should be envisaged in ANTARES as well.

Moreover, in a study done a posteriori, source-stacking methods can be applied additionally. Source stacking is widely used in astronomy when the sources envisaged are just below the sensitivity of the instrument. Since the detection rate per individual GRB is very low due to the cosmic distances involved, which entail low fluxes, it is wise to do a combined analysis for several GRBs in order to increase

the expected rate of neutrinos. Nevertheless, in the case of a detection it is still possible to attribute the detected neutrino(s) unambiguously to an individual GRB.

The hindsight method of GRB-neutrino detection is intended to be complementary to the existing efforts aimed at the installation of the GCN and IBAS alert mechanism and the subsequent use of the flash-back filter [69], which are online methods. In contrast, the hindsight study is off-line because it relies purely on stored data and hence is completely parasitic. There is no interference with the standard data-taking mode.

In the following, a short outline of the *hindsight method* is presented. The beginning of the study comprises a GRB catalogue, from which the data on individual GRBs can be extracted, such as the coordinates of the burst, its starting time and duration. With this information available, we can examine the stored ANTARES data taken during the burst interval using the standard data filter. The time window of the burst should be extended by a generous safety margin, which makes it possible to capture the neutrinos arriving before and after the prompt gamma-rays. This could be important because there are theoretical considerations in favour of pre-burst neutrinos, which are thought to be decoupled from the fireball faster than photons, to which the plasma appears more opaque. This could be the case when, for example, the fireball expands through the opaque ejecta of a supernova.

Subsequently, the reconstruction of all events within the given time window can be carried out. This has to take into account the precise environmental conditions at the time of the burst (i.e. baseline rate, burst rate, position and alignment of the OMs, etc.) which are stored in the database. It could also be beneficial to use special reconstruction procedures for GRBs rather than the standard all-purpose reconstruction. A reconstruction algorithm written especially for GRBs can take advantage of the known direction of the event and employ this additional information to increase the reconstruction efficiency for GRBs. Following the quality cuts, we are left with a sample of well-reconstructed neutrino candidates, from which we can single out those neutrinos which are within the predefined search cone for the GRB. The centre of the search cone is determined by the catalogue coordinates of the GRB and its radius corresponds to the resolution of the ANTARES telescope.

Since the expected neutrino rates for an individual GRB are so low, it is wise to repeat the analysis for all the GRB-entries in the catalogue which are in the field of view of ANTARES. The sum of all the neutrino events over the analysed GRBs will constitute the source-stacking part of the method.

6.2 Expected GRB-neutrino event rates in ANTARES and KM3NeT

Important parameters for neutrino detection from GRBs and other point sources are the angular resolution and the effective area of the telescope.

The angular resolution improves greatly with increasing neutrino energy since both the direction of the muon can be reconstructed better and the muon direction is more strongly aligned with the direction of the incident neutrino due to the increasing Lorentz boost. Hence, the angular resolution of ANTARES is below 0.3° in the high-energy region relevant to GRB neutrino detection. This is a key parameter important for constraining the radius of the search cone so that the signal to background ratio can be maximised.

In order to convert the ν-fluxes into event rates $\dot{N}_\nu$, the effective area A_{eff} of the detector has to be known (see Chapter 3.3 and Equ. 3.10).

Unlike the geometric area of the detector, the effective area represents the area which is seen by the neutrinos prior to entering the Earth, and is therefore dependent on the energy and zenith angle of the incident neutrinos. Especially at high energies dependence on the direction becomes more pronounced since there is an increasing probability $P_{Earth}(E_\nu, \theta_\nu)$ of a neutrino interaction inside the Earth for vertical directions compared to horizontal ones, where the amount of traversed matter is smaller (see Fig. 3.15 upper).

Moreover, the effective area of ANTARES also depends on environmental parameters such as the baseline and burst rates. This effect does not involve any neutrino physics but is rather an artefact of reconstruction efficiency since the reconstruction algorithms detract from purity when the number of fake hits increases. As a result, the effective area of the detector diminishes (see Fig. 3.15 lower).

The anticipated rate of neutrinos in ANTARES for an average GRB is shown in Fig. 6.1. The peak differential rate of muon-neutrinos is expected around 0.25 PeV in both flux models regardless of the baseline rate. Additionally, the expected rate of electron-neutrinos is also shown. This calculation uses the ANTARES effective area for electron-neutrinos obtained by the Shower Strategy [70] which is intrinsically smaller than the effective area for muons due to the properties of the induced electromagnetic cascades. Furthermore, it is noteworthy that 90% of the GRB-neutrinos are expected at energies higher than about 16 TeV. This value is entirely model-independent, thus making it possible to perform further energy cuts on the neutrino events and leveraging the GRB-neutrino signal even more clearly above the background of atmospheric neutrinos.

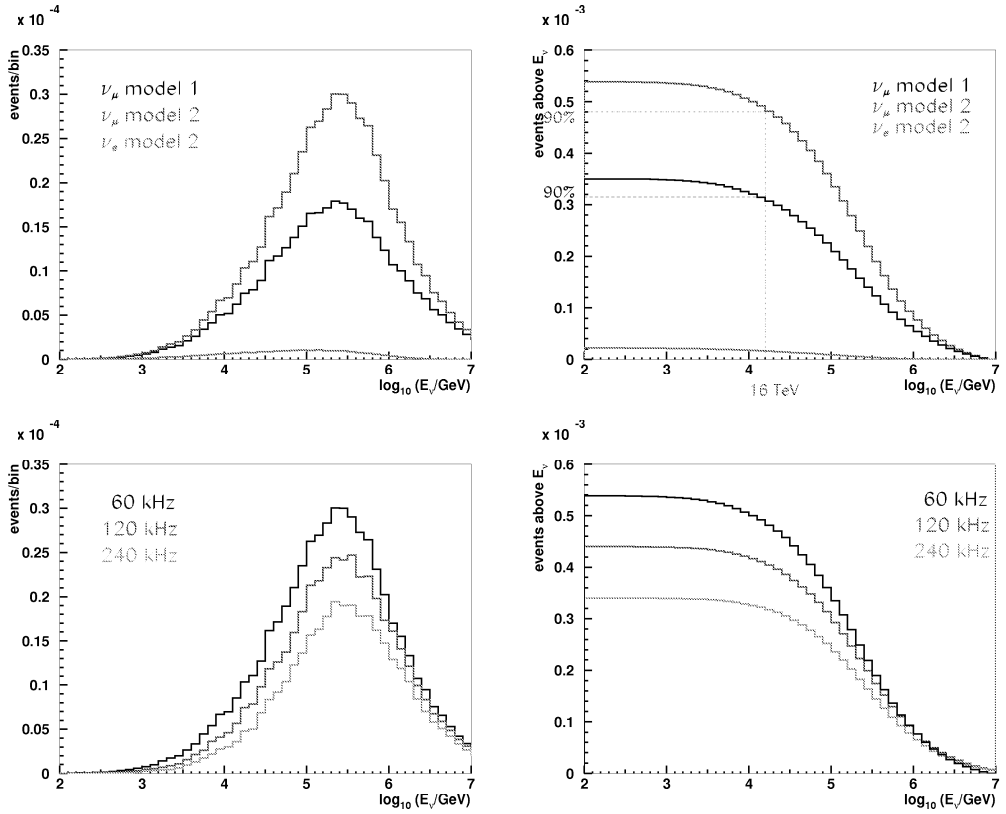

Figure 6.1: *Left: Differential event rates in ANTARES as a function of the energy bin. Right: Integrated event rates in ANTARES. The upper graphs show the results for models 1 and 2 at 60 kHz baseline rate while the lower plots illustrate the results of model 2 for different baselines.*

In addition to the expected rates in the ANTARES telescope, rates have also been estimated for the intended successor telescope. The KM3NeT project [71] is a joint European scientific enterprise, launched by the ANTARES, NEMO and NESTOR collaborations, whose aim is to construct an ultra-high-energy neutrino telescope of cubic-kilometre scale in the Mediterranean. The ongoing design study has several proposals for the architecture of the future telescope but until the study has been completed the geometry will not be decided on. Thus, the effective area used for estimating neutrino rates is derived from the preferred cube geometry consisting of 22×22 strings in a quadratic arrangement in which the distance between two neighbouring strings is 62.5 m in both directions. The other difference with respect to the ANTARES telescope is the optical modules used in the given simulation: each optical module is equipped with 12 cylindrical 3-inch PMTs, which enables it to yield a better quantum efficiency of about 35%. Two effective areas of the prospective KM3NeT telescope [72] are shown

in Figure 6.2: The lower curve represents the effective area after reconstruction and quality cuts, and hence is the minimal area for the given geometry. Since the reconstruction algorithm has not yet been optimised to fit the KM3NeT geometry but is essentially a modified AartStrategy, it is conceivable that a dedicated reconstruction algorithm will yield a larger area by performing in an optimal way. Therefore, an effective area corresponding to those muon-neutrino events which have generated at least 10 signal hits in the detector is also shown, thus representing the maximal area for the given geometry.

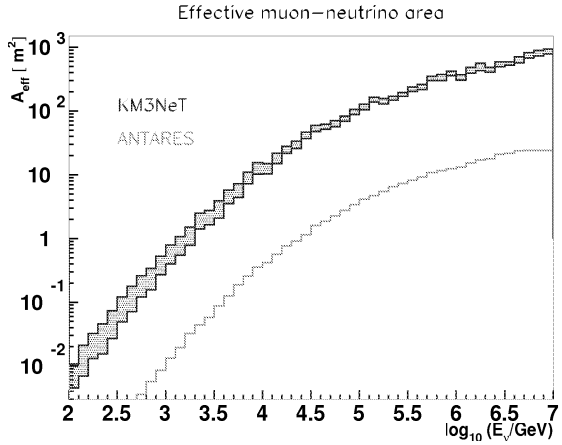

Figure 6.2: *Expected effective area for muon-neutrinos of the KM3NeT telescope at 60 kHz noise rate. The two curves indicate the upper and lower limit to the effective area due to uncertainties in the final design and the unadjusted reconstruction. The ANTARES effective area is shown for purposes of comparison.*

On the basis of the range for the KM3NeT effective area shown above, the detection rate for GRB-neutrinos has been calculated. The results are shown in Figure 6.3. Compared to the ANTARES detector, KM3NeT will probably be able to detect 30 to 40 times more neutrinos from GRBs, provided the currently favoured geometry is created and the GRB neutrino flux is valid. While long-duration burst will certainly be detectable with KM3NeT, and probably also short-duration bursts within several years, neutrinos from X-ray flashes are still out of reach even for KM3NeT.

For both telescopes it is noteworthy that the expected number of events per burst varies considerably, as illustrated in Fig. 6.4, which is not only a result of the dispersion of fluences (as shown in Figure 5.4 right) but is also due to variations in f_π and different zenith angles which involve different effective areas.

To obtain the expected number of neutrinos per year, the values shown in Fig. 6.1 and 6.3 simply have to be multiplied by the number of GRBs which have been

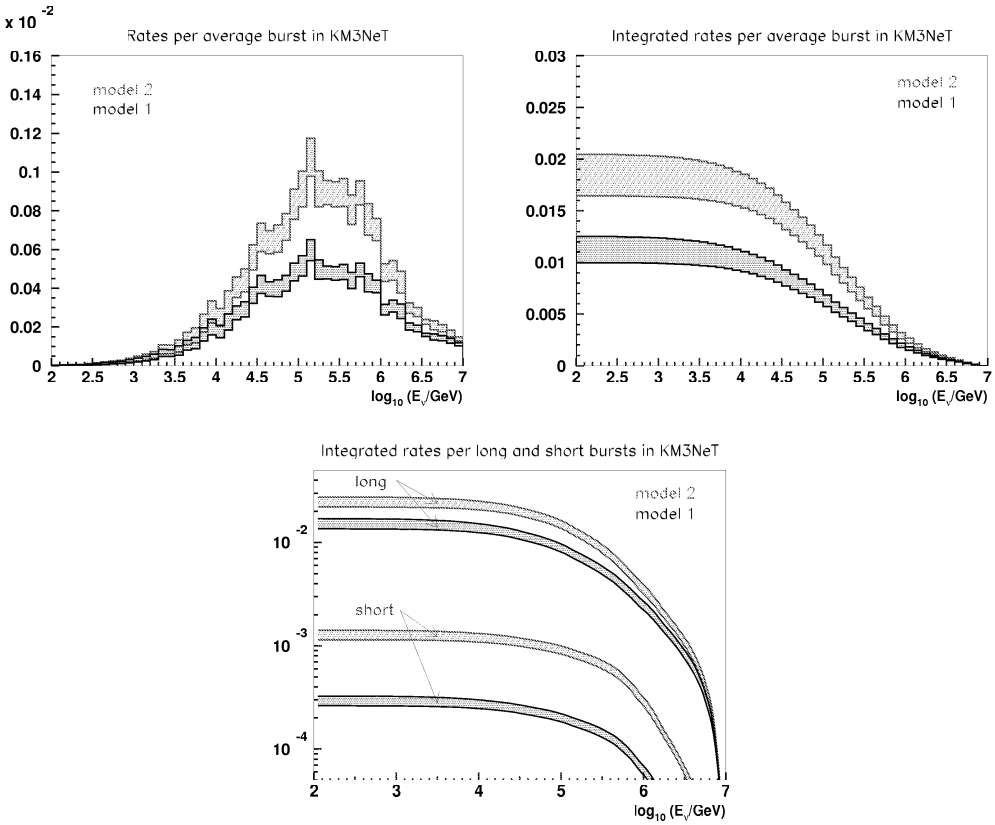

Figure 6.3: *Upper: Differential and integrated event rates per average GRB in KM3NeT. Lower: Integrated event rates per average long and short burst in KM3NeT. The shaded areas indicate the possible values for event rates in KM3NeT due to the uncertainties in the predicted effective area of the future telescope.*

detected by gamma satellites during the same time period. The detection rate of GRB observatories in orbit is difficult to estimate because it depends on their field of view and effective area. For the purpose of comparison, Table 6.1 summarises key performance parameters of BATSE and some current and future gamma-ray experiments.

The total rate at which GRBs occur has to be estimated from the BATSE observations. BATSE's detection rate has been approximately 300 bursts per year. Its field of view was limited by Earth occultation only, which is equivalent to 68% full-sky coverage at the CGRO altitude. If this geometric shielding is taken into account, the overall GRB detection efficiency of BATSE amounted to 33%, which implies that GRBs occur at a rate of about 1000 per year in 4π steradian.

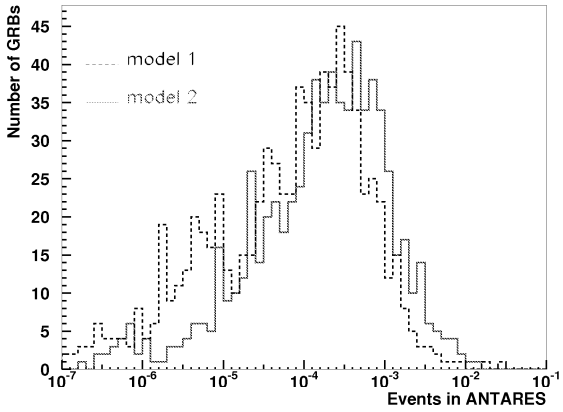

Figure 6.4: *Distribution of the estimated number of muon neutrino events from individual GRBs in ANTARES.*

Table 6.1: *Parameters of past, present and future gamma-ray observatories in orbit [60], [73], [74], [75], [76], [77].*

Parameter	BATSE	HETE2	INTEGRAL	SWIFT	AGILE	GLAST
Launch	1991-2000	Oct. 2000	Oct. 2002	Nov. 2004	2007-8 ?	Sept. 2007
Source position	1°	$1' - 10'$	$\leq 1' - 1.5'$	$1'' - 4''$	$2' - 3'$	$30'' - 5'$
Field of View (sr)	8.5	4	0.95	1.4	2.5	> 2
Effective area (cm^2)	8×2025	160	500	5240	550	8000
Energy range (MeV)	0.03-1.9	0.002-0.4	0.004-10	0.015-0.15	30-50000	20-30000
Energy resolution (%)	20-32	9-25	0.16	5-47	9-27	10
Detected bursts (yr^{-1})	~ 300	~ 50	6-24	> 100	~ 20	~ 100

6.3 Background studies

Different types of background are known to occur at neutrino telescopes. The location of the telescopes ANTARES and KM3NeT in the Mediterranean is responsible for a relatively high optical background noise as compared to other neutrino telescopes due to radioactive decay of ^{40}K and bioluminescent organisms (see section 2.4). However, the optical background is dealt with in the reconstruction strategy and is thus already incorporated in the effective areas (shown in Fig. 3.15) used to compute the event rates in Fig. 6.1 and 6.3.

Besides the noise, there is also an important and irreducible background of atmospheric neutrinos and muons resulting from cosmic ray interactions in the atmosphere. Since neutrino telescopes are designed to detect these very particles, the atmospheric background cannot be disposed of easily except through the application of various cuts on the reconstructed events. In the following,

atmospheric neutrinos and muons are regarded as background to a GRB signal.

The differential spectra of atmospheric muon neutrinos from pion, kaon, and muon decays at sea level can be analytically approximated by Eq. 1.1 as derived by [6]. Similarly, the electron neutrino spectra from muon and kaon decay can be parametrised according to Eq. 1.2. The accuracy of these formulae is about 5% in shape, but the absolute magnitude is more uncertain. It is also apparent that electron neutrinos are suppressed by nearly two orders of magnitude compared to muon neutrinos because, at the high energies involved, all the decay channels which would produce ν_e via muon decay make only a small contribution since the lifetime of the muons is relativistically prolonged, allowing them to reach the sea level before decaying.

For multi-messenger GRB observations, however, the time and angular windows are so narrow that the expected background events from the above-mentioned spectra are reduced further. The ability of the ANTARES detector to reconstruct muon-neutrino tracks to within 0.5° of their true direction makes it possible to use a search window of similar size, which greatly reduces the background while retaining a large proportion of the signal. The same methods hold for the time window of a GRB including the short bursts. Considering, for instance, a search cone with an opening solid angle of 0.5° and 100 s for a long-duration burst (0.1 s for short duration bursts) to be on the safe side, the atmospheric muon-neutrino flux shrinks by 10 (13 for short bursts) orders of magnitude (see Fig. 6.5 left). In the case of electron neutrinos, the angular resolution is around 10 degrees, which necessitates a widening of the angular window.

Normally, this has to be calculated individually for each burst, taking into account the precise burst duration, the uncertainty in the position reconstruction and the background neutrino flux corresponding to the zenith angle of the GRB. Since the burst-to-burst variations with respect to background suppression are minor within the same GRB subclass, Fig. 6.5 presents the signal and background fluxes for different GRB subclasses instead of individual bursts. The atmospheric neutrino background shown here also includes the contribution from the prompt component, as can be seen in Fig. 6.5 upper right, where a slight kink in the horizontal atmospheric ν_e-flux is visible at 370 TeV. As is evident from the energy dependence of the fluxes, energy cuts (with varying amounts of threshold energy for the different subclasses) can significantly improve the signal-to-noise ratio by eliminating most of the low-energy background neutrinos.

In addition to the atmospheric neutrinos atmospheric muons also constitute a source of background for GRB observation. Even in the case of GRB-observation restricted to directions below the horizon atmospheric muons can contaminate the measurement if directional reconstruction fails and an atmospheric muon is reconstructed into the GRB search cone. Similarly to the atmospheric neutrinos, cuts on the energy and zenith angle of the reconstructed events will considerably

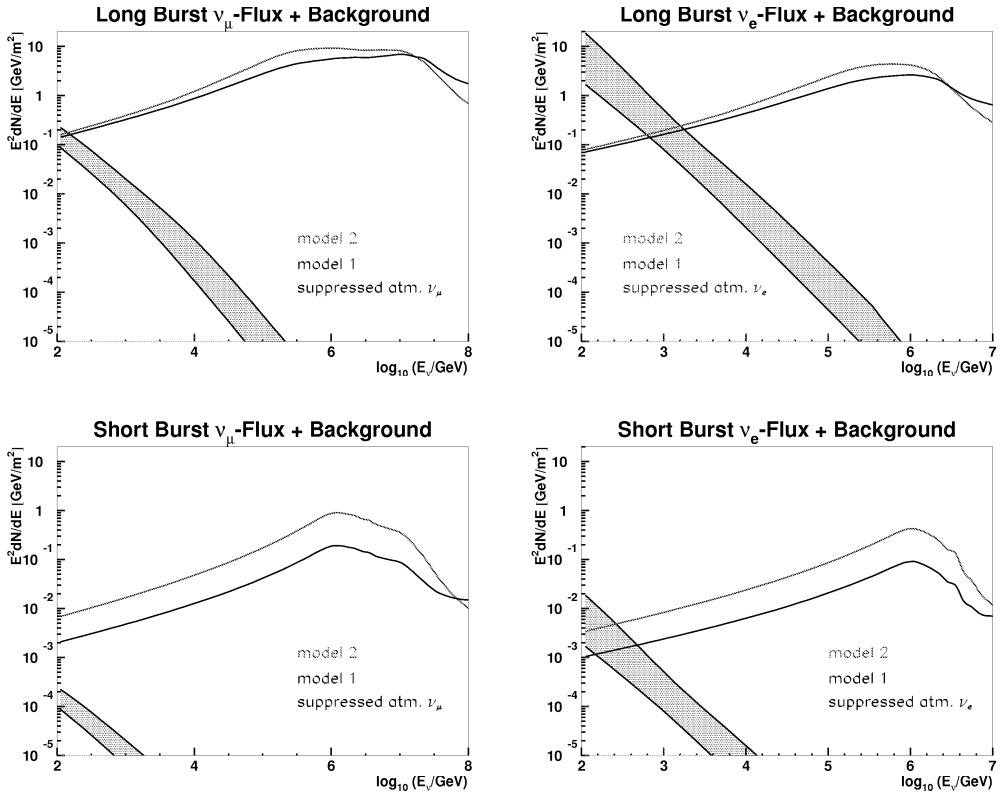

Figure 6.5: *E^2-weighted average flux of GRB neutrinos and atmospheric neutrinos (shaded bands) for a time window of 100 s for long bursts (upper) and 0.1 s for short bursts (lower). An angular search cone with opening angle 0.5° is assumed for muons (left) and 10° respectively for electrons (right).*

enhance the signal to background ratio. Figure 6.6 shows the expected differential rate of signal events together with background events from atmospheric neutrinos and muons as a function of energy for different zenith angle bins. The rates for the signal and atmospheric neutrinos have been calculated analytically by assuming model 2 for the GRB neutrino flux and the predicted Volkova-flux for the median of the angular bin. For each zenith angle the corresponding effective area (see Fig. 3.15) has been used to compute the rates. The lack of smoothness visible in the calculated rates is a numerical artefact resulting from the interpolation of the effective areas.

The atmospheric muons are extracted from a `CORSIKA` simulation [38], which is reconstructed with the very same strategy as that employed for the signal neutrinos, and their rates weighted in such a way as to correspond to a time interval of 100 s and a search cone with a 0.5° opening angle – just like the

atmospheric neutrinos.

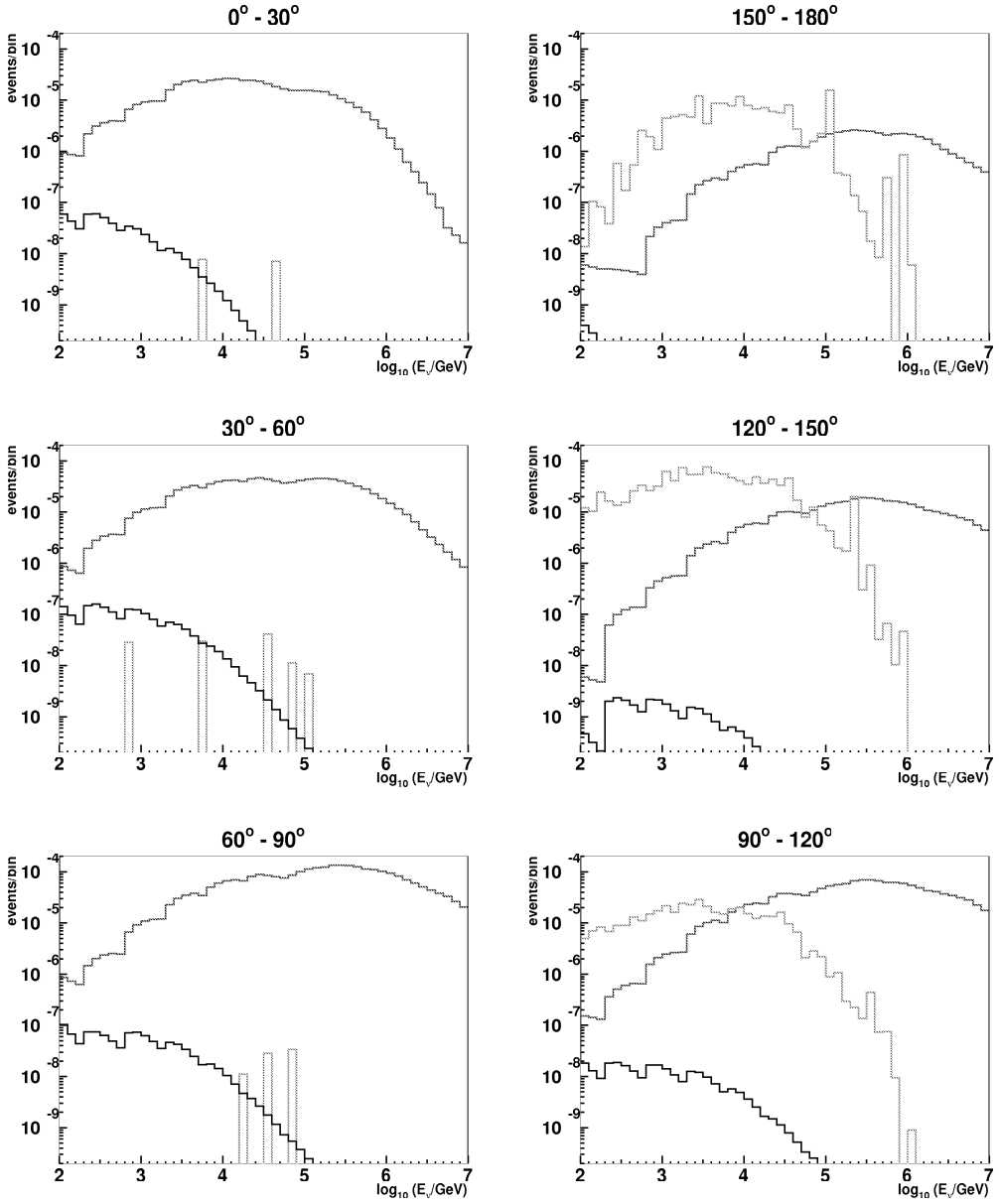

Figure 6.6: *Differential rate of muon neutrino events arising from the GRB-signal (red), the atmospheric neutrinos (black) and the atmospheric muons (green) for the indicated angular bins.*

It becomes evident from Fig 6.6 that multi-messenger GRB observations below the horizon are essentially background-free due to its suppression by the coincidence condition. Although the statistics on atmospheric muons are very sparse,

the rate of falsely reconstructed atmospheric muons seems to be comparable to the rate of atmospheric neutrinos if an energy cut around 10 TeV is envisaged. By contrast, the situation above the horizon is worse, as the muon flux dominates well into the TeV energy region. Therefore, the most obvious strategy is to restrict all observations to directions from below the horizon by cutting on the zenith angle of the reconstructed events. Alternatively, it may be worthwhile to look upwards as well, provided the energy of the reconstructed event exceeds a certain threshold. For instance, the threshold energy could be set between 100 TeV and 1 PeV for downward-going events in terms of GRB signal-to-background ratio.

The feasibility of an energy cut is a crucial point given the poor energy resolution of neutrino telescopes in general. Since the energy reconstruction is based on the amount of deposited light in the detector and the muon ranges exceed the detector length in most cases except the very low-energy ones, muon energy reconstruction is intrinsically limited. However, the upper TeV region is well-suited for energy cuts since the muon has already past the transition phase, in which it changes from a minimally ionising particle to a more actively interacting particle, whose energy loss is dominated by stochastic processes such as pair production, from which electromagnetic showers will emerge. Figure 6.7 exemplifies the possibility of an energy cut at 10 TeV. The real energy of the neutrinos is shown in black, the reconstructed energy in blue. After a cut on the reconstructed energy the red events survive and are displayed according to their real energy to illustrate the accuracy of the applied cut. While there are still a few events with real energies below 10 TeV, the majority of the remaining events satisfy the criterion.

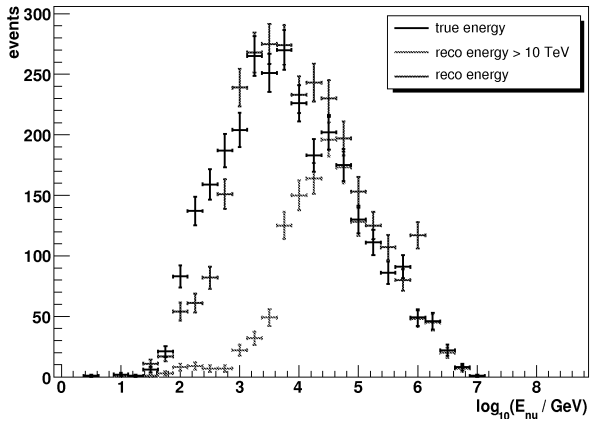

Figure 6.7: *Energy cut on the reconstructed energy at 10 TeV. [78]*

The results from Figure 6.6 are summarised in Table 6.2. Here, the energy threshold was set to 10 TeV for events below the horizon, which is very close to the energy value above which 90% of the total muon neutrino flux is expected, and

100 TeV for events above the horizon.

Table 6.2: *Expected rates in ANTARES for GRB-neutrinos (per average burst model 2), atmospheric neutrinos and atmospheric muons (both 100 s, 0.5°) after the indicated energy cut:*

energy cut	nadir angle	atm ν	atm μ	sum bkg	GRB-ν
$E > 10$ TeV	$0° - 30°$	$0.33 \cdot 10^{-8}$	$0.72 \cdot 10^{-8}$	$1.05 \cdot 10^{-8}$	$0.31 \cdot 10^{-3}$
	$30° - 60°$	$4.30 \cdot 10^{-8}$	$5.95 \cdot 10^{-8}$	$10.2 \cdot 10^{-8}$	$0.83 \cdot 10^{-3}$
	$60° - 90°$	$3.39 \cdot 10^{-8}$	$7.40 \cdot 10^{-8}$	$10.8 \cdot 10^{-8}$	$2.53 \cdot 10^{-3}$
$E > 100$ TeV	$90° - 120°$	$3.25 \cdot 10^{-10}$	$0.32 \cdot 10^{-5}$	$0.32 \cdot 10^{-5}$	$0.98 \cdot 10^{-3}$
	$120° - 150°$	$0.35 \cdot 10^{-10}$	$2.94 \cdot 10^{-5}$	$2.94 \cdot 10^{-5}$	$0.26 \cdot 10^{-3}$
	$150° - 180°$	$0.04 \cdot 10^{-10}$	$1.78 \cdot 10^{-5}$	$1.78 \cdot 10^{-5}$	$0.03 \cdot 10^{-3}$

6.4 Discovery potential

In general, a phenomenon is considered to be "discovered" when a measurement yields a 5σ excess over background, thus implying that the probability of the observation caused by an upward fluctuation of background is lower than $2.85 \cdot 10^{-7}$, which is the integral of the one-sided tail beyond 5σ of a normalised Gaussian.

Since the ANTARES telescope is on the verge of observing a GRB-neutrino, it may be large enough to detect GRB-neutrino(s) but it is unlikely to reach the required 5σ significance level. In order to obtain a signal event, ANTARES will have to measure GRBs in the coincidence mode with γ-satellites for several years.

However, the flavour composition of the neutrino flux on Earth will differ from the one at the source due to neutrino oscillations. The neutrino vacuum oscillations over cosmological distances will alter the initial $\nu_e : \nu_\mu : \nu_\tau = 1 : 2 : 0$ composition to $1 : 1 : 1$, provided all neutrino flavours share the same energy spectrum. This is largely the case, since for a particular burst the ν_μ- and ν_e-spectra are identical until affected by the muon synchrotron energy, which leads to a cut-off of the ν_e and $\bar{\nu}_\mu$-spectra (see Fig. 5.5). This deviation usually occurs at very high energies in the PeV region and a decade in energy below the cut-off of the ν_μ-spectrum itself. Therefore, it seems justifiable to assume that the GRB-neutrino flavours have similar spectra and thus the ν_μ-flux component on Earth will amount to roughly 50% of the original flux. Thus, dividing the expected detection rate for GRB-neutrino observation below the horizon by two (see Table 6.2) the required

observation period for ANTARES to detect a GRB-neutrino would amount to about 4 years.

Moreover, given the fact that satellites in orbit do not have full sky coverage and hence detect only a fraction of the total numbers of GRBs, the measurement period required by ANTARES to detect its first GRB-neutrino may well extend to about 5 years. In this example, the background expectation value will amount to $N_b = 1.8 \cdot 10^{-4}$, given the fact that atmospheric neutrinos in this energy range do not suffer from oscillations. Thus the significance obtained by measuring a neutrino in coincidence mode is

$$P(N_{obs}|N_b) = 0.999816,$$

where P is the Poisson probability of observing one background event at the given background expectation value N_b. In this particular example, the significance level of the measurement would be 3.7 σ.

Other observation modes, including GRB-neutrino detection above the horizon, are also conceivable, as is shown by Table 6.2: for instance, the GRB signal rates are highest in the $0° - 120°$ nadir angle bins although the energy cut for events above the horizon is much more stringent. Restricting GRB observations to these zenith angles would increase the probability of detecting a GRB-neutrino earlier (4 years) at the expense of significance (3.0 σ).

6.5 Limit-setting potential

Feldman and Cousins [79] proposed a method for quantifying the sensitivity of an experiment by calculating the average upper limit which would be obtained in the absence of a signal. This method is particularly well-suited for Poisson processes with background and Gaussian errors with a limited physical region. The average upper limit is calculated from the mean number of expected background events N_b by averaging out all the limits obtained from all possible experimental outcomes. In the case of ANTARES GRB-neutrino observation below the horizon, using the coincidence condition mentioned above, the mean number of expected background events amounts to $N_b = 1.07 \cdot 10^{-4}$ for a 5-year measurement period.

The average upper limit is the maximum number of events which can be excluded at a given confidence level. Thus, the ANTARES experiment can be expected to constrain any hypothetical GRB neutrino flux which generates at least 2.43 signal events during a measurement period of 5 years at 90% confidence level.

The flux limit derived from this number depends on the shape of the assumed flux. In the case of the average flux (see Fig. 5.6 and Fig. 6.8) the ANTARES

limit at 90% confidence level for an observation period of 5 years is expected to be

$$E^2\Phi_{90\%} < 3.8 \cdot 10^{-9} \quad \text{GeV cm}^{-2}\ \text{s}^{-1}\ \text{sr}^{-1}.$$

The Amanda collaboration was also investigating GRB-neutrino detection in coincidence with the BATSE satellite during their common measurement period between 1997 and May 2000. To increase their search exposure, they examined BATSE bursts that were revealed off-line by additional analysis (termed "non-triggered" bursts) and GRBs identified by the Interplanetary Network (IPN) of satellites. The result was clear, neither AMANDA-B10 nor AMANDA-II observed correlated emission of high-energy neutrinos from any burst sample. The limit derived from this for GRBs assuming a broken power law spectral form is:

$$E^2\Phi < 4 \cdot 10^{-8} \quad \text{GeV cm}^{-2}\ \text{s}^{-1}\ \text{sr}^{-1}.$$

The AMANDA GRB limit is a factor of 10 above the predicted ANTARES limit, which is perfectly understandable given the better angular resolution of ANTARES of 0.5° compared to approximately 2° of AMANDA-II, and the longer observation period of 5 years compared to $3 - 3.5$ years for AMANDA.

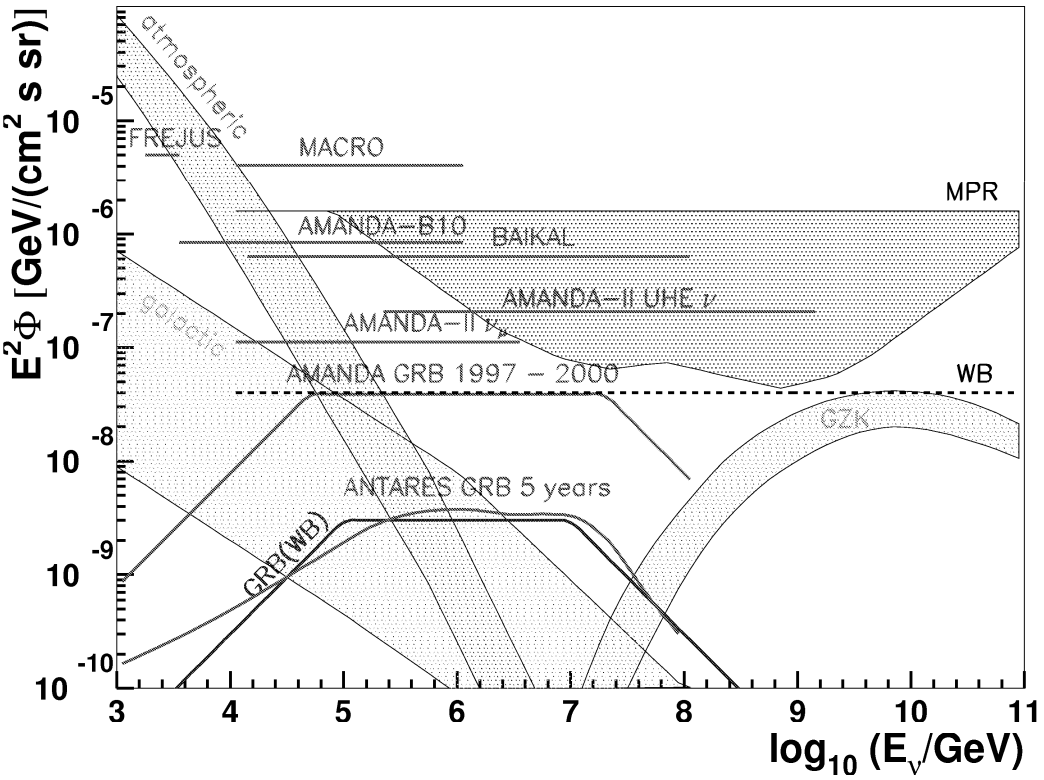

Figure 6.8: *Limit which could be set by ANTARES on the GRB-$\nu_\mu + \bar{\nu}_\mu$ flux after a measurement period of 5 years compared to other experimental upper limits for GRBs.*

7 Conclusions and Outlook

Studies on the neutrino emission from individual GRBs recorded by BATSE have been conducted to estimate the rate of muon (and electron) neutrinos observable with the ANTARES telescope.

The neutrino flux calculations were done within the framework of the fireball model with internal shocks, as proposed by Waxman and Bahcall. The individual fluxes are then summarised to give an average GRB neutrino flux, which is converted into neutrino rates for the ANTARES and the prospective KM3NeT telescopes by using the effective areas obtained with the modified reconstruction strategy for high optical background and an effective area "band" for the currently favoured KM3NeT design. The major background of atmospheric neutrinos and falsely reconstructed atmospheric muons is also estimated, taking into account its suppression by the narrow time and angular windows set by multi-messenger observations in coincidence mode with γ-satellites.

In conclusion, it can be asserted that even in standard data-taking mode using the common data filter it will be possible to detect GRB neutrinos with ANTARES employing the hindsight method. It is anticipated that the analysis will be performed retrospectively by means of investigation into both the stored ANTARES data and various catalogues of GRB observatories in orbit. This will make it possible to combine both sets of information, which will make the observation of neutrinos from GRBs in coincidence with satellite measurements virtually free of background. Hence, even one neutrino would be significant. In other words, the hindsight method appears to be suited for GRB-neutrino detection.

Summa summarum, ANTARES, and certainly its successor KM3NeT, will have the potential for detecting neutrinos from GRBs by taking advantage of the multi-messenger observations and thus leveraging the GRB-neutrino signal more clearly above the otherwise irreducible background of atmospheric neutrinos and muons. Such a measurement of a single GRB-neutrino would already constitute a benchmark observation, since it would confirm the hypothesis of hadrons being accelerated to at least the measured energy in the observed GRB. Since the acceleration mechanism of cosmic rays to the highest observed energies of $3 \cdot 10^{20}$ eV is still unsubstantiated, and GRBs are among the best known candidate sources with regard to the provision of sufficiently strong magnetic fields in a very compact space, being able, in principle, to accelerate protons up to

10^{20} eV, neutrino measurements could provide direct evidence for the resolution of this open question. Moreover, cubic-kilometre scale neutrino telescopes with increased sensitivity would also be able to measure neutrinos from all subclasses of GRBs such as long and short duration bursts and maybe even X-ray flashes, and by arrival-time comparison to the GRB-photons determine important parameters of the GRB such as its opacity. However, there are still some drawbacks that must not be ignored: even the next-generation neutrino telescopes such as IceCube and KM3NeT will not be capable of measuring a complete neutrino spectrum or a neutrino "lightcurve", or of deriving a neutrino "luminosity" from an individual burst because they will never detect more than a handful of neutrinos from a particular GRB. This could occur only in a very fortunate (?) case if a GRB happened to be observed in our immediate proximity. Therefore, precision measurements necessary for an understanding of the exact nature of GRBs and for discrimination between different theoretical GRB models are unlikely to be carried out successfully even with the next generation of neutrino telescopes.[1]

[1] One might contemplate the possibility of investigating these GRB models by measuring very precisely the TeV-γ-ray counterparts from π^0 decays of the accelerated hadrons. This is only possible if the TeV-photons can decouple from the GRB fireball in the first place, the GRB is close enough to be within the gamma-horizon, and no absorption occurs on the way to Earth.

A Neutrino rates from neutralino annihilation in the Sun

There are copious manifestations ranging from galactic to cosmological scales which imply the existence of cold dark matter (CDM) in the Universe. The rotational curves of galaxies, including our own, differ significantly from the predictions based on the mass inferred by the amount of luminous matter observed in the galaxies and suggest the existence of a halo. Moreover, the observed temperature in galaxy clusters does not agree with the model calculations of the hydrostatic equation of state. The existence of surplus matter is also confirmed by gravitational lensing, such as the recent observation of two merging clusters in 1E0657-56 [80]. Also on the cosmological scale, the anisotropies in the cosmic microwave background radiation constrain the density of matter and baryons in the Universe. The resulting discrepancy is the CDM density, which has been measured to a very high degree of accuracy as being $0.094 < \Omega h^2 < 0.129$ at 2σ confidence level [21].

Due to the relatively high relic density, CDM is thought to consist of weakly interacting massive particles (WIMPs). Currently, there are several candidate particles thought to explain the nature of the WIMP: the neutralino as the lightest supersymmetric particle, the Kaluza-Klein particles inferred from models with extra-dimensions and axions arising from the attempt to solve the strong CP-problem.

In the following, neutralinos are considered to be the most promising candidates for dark matter and their indirect detection is an important aspect of ANTARES physics goals. Neutralinos are thought to self-annihilate and this process is enhanced in places where neutralinos are abundant due to gravitational capture in massive objects such as the Sun, Earth, Galactic Centre, etc. The annihilation products, usually heavy quark pairs, tau pairs as well as W, Z and H pairs, cascade down in energy and eventually produce neutrinos. The neutrino fluxes from neutralino annihilation in the Sun have been calculated by H. Motz [81] on the basis of DarkSusy and taking into account neutrino oscillations, resonant neutrino oscillations in the Sun and vacuum oscillations during propagation to Earth. From the multitude of fluxes calculated for all relevant parameters of the SUSY parameter space, a few fluxes representative of different regions of the

parameter space have been chosen and termed accordingly: A-resonance, bulk, focuspoint (centre and lower) and h-resonance.

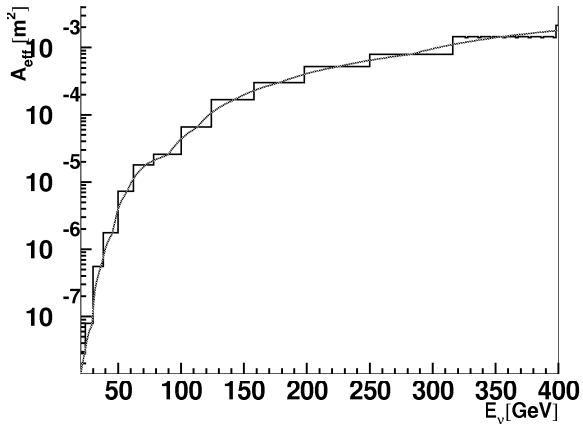

Figure A.1: *ANTARES effective area at the low-energy detection threshold 10 - 400 GeV.*

For these example fluxes, signal and background rates have been estimated for the ANTARES detector. The intention behind this study is not a precision calculation but a crude estimation of the expected event rates for signal and background in order to acquire an idea of the feasibility of the detection of neutrino signals from WIMP annihilation. With this goal and bearing in mind the fact that the reconstruction algorithm has not been adapted to suit these extremely low-energy events close and partly below the ANTARES detection threshold, the reconstruction algorithm presented in Chapter 3 was applied to a sample of 10^8 neutrinos generated in the energy region between $10 - 400$ GeV with a spectrum of E^{-1} and a background noise of 60 kHz. As these low-energy neutrinos are not likely to interact very often and even less likely to produce sufficient hits in the detector to be well reconstructed, the statistics of this study are in general very poor. The effective area obtained is shown in Figure A.1 together with the interpolation used to calculate the rates. For the calculation of the angular resolution the statistics were not sufficient because in this energy region the angular resolution is expected to change very rapidly due to the increase in the neutrino-muon misalignment with decreasing energy. Therefore the parametrised angular resolution from Figure 3.17 has been taken and extrapolated to lower energies, thereby reaching 4.5 degrees at 4 GeV.

This angular resolution has been used to attain an approximate determination of

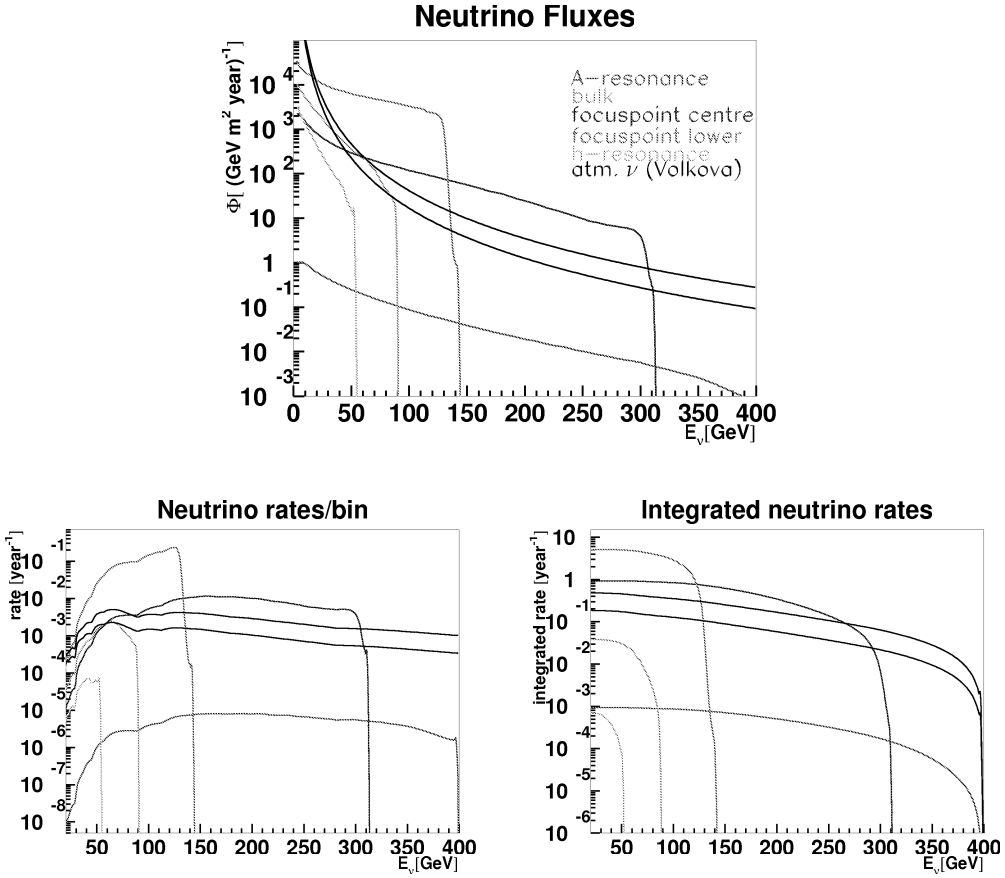

Figure A.2: *Upper: Comparison of muon-neutrino fluxes from neutralino annihilation in the Sun and atmospheric neutrinos. Lower: Expected event rates in ANTARES for neutrinos from neutralino annihilation in the Sun and background rates from atmospheric neutrinos. The colour coding indicated in the upper figure also applies to the lower figures.*

the opening angle of the search cone as a function of energy:

$$\Theta(E_\nu) = \sqrt{\sigma_{Sun}^2 + \sigma_{PSF}(E_\nu))^2}.$$

Here $\sigma_{PSF}(E_\nu))$ is the extrapolated energy resolution of ANTARES and σ_{Sun} the angular size of the Sun. The search window with the opening angle $\Theta(E_\nu)$ and the fact that the Sun is, on average, below the horizon for half of the observation time determine the suppression factor of the atmospheric neutrinos. This suppressed atmospheric neutrino flux is shown in Figure A.2 (top) for horizontal and vertical directions (upper and lower black curve), using the parametrisation provided by Volkova [6] together with the example neutrino fluxes from the various regions of

the SUSY parameter space.

The event rates[1] displayed in the same colour code as the corresponding neutrino fluxes are also shown in Figure A.2 (lower) per energy bin and integrated in such a way that the expected number of neutrinos with energies higher than E_ν is plotted. It is noteworthy that the neutrinos originating from the focuspoint region stand a chance of being detected by ANTARES provided that this region of the parameter space is indeed the one chosen by Nature.

[1] In this calculation, the loss of signal neutrinos due to their arrival outside the search cone is not taken into consideration.

Bibliography

[1] K. Greisen, *End to the cosmic ray spectrum?*, Phys. Rev. Lett. **16**, 748 (1966).

[2] G.T. Zatsepin and V.A. Kuzmin, *Upper limit of the spectrum of cosmic rays.* JETP Lett. **4**, 78 (1966).

[3] M. Walter, *Design and initial performance of the IceCube detector*, 10th Topical Seminar on Innovative Particle and Radiation detectors, Siena (2006).

[4] T. K. Gaisser and M. Honda, *Flux of Atmospheric Neutrinos*, Ann. Rev. Nucl. Part. Sci. **52**, 153 (2002).

[5] The AMANDA collaboration, `http://amanda.uci.edu/results.html`

[6] L. V. Volkova, *Energy spectra and angular distributions of atmospheric neutrinos*, Sov. J. Nucl. Phys. **31**, 1510 (1980).

[7] G. Ingelman and M. Thunman, *Particle Production in the Interstellar Medium.* `hep-ph/9604286`

[8] D. Allard *et al.*, *Cosmogenic Neutrinos from the propagation of Ultra High Energy Nuclei.* `astro-ph/0605327`

[9] N. Kawai *et al.*, *An optical spectrum of the afterglow of a γ-ray burst at a redshift of $z = 6.295$*, Nature **440**, 184 (2006).

[10] J. E. Gunn and B. A. Peterson, *On the Density of Neutral Hydrogen in Intergalactic Space*, Astrophys. J. **142** 1633 (1965).

[11] The SWIFT collaboration, `http://heasarc.gsfc.nasa.gov/docs/swift/about_swift/objectives/environment.html`

[12] T. Piran, *Gamma-Ray Bursts and the Fireball Model*, Phys. Rep. **314**, 575 (1999).

[13] E. Waxman and J. Bahcall, *High Energy Neutrinos from Cosmological Gamma-Ray Burst Fireballs*, Phys. Rev. Lett. **78**, 2292 (1997).

[14] E. Waxman and J. Bahcall, *High Energy neutrinos from astrophysical sources: An upper bound*, Phys. Rev. D **59**, 023002 (1998).

[15] C. S. Reynolds and M. A. Nowak, *Fluorescent iron lines as a probe of astrophysical black hole systems*, Phys. Reports **377**, 389 (2003).

[16] The Cambridge X-ray astronomy group, `http://www-xray.ast.cam.ac.uk/xray_introduction/AGN_Jets.html`

[17] R. Sankrit and W. Blair, ESA, NASA, `http://antwrp.gsfc.nasa.gov/apod/ap041008.html`

[18] F. Aharonian *et al.* (HESS), *Observations of the Crab Nebula with H.E.S.S*, Astron. Astrophys. **457**, 899 (2006).

[19] F. Aharonian *et al.* (HESS), *A detailed spectral and morphological study of the gamma-ray supernova remnant RX J1713.7-3946 with H.E.S.S*, Astron. Astrophys. **449**, 223 (2006).

[20] J. Albert *et al.* (MAGIC), *Variable Very-High-Energy Gamma-Ray Emission from the Microquasar LS I +61 303*, Science **312**, 1771 (2006).

[21] D. Spergel *et al.* (WMAP), *First Year Wilkinson Microwave Anisotropy Probe (WMAP) Observations: Determination of Cosmological Parameters*, Astrophys. J. Suppl. **148**, 175 (2003).

[22] T. W. B. Kibble, *Topology Of Cosmic Domains And Strings*, J. Phys. **A9** 1387 (1976).

[23] K. Mannheim, R. J. Protheroe and J. P. Rachen, *On the cosmic ray bound for models of extragalactic neutrino production*, Phys. Rev. D **63**, 023003 (2001). `astro-ph/9812398`

[24] W. Rhode *et al.* (FREJUS), *Limits on the flux of very high energy neutrinos with the Frejus detector*, Astropart. Phys. **4**, 217 (1996).

[25] M. Ambrosio *et al.* (MACRO), *Search for diffuse neutrino flux from astrophysical sources with MACRO*, Astropart. Phys. **19**, 1 (2003). `astro-ph/0203181`

[26] R. Wischnewski *et al.* (BAIKAL), *The BAIKAL Neutrino Telescope - Results and Plans*, Int.J.Mod.Phys. **A20**, 6932 (2005). `astro-ph/0507698`

[27] J. Ahrens *et al.* (AMANDA-B10), *Limits on diffuse fluxes of high energy extraterrestrial neutrinos with the AMANDA-B10 detector*, Phys. Rev. Lett. **90**, 251101 (2003). `astro-ph/0303218`

[28] J. Hodges *et al.* (AMANDA-II), *Search for Diffuse Flux of Extraterrestrial Muon Neutrinos using AMANDA-II Data from 2000 to 2003*, 29th International Cosmic Ray Conference Pune, 101 (2005).

[29] R. Gandhi *et al.*, *Neutrino interactions at ultrahigh energies*, Phys. Rev. D **58**, 093009 (1998).

[30] S. L. Glashow, *Resonant Scattering of Antineutrinos*, Phys. Rev. **118**, 316 (1960).

[31] N. Palanque-Delabrouille, *Site comparison with test3'*, `ANTARES-Soft/2003-001`, (2003).

[32] J. A. Aguilar *et al.* (ANTARES), *Transmission of light in deep sea water at the site of the ANTARES neutrino telescope*, Astropart. Phys. **23**, 131 (2005).

[33] J. A. Aguilar *et al.* (ANTARES), *The data acquisition system for the ANTARES neutrino telescope*, acc. by Nucl. Instr. and Meth. A,`astro-ph/0610029`.

[34] B. van Rens, *The software trigger in ANTARES*, `ANTARES-Soft/2004-001`, (2004).

[35] J. A. Aguilar *et al.* (ANTARES), *Study of Large Hemispherical Photomultiplier Tubes for the ANTARES Neutrino Telescope*, Nuc. Inst. Meth. A **555**, 132 (2005).

[36] J. Hößl, private communication.

[37] D. Heck and J. Knapp, *Extensive air shower simulations with the* `CORSIKA` *code*, Nachr.Forsch.zentr.Karlsruhe **30**, 27 (1998).

[38] E. Korolkova and L. Thompson, *Monte Carlo Simulation of Cosmic Ray Muons at Sea Level with* `CORSIKA`, `ANTARES-Soft/2003-002`, (2003).

[39] N. N. Kalmykov, S. S. Ostapchenko and A. I. Pavlov, *Study of Large Hemispherical Photomultiplier Tubes for the ANTARES Neutrino Telescope*, Nuc. Phys. B (Proc. Suppl.) **52B**, 17 (1997).

[40] P. Antonioli *et al.*, *A Three-dimensional code for muon propagation through the rock: Music*, Astropart. Phys. **7**, 357 (1997). `hep-ph/9705408`

[41] D. J. L. Bailey, *Genhen v5r1: Software Documentation*, ANTARES-Soft/2002-004, (2002).

[42] G. Ingelman, A. Edin and J. Rathsman, *LEPTO 6.5 – A Monte Carlo generator for deep inelastic lepton-nucleon scattering*, Comput. Phys. Commun. **101**, 108 (1997).

[43] G. Barr, *The separation of signals and background in a nucleon decay experiment*, PhD Thesis, Keble College, University of Oxford, 1987.

[44] J. Pumplin *et al.*, *New Generation of Parton Distributions with Uncertainties from Global QCD Analysis*, JHEP **7**, 12 (2002).

[45] C. Carlogeanu, *Muon interactions at high energies.*, ANTARES-Phys/1998-013, (1998).

[46] D. J. L. Bailey, *KM3 v2r1: User Guide*, ANTARES-Soft/2002-006, (2002).

[47] Application Software Group, *GEANT 3.21: Detector description and simulation tool*, CERN Program Library long writeup W5013 (1995), http://wwwasdoc.web.cern.ch/wwwasdoc/geant_html3/geantall.html

[48] A. J. Heijboer, *Track Reconstruction and Point Source Searches with ANTARES*, PhD Thesis, Amsterdam University (2004).

[49] Y. Becherini and T. Stolarczyk, *Offline reconstruction and analysis software*, ANTARES-Soft/2006-003, (2006).

[50] S. Scholz, Diploma Thesis in preparation.

[51] Y. Becherini, private communication.

[52] R. W. Klebesadel, I. B. Strong, and R. A. Olson, *Observations of Gamma-Ray Bursts of Cosmic Origin*, Astrophys. J. **182**, L85 (1973).

[53] A. Mitra, *General Relativistic Collapse of Neutron Stars to Strange Stars: A Mechanism for Gamma-Ray Bursts*, astro-ph/0010311.

[54] J. Hjorth, *A very energetic supernova associated with the γ-ray burst of 29 March 2003*, Nature **423**, 847 (2003).

[55] J. N. Reeves *et al.*, *Outflowing supernova ejecta measured in the x-ray afterglow of Gamma-Ray Burst GRB011211*, Nature **416**, 512 (2002).

[56] M. Vietri and L. Stella, *A Gamma-Ray Burst Model with Small Baryon Contamination*, Astrophys. J. **507**, L45 (1998).

[57] T. Piran, *Gamma-ray bursts – a puzzle being resolved*, Phys. Rep. **333**, 529 (2000).

[58] J. Heise *et al.*, *Discovery of the X-ray burster SAX J1752.3-3138*, Astron. Astrophys. **378**, L37 (2001).

[59] R. M. Kippen *et al.*, in Proc. Woods Hole Gamma-Ray Burst Workshop, (2002). `astro-ph/0203114`

[60] G. J. Fishman *et al.* (BATSE), *The first BATSE gamma-ray burst catalog*, Astrophys. J. (Suppl. Series) **92**, 229 (1994).

[61] G. J. Fishman *et al.* (BATSE), Astronomy Picture of the Day `http://antwrp.gsfc.nasa.gov/apod/ap000628.html`

[62] D. Band *et al.*, *BATSE observations of gamma-ray burst spectra. I. Spectral diversity*, Astrophys. J. **413**, 281 (1993).

[63] J. I. Katz, Astrophys. J. Lett. **432**, L107 (1994).

[64] D. Guetta *et al.*, *Neutrinos from individual gamma-ray bursts in the BATSE catalog*, Astropart. Phys. **20**, 429 (2004).

[65] E. Waxman, *Gamma-Ray Bursts: The Underlying Model*, `astro-ph/0303517.`

[66] C. L. Fryer, S. E. Woosley, and D. H. Hartmann, *Formation Rates of Black Hole Accretion Disk Gamma-Ray Bursts*, Astrophys. J. **526**, 152 (1999).

[67] K. S. Hirata *et al.* (Kamiokande), *Observation of a Neutrino Burst from Supernova SN1987A*, Phys. Rev. Lett. **58**, 1490 (1987).

[68] R. M. Bionata *et al.* (IMB), *Observation of a Neutrino Burst in Coincidence with Supernova 1987A in the Large Magellanic Cloud*, Phys. Rev. Lett. **58**, 1494 (1987).

[69] M. C. Bouwhuis, *Detection of Neutrinos from Gamma-Ray Bursts*, PhD Thesis, Amsterdam University (2005).

[70] B. Hartmann, *Reconstruction of Neutrino-Induced Hadronic and Electromagnetic Showers with the ANTARES Experiment*, PhD Thesis, Erlangen University (2006).

[71] The KM3NeT Consortium, `http://www.km3net.org/`

[72] S. Kuch, PhD Thesis in preparation.

[73] G. Ricker *et al.* (HETE), *GRB 010921: Localization and observations by the High Energy Transient Explorer satellite*, Astrophys. J. **571**, L127 (2002).

[74] C. Winkler *et al.* (INTEGRAL), *The INTEGRAL mission*, Astron. Astrophys. **411**, L1 (2003).

[75] N. Gehrels *et al.* (SWIFT), *The SWIFT Gamma-Ray Burst Mission*, Astrophys. J. **611**, 1005 (2004).

[76] M. Tavani *et al.* (AGILE), *The AGILE Mission: Gamma-Ray Astrophysics of Galactic Sources*, http://www.mi.iasf.cnr.it/Agile/Homepage (2004).

[77] N. Gehrels and P. Michelson (GLAST), *GLAST: the next-generation high energy gamma-ray astronomy mission*, Astropart. Phys. **11**, 277 (1999).

[78] C. Kopper, PhD Thesis in preparation.

[79] G. J. Feldman and R. D. Cousins, *Unified approach to the classical statistical analysis of small signals*, Phys. Rev. D **57**, 3873 (1998).

[80] D. Clowe *et al.*, *A direct empirical proof of the existence of dark matter*, Astrophys. J. **648**, L109 (2006).

[81] H. Motz, *Berechnung von Neutrinoflüssen und erwarteten Ereignisraten in ANTARES aus Neutralino-Annihilation in der Sonne*, Diploma Thesis, Erlangen University 2005.

Danksagung

Ich möchte mich ganz herzlich bei allen bedanken, die mich bei der Anfertigung der vorliegenden Arbeit unterstützt haben. Mein Dank gilt:

- Frau Prof. Dr. Gisela Anton für die Vergabe dieser Doktorarbeit sowie der Förderung meiner Arbeit innerhalb der ANTARES-Kollaboration,
- Prof. Dr. Gerard van der Steenhoven for his willingness to serve as second referee and thereby reviewing the thesis carefully,
- Herrn Prof. Dr. Klaus Rith für das sorgfältige Korrekturlesen der Arbeit,
- Herrn Dr. Jürgen Hößl für die Betreuung der Arbeit, für seine ständige Diskussions- und Hilfsbereitschaft,
- Herrn Prof. Dr. Wolfgang Kretschmer für sein stetiges Interesse und die konstruktiven Diskussionen im Laufe meiner Arbeit,
- Herrn Dr. Jürgen Brunner für seine Einführung in das umfangreiche und nicht immer selbsterklärende ANTARES Software Paket,
- sowie Dr. Alexander Kappes, Dr. Bettina Hartmann, Dipl.-Phys. Holger Motz, Dipl.-Phys. Sebastian Kuch, Dipl.-Phys. Felix Fehr, Dipl.-Phys. Claudio Kopper für die gute Zusammenarbeit,
- und allen anderen Mitgliedern der Erlanger ANTARES-Gruppe, die nicht namentlich genannt werden können,
- meiner Mutter und Großmutter, die mich zeitlebens gefördert und unterstützt haben,
- meiner Schwiegermutter, die bereitwillig die Arbeit Korrektur gelesen hat und damit für stilistisch tadelloses Englisch gesort hat,
- und nicht zuletzt meinem Mann, Dipl. Phys. Christopher Naumann, dem ich nicht nur für die gute Zusammenarbeit in der Uni, seine engagierte Betreuung unserer Tochter Sophia und für die seelische Unterstützung während der Anfertigung dieser Arbeit zu danken habe ...

Desweiteren gebührt mein Dank dem Cusanuswerk, das meine Promotion durch ein Stipendium finanziert hat, sowie der Christiane-Nüsslein-Volhard Stiftung, deren finanzielle Unterstützung das Promovieren mit Kind erleichtert hat.